Chapter 8
Motors and Generators

Jeffrey H. Lang and Sauparna Das

This chapter describes the development of motors and generators as PowerMEMS machines. It also discusses aspects of the larger electromechanical energy conversion systems into which they fit. When coupled to microturbomachinery, typical applications of these machines might include motor/compressors, motor/pumps, and turbine/generators, all perhaps part of much larger systems such as a microengine or a microrocket.

Our development of PowerMEMS motors and generators takes place in the context of the system shown in Fig. 8.1. This system connects an electrical source or load to a mechanical load or source through an electric or magnetic machine and its attendant power electronics. If the machine acts as a motor, then power flows from left to right. If the machine acts as a generator, then power flows from right to left. The role of the machine in this context is the conversion of electrical to mechanical energy, or vice versa. The role of the power electronics is to commutate the machine; it is assumed here that the machine is an AC machine, while the electrical load or source is a DC device. The operation of the system takes place under the supervision of a local controller, which executes the desired regulation functions.

In every-day language, the terms "electric motor" and "electric generator" almost always refer to magnetic-field machines, rather than electric-field machines. This is understandable because electric-field machines are very rare in every-day life, while
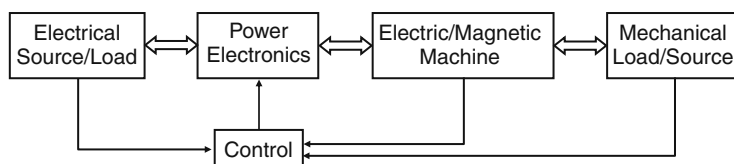

Fig. 8.1 An electric/magnetic machine system. Power flow is shown with *block arrows*. Signal flow is shown with *thin arrows*

J.H. Lang (✉)
Department of Electrical Engineering and Computer Science, Massachusetts Institute of Technology, Bldg 10-176, 77 Massachusetts Avenue, Cambridge, MA 02139, USA

magnetic-field machines are ubiquitous. The language of this chapter, however, must be more precise because both types of machines will be discussed. Thus, from this point forward the adjectives "electric" and "magnetic" will be used literally so as to avoid confusion. A non-specific machine will be refered to as "electromagnetic."

8.1 Background

Electromagnetic machine systems have been studied in great depth over the past two centuries, and their analysis, design and operation is thus very well understood [1–4]. Given this background, it is important to understand what is new and different in the context of PowerMEMS, beyond the obvious small size. It is also important to understand what is the same, and where electromagnetic PowerMEMS machines fit in the context of the prior art. That is the purpose of this section. Not surprisingly, there are important issues to reconsider, and these issues have a significant impact on the design and performance of electromagnetic PowerMEMS machine systems. At the same time, however, there is a very solid foundation on which to build their development. This too is discussed below.

8.1.1 What Is New?

Generally speaking, MEMS machines are fabricated through the selective addition (growth, deposition, electroplating, bonding) and subtraction (etching, lift-off, polishing) of materials to and from a wafer or wafer stack; see Chapter 2. This naturally leads to machines that are planar and disk shaped, which are uncommon, although not unseen, at the macroscale. Additionally, microfabrication is more limited in its capabilities than is macrofabrication, making it difficult to create microscale features that are common at the macroscale. For example, the aspect ratios of trenches and slots are more limited at the microscale. Also, useful features such as three-dimensionally smoothly rounded corners that would reduce breakdown in electric machines, or closed slots that would reduce losses in magnetic machines, are very difficult to fabricate at the microscale. Features on sidewalls are even more difficult to fabricate. Thus, MEMS machines must be designed within relatively constrained geometries.

Another important issue to reconsider is the relative torque and power density of electric and magnetic machines. At the macroscale, magnetic machines are considerably more power dense than electric machines, and this explains their ubiquitous presence. The stored energy density in the air gap of a magnetic machine is $B^2/2\mu_0$, where B is the magnitude of the magnetic field and μ_0 is the permeability of free space [5, 2]. This density is directly related to the magnetic shear stress acting on the rotor [2]. Generally, B is limited by magnetic saturation in the stator and/or rotor core. A typical air-gap B is 1.5 T, and so a typical magnetic air-gap energy density is 9×10^5 J/m^3. In contrast, the stored energy density in the air gap of an electric

machine is $\epsilon_0 E^2/2$, where E is the magnitude of the electric field and ϵ_0 is the permittivity of free space [5, 2]. Generally, E is limited by electric breakdown, which in a large smooth air gap will occur as E approaches 10^6 V/m [6–8]. This limits the electric air-gap energy density to 4 J/m^3, which is considerably lower than that found in a magnetic machine. However, when the air gap becomes very small, it no longer contains enough gas molecules to support avalanching electric breakdown, and the practical limit to E can rise to near 3×10^8 V/m [6–9]. In this case, the electric air-gap energy density becomes 4×10^5 J/m^3, which is comparable to that found in a magnetic machine. At this point, other factors might become important. For example, an electric machine could be CMOS compatible, whereas a magnetic machine would most certainly not. On the other hand, the narrow air gap of an electric machine gives rise to increased viscous losses. In any case, electric machines should be considered along with magnetic machines at the MEMS scale.

Following [8], Fig. 8.2 details the dependence of the breakdown voltage of a smooth gap containing various gases on the product of the gap separation and the gas pressure. Note the 1 Pa·m is approximately 10 μm at 1 atm. From the figure, it is apparent that very small air gaps, for example 3 μm at 1 atm, can sustain voltages in excess of 300 V. This corresponds to an electric field strength in excess of 10^8 V/m. Even higher field strengths, reaching the field emission limit for electrons near 10^9 V/m, are possible for smaller air gaps. In any case, the field strengths are considerably greater than those achieved at the macro scale.
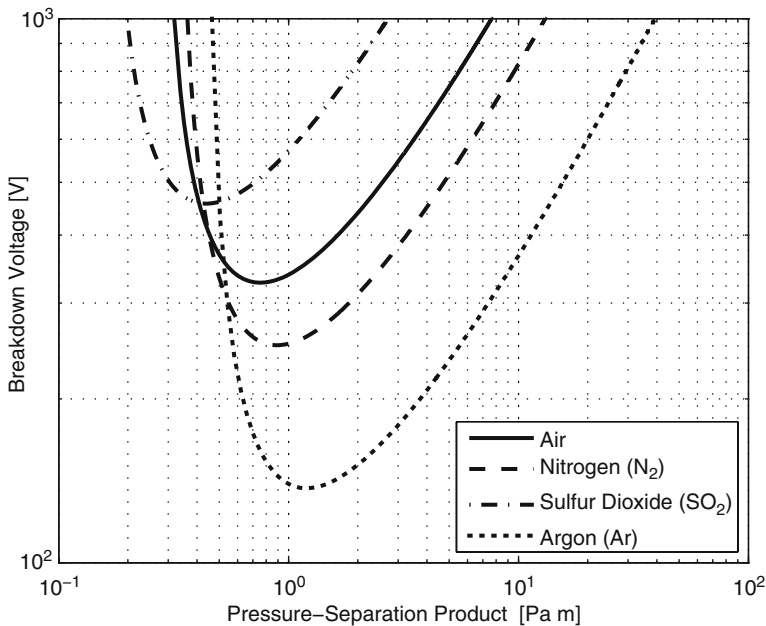

Fig. 8.2 Electric breakdown voltage for various gases in a smooth gap as a function of the gas-pressure-gap-separation product, following [8]. Note that 1 Pa·m is approximately 10 μm at 1 atm

Early micromotors, both electric and magnetic such as those described in [10–14] for example, applied electromagnetic stress to the circumferential edges of their rotors, as do most macroscale electromagnetic machines. Those micromotors converted energy through phases that exhibited a variable capacitance or a variable inductance. Such electromagnetic structures were very simple to implement by vertically etching salient stator and rotor poles simultaneously from a single planar material layer. However, when the rotor radius is larger than three times the rotor thickness, a greater torque can be achieved by applying the same stress to one planar surface of the rotor; here, the other planar surface is reserved for microturbomachinery. This, of course, requires more complex fabrication, but given the naturally planar geometry of MEMS machines it is the basic design pursued here in the interest of increased power throughput. Such designs have the added advantage that they free the gap at the edge of the rotor to become a journal bearing, as described in Chapter 6. However, they introduce the disadvantage of an unbalanced electromagnetic axial force on the rotor that must be balanced by an axial thrust bearing, again as described in Chapter 6. This added complexity is not common in macroscale machines, and should be managed through integrated electromechanical and bearing design.

As a further consequence of the way in which they are fabricated, it is rare to employ the assembly of many loose parts in an MEMS machine. Thus, the parts of MEMS machines are generally in intimate structural and thermal contact with one another over the broadest possible area, and this has two significant consequences. First, the rotors of MEMS machines have excellent structural integrity, enabling them to run at very high speeds. This offers the opportunity to design PowerMEMS machines with high power densities. Second, heat transfer through MEMS machines is relatively good, and this is enhanced by their planar geometries and the increasing ratio of surface area to volume of these machines as their size decreases. Thus, the traditional thermal limits observed in macroscale electric and magnetic machines are not observed in their PowerMEMS counterparts. This too opens up new design possibilities.

A simple rotating disk made from a homogenous material will burst when the speed of its peripheral tip reaches the burst speed u_B given by $\sqrt{8\sigma_F/(3+\nu)\rho}$, where σ_F is the fracture stress, ρ is the mass density, and ν is the Poisson's ratio of the material from which the disk is made [15]; see Chapter 2. This burst speed and the relevant material properties are given in Table 8.1 for silicon, 80/20 electroplated NiFe, a generic MnZn ferrite and a generic silicon steel; Young's modulus E is also given in the table for completeness. Two immediate conclusions can be drawn from the table. First, an electric machine having a silicon rotor can spin about two to three times faster than a magnetic machine having a solid steel rotor; note that solid steel rotors on the macroscale are rare. Thus, it is possible for the two machines to have comparable power densities even if the motive magnetic shear stress exceeds the motive electric shear stress. Again, electric machines should be considered along with magnetic machines in PowerMEMS applications. This becomes a stronger statement given the reduced burst speed of NiFe and MnZn ferrite, which are more probable materials for a PowerMEMS machine. Second,

Table 8.1 material properties and disk burst speed for silicon, 80/20 electroplated NiFe, a generic MnZn ferrite used for power applications, and a generic silicon steel used for power applications. Note that for silicon, Young's modulus varies from 130 to 196 GPa, and Poisson's ratio varies from 0.06 to 0.28, depending on crystallographic orientation. The properties of the other materials vary as well

Material	ρ [kg/m^3]	E [GPa]	ν	σ_F [GPa]	u_B [m/s]
Silicon	2330	160	0.18	4.1	2100
NiFe (80/20)	8500	140	0.3	1.6	675
MnZn Ferrite	4800	120	0.3	0.04	140
Silicon Steel	7700	230	0.25	2.0	800

macroscale magnetic machines exhibit maximum peripheral tip speeds more on the order of 100–150 m/s, and so PowerMEMS magnetic machines fabricated with more integral rotors can perhaps have greater power densities than their macroscale counterparts.

Because microscale PowerMEMS machines can operate at very high speeds they often do in order to obtain the highest possible power throughput. This in turn gives rise to very high electrical frequencies. As illustrated in subsequent sections, electrical frequencies ranging from many tens of kilohertz to several megahertz are not uncommon. Together, a high speed and high electrical frequency can lead to high material, bearing, aerodynamic and power electronics losses, and thus more complex design tradeoffs.

The importance of aerodynamic losses can be examined through Fig. 8.3, which shows a disk rotor of radius R spinning with tip speed u above a stator with an air-gap separation of G. Assuming laminar azimuthal air flow between the rotor and the stator, the viscous loss in the air gap is given by $\pi \mu_V R^2 u^2/2G$, where μ_V is the absolute viscosity of air, taken here to be 1.8×10^{-5} Ns/m^2. If at the same time, the rotor experiences a uniform electromagnetic shear stress of σ_{EM}, then the electromagnetic motive power is given by $2\pi \sigma_{EM} R^2 u/3$. The ratio of the viscous loss to the motive power is therefore $3\mu_V u/4G\sigma_{EM}$. As an example, consider an electric machine with a 3-μm air gap across which the rotor–stator potential difference varies sinusoidally in the azimuthal direction with a 300-V amplitude. In this machine the peak electric field is 10^8 V/m, and so the peak electric air-gap energy density is 4.4×10^4 J/m^3. Its spatial average is then 2.2×10^4 J/m^3. Typically, an electric machine might achieve an average electric shear stress equal to 10% of its average stored air-gap energy density, which averages to 2.2×10^3 N/m^2 in this example. Assuming that the rotor
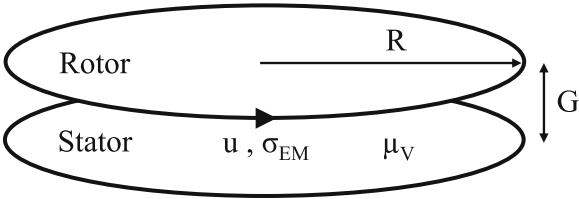

Fig. 8.3 Geometry for comparing viscous losses and electromagnetic motive power

tip speed u is 500 m/s, as allowed by Table 8.1 for silicon, the ratio of viscous loss to motive power is 1. Thus, it is important to account for viscous loss during the design of an electric PowerMEMS machine, particularly for motors as explained later in this subsection. Magnetic machines, which can successfully operate with much larger air gaps, need not exhibit such high viscous losses, but those losses can still be significant at the microscale.

In electric PowerMEMS machines, high-frequency operation has its most serious impact through losses in the power electronics; the typical power electronics for an electromagnetic machine is shown in Fig. 8.4 [3, 4]. The figure shows the switching branch for one phase, and includes two capacitors to model parasitic wiring and transistor capacitance. The power electronics operate by alternately turning the top and bottom transistors on and off, thereby applying a voltage square-wave to the corresponding phase of the machine; a varying duty cycle can be used to implement more complex time-average waveforms. If the switching frequency is f, then the power dissipated in this circuit due to the charging and discharging of the two parasitic capacitors is $2C_P V^2 f$ per phase. To illustrate the importance of this loss, let C_P be 10 pF, V be 300 V, and f be 1 MHz, as could be the case for an electric PowerMEMS machine. In this case, the power loss is 1.8 W per phase. Thus, the design of the power electronics and proper management of parasitics is critical to the performance of a PowerMEMS machine, particularly an electric PowerMEMS machine.

Fig. 8.4 Power electronics for an electric machine; only one phase branch is shown
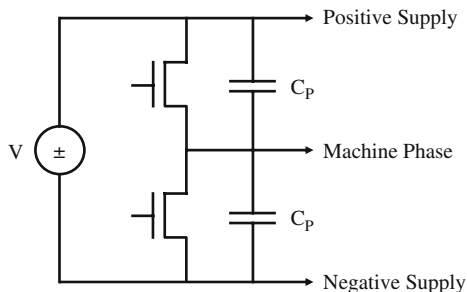
In magnetic PowerMEMS machines, high-frequency operation introduces significant challenges through eddy currents and losses in the core. The role of the core in a magnetic machine is to guide magnetic flux through the machine without incurring a significant loss of magnetomotive force [1]. At high frequencies, eddy currents in the core act to exclude the flux, rendering the core ineffective. These eddy currents also generate loss. A core carries substantial magnetic flux only within a magnetic skin depth δ of its surface [5, 2]; the magnetic skin depth is given by $\sqrt{2/\omega\mu\sigma}$, where ω is the radian frequency of the flux, μ is the permeability of the core, and σ is the conductivity of the core. Therefore, planar cores, into which magnetic flux diffuses from both sides, carry flux only over a thickness of a few skin depths. Thicker cores exhibit wasted material from a magnetic viewpoint. To circumvent this problem, cores are thinly laminated, with the lamination thickness set to a skin depth

or two, or less. This also helps reduce eddy-current losses by crowding the eddy currents into narrow regions. The skin depth at 100 kHz and the relevant material properties are given in Table 8.2 for electroplated NiFe, a generic MnZn ferrite and a generic silicon steel. Two immediate conclusions can be drawn from the table. First, if materials such as electroplated NiFe are to be used for high-performance magnetic PowerMEMS machines, their fabrication will be complicated by the need for very thinly laminated cores, on the order of 50 μm or less. Second, where possible, ferrite substrates might profitably be used in cores due to their greatly reduced conductivity. Unfortunately, their saturation flux density, B_S, is generally low, which will possibly require a thick substrate.

Table 8.2 magnetic properties and skin depth at 100 kHz for 80/20 electroplated NiFe, a generic MnZn ferrite used for power applications, and a generic silicon steel used for power applications; note that the permeability is relative to that of free space, $\mu_0 = 4\pi \times 10^{-7}$ H/m

Material	σ [S/m]	μ/μ_0	B_S [T]	δ [m]
NiFe (80/20)	6.7×10^6	500	0.8	2.5×10^{-5}
MnZn ferrite	0.2	3000	0.5	4.2×10^{-3}
Silicon steel	2×10^6	5000	2.2	1.6×10^{-5}

Thermal considerations are also very different at the microscale. In well-designed and well-constructed macroscale magnetic machines, it is typical to observe current densities ranging from about 10^6 A/m^2 for natural-air-cooled machines to about 10^7 A/m^2 for liquid-cooled machines. The current density is limited by the tolerable temperature rise, and so such current density limits are often used as substitutes for a thermal analysis. In the MEMS magnetic machines described here, current densities of 10^9 A/m^2 are common, as permitted by their excellent heat transfer. The immediate consequences of this can be seen through Fig. 8.5. The figure shows the rotor and stator of a simple magnetic machine having an air-gap separation of G. The stator supports windings carrying a current density J that are laid with alternating direction in slots each having an area A. The magnetic flux density created by the stator currents is B. Following Ampere's Law [1, 5], the peak magnetic flux density B in the air gap is approximately $\mu_0 JA/2G$, assuming that B is one-dimensional and the stator and rotor cores are highly permeable. From this, it is apparent that the achievable B will decrease linearly with dimensional scale as the size of the machine
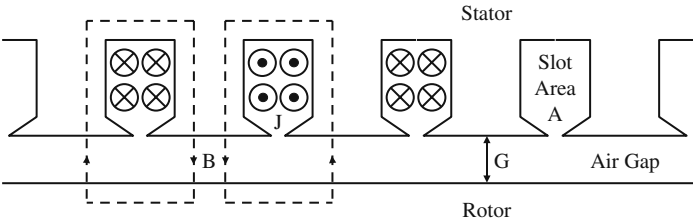

Fig. 8.5 The magnetic flux in a slotted magnetic machine

decreases for a given *J*. Thus, without some form of thermal relief, the performance of a MEMS magnetic machine will be relatively poor. Fortunately, the excellent heat transfer observed in MEMS machines provides the necessary thermal relief, and this must be taken into account during design.

Finally, the role of parasitics in general in PowerMEMS machine systems is more prominent than in macroscale machine systems. For example, parasitic capacitance in the stator wiring and power electronics of electric machines systems can be particularly significant, as can the parasitic winding inductance and core loss in magnetic machine systems. Aerodynamic and bearing losses can be significant in both machine systems. Moreover, the significance of these phenomena depends on the application as can be seen in Fig. 8.6. The figure shows the flow of power, including losses, through an electromagnetic machine system during both motoring (top) and generating (bottom) operation. In both sub-figures it is important to realize that the air-gap power is a bottleneck. This power is determined by the electromagnetic shear stress acting on the rotor, which is in turn limited by the available electromagnetic energy stored in the air gap. Therefore, losses downstream of the air gap not only lower efficiency, but more importantly limit the available output power. For a given machine, they cannot be compensated by an increased input power once the air-gap power limit is reached.
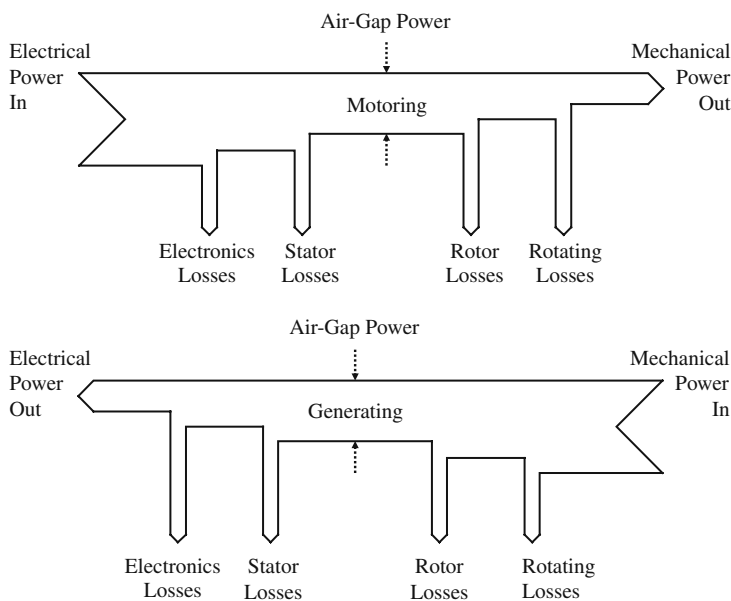

Fig. 8.6 Power flow in an electromagnetic machine system during both motoring (*top*) and generating (*bottom*) applications

By way of example, consider an electric PowerMEMS machine. These machines typically have relatively large parasitic capacitances between their stator electrodes and the surrounding silicon support structure or substrate. In an AC machine, these

capacitances will cause reactive currents to flow through the stator wiring and power electronics, and the currents will in turn create significant losses. It is for this reason that thick dielectrics are used to separate the stator wiring and electrodes from the substrate, and thereby reduce the parasitic capacitances. In motoring operation, the losses are upstream of the air gap, as seen in Fig. 8.6, and so they act only to reduce efficiency. However, during generating operation, these losses are downstream of the air gap, and so serve not only to reduce efficiency, but also to limit output power. In fact, without the use of thick dielectrics to reduce parasitic capacitances, the associated losses can consume the majority, if not all, of the power that passes through the air gap. A similar example could be made of core loss in a magnetic machine given the typical high electrical frequencies involved. Alternatively, aerodynamic and bearing losses in both machines can have a limiting effect during motoring operation. Thus, parasitics in PowerMEMS machines must be managed early during design.

8.1.2 What Is Old?

While there are many issues that warrant reconsideration in the context of electromagnetic PowerMEMS machines, there are also important aspects of electromagnetic machine analysis, design and operation that are common across the macro- and microscales. For example, Maxwell's Equations are applicable at both scales. Further, since both macroscale and microscale machines make use of the bulk properties of their constituent materials, the relevant material laws are the same at both scales, even though the specific numerical values of their properties may differ due to material selection. Thus, the types and operating principles of electromagnetic machines are common to both scales, as are the approaches to analysis (analytical and numerical), design, and control.

8.1.3 Electromagnetic Machine Types Attributes, and Selection

Maxwell's Equations exhibit symmetry in the equations which govern the behavior of electric and magnetic fields. There is also a strong formulaic similarity between the equations which govern the behavior of electric and magnetic materials. Because of this, there is a duality in the basic types of electric and magnetic machines [16]. For example, Table 8.3 catalogs the dual pairs of some basic AC electric and magnetic machines [1]. Other dual machine pairs can be created by combining the features of those listed in the table. In principle, any such machine could be implemented as a PowerMEMS machine. In that case, which one is the best choice for a given PowerMEMS motoring or generating application? While there is no universal answer to this question, there are good guidelines for a selection. These guidelines are described next in the context of the Microengine Project.

Table 8.3 Some basic AC electric and magnetic machine duals. The first three machines in each column are synchronous machines, while the induction machines are asynchronous

Electric machine	Magnetic machine
Variable capacitance	Variable reluctance
Permanent-electret	Permanent-magnet
Excited-rotor	Wound-field
Induction	Induction

To begin, those machines with externally excited rotors, specifically the electric excited-rotor and the magnetic wound-field synchronous machines [1], require brushes and slip rings to bring the excitation to their rotating rotor phases. At the macroscale, this poses few challenges, and is common practice. However, at the microscale there is no proven brush and slip ring technology. Further, even if such components were developed, they would likely cause a significant mechanical loss. Thus, these machines are eliminated here as impractical at the microscale. Similar concerns eliminate the use of brushes and commutator bars as a means of commutating AC machines, which would result in a traditional DC machine as viewed from the outermost electrical terminals.

Consider next the electric variable-capacitance and magnetic variable-reluctance synchronous machines [1, 17], which have both been implemented as MEMS machines [10–14]. These machines usually use slots on both the stator and rotor to define salient poles that are excited by electrodes or windings on the stator. The poles then attract to produce a torque. In general, to be good torque producers, these machines require deep slots and very narrow air gaps in order to create a large difference between the maximum and minimum phase capacitance or inductance. Further, they require relatively accurate rotor position information to support the commutation required for good performance, both as a motor and as a generator [18, 19], which is challenging to measure at the microscale. While these machines exhibit excellent rotor integrity, they are nonetheless eliminated here due to their fabrication challenges, their control challenges, and the viscous loss they incur with a small air gap.

After elimination of the others, only the permanent-electret and permanent-magnet synchronous machines, and the two asynchronous induction machines, remain. Each is a viable candidate for the Microengine Project, and the selection among them is more complex. Consider first a comparison of the two electric machines, and a separate comparison of the two magnetic machines.

In an MEMS electric induction machine exhibiting a typical air-gap electric field magnitude E of 10^8 V/m, the induced surface charge on the rotor is approximately $\epsilon_0 E$, or 0.9×10^{-3} C/m^2. This is very close to the $0.5 - 1.2 \times 10^{-3}$ C/m^2 surface charge reported for MEMS permanent electrets fabricated from thin films of Teflon, similar materials and silicon dioxide [20–23]. Thus, the two machines appear electromechanically comparable at the microscale because it is the rotor surface charge which interacts with the stator excitation to produce a torque. However, the

permanent electrets are not yet stable against leakage and decay over time, particularly at temperatures approaching 80°C and above. Further, being a synchronous machine, the permanent-electret machine requires position information to operate at its best, which is again difficult to provide at the microscale. Therefore, the electric induction machine is chosen here over the permanent-electret synchronous machine. The development of the electric induction machine is presented in Section 8.3.

The choice between the permanent-magnet synchronous machine and the magnetic induction machine is much less clear than in the case of the dual electric machines. Samarium-cobalt magnets are capable of high-performance operation even beyond 300°C. For this reason, both machines have been studied in detail as PowerMEMS machines. The primary conclusion from this work is that, when permitted by thermal considerations, the permanent-magnet synchronous machine appears to be the better choice, and so it is chosen here. The permanent-magnet synchronous machine is generally more power dense and efficient than the induction machine at the microscale due largely to the challenge of inducing substantial rotor currents at that scale. Permanent magnets, on the other hand, maintain their bulk performance at the micro scale, easily offering a good rotor field excitation. The development of the permanent-magnet synchronous machine is presented in Section 8.4. The development of the magnetic induction machine as a PowerMEMS machine is chronicalled in [24–28].

At this point, a comparison between the electric and magnetic machines chosen above is deferred until Section 8.5. As mentioned in Section 8.1.1, electric and magnetic PowerMEMS machines have very different properties, leading to very different advantages and disadvantage.

8.1.4 Summary

There are several important messages to take away from the discussion presented in this section. Perhaps the most important message is that while the practice of analysis and design of electromagnetic PowerMEMS machines may be no different than for any other electromagnetic machine, the end product likely will be quite different. This results from a combination of: (1) different geometries and fabrication constraints; (2) new materials; (3) revised thermal, speed and frequency considerations; (4) the need to consider both electric and magnetic machines; and (5) the increased importance of parasitics. More details may be found in Sections 8.1.1 and 8.1.2. Another important message is the interplay between microfabrication limitations and the performance of a PowerMEMS machine. The resulting design tradeoffs are significant, particularly given the need to manage such phenomena as parasitic capacitance and viscous loss in electric machines, and eddy currents in magnetic machines. Finally, from the viewpoint of PowerMEMS applications such as the Microengine Project, two electromagnetic machine systems stand out as being best suited to such applications. Those systems are based on the electric

induction machine and the permanent-magnet synchronous machine. Both machine systems are discussed in detail below. The rationale for this conclusion is given in Section 8.1.3.

8.2 Modeling Simplifications

As indicated in Fig. 8.3, the electromagnetic machines studied here are disk-shaped. Thus, the fields between, within, and outside their stators and rotors are naturally analyzed in cylindrical coordinates. Such an analysis, however, leads to three-dimensional fields involving a mix of Fourier and Bessel functions [29]. While these fields are simple enough to derive, they are too complex to permit the most transparent discussion of machine performance. Therefore, approximate two-dimensional fields are derived here based on an approximate rectilinear machine geometry. The two-dimensional fields are simple enough to permit a transparent discussion of machine performance without a significant loss of accuracy, at least for the geometries typically seen in Power-MEMS electromagnetic machines.

The approximate two-dimensional fields are developed with reference to Fig. 8.7. Here, the annular rotor and stator of an electromagnetic machine are sliced along a radius, and unwrapped and stretched onto Cartesian coordinates. The resulting rectilinear machine is then analyzed using Cartesian coordinates, and its fields are wrapped back onto the original cylindrical geometry in the end. To further simplify matters, the fields are assumed to be uniform in x when analyzed using the Cartesian coordinates. That is, the fields are assumed to be two dimensional. This is justified for a typical Power-MEMS machine in part because the axial extent of the fields is much narrower than the distance from the inner radius of the machine to the outer radius, and so field fringing at the two extreme radii should be minor.
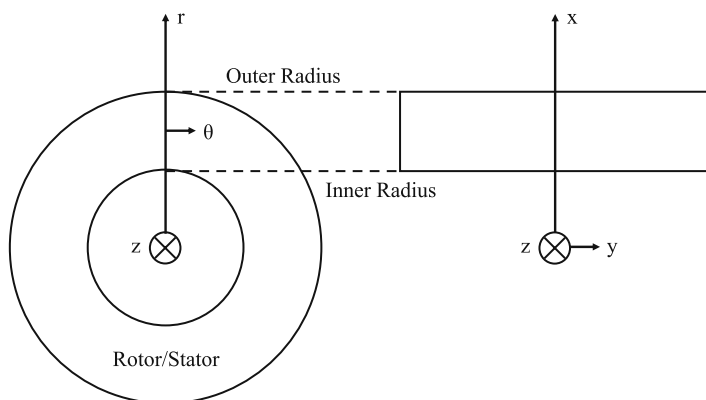

Fig. 8.7 The relation between the natural cylindrical coordinates (*left*) and approximate Cartesian coordinates (*right*) used to analyze the electromagnetic machines

The primary equation of interest here will be Laplace's Equation which is to be solved in the two-dimensional y-z plane. Since the electromagnetic machine is structurally periodic in θ, its fields are also periodic in θ, and hence in y. Thus, the corresponding solutions to Laplace's Equation will take the form $e^{\pm jky}e^{\pm kz}$ in Cartesian coordinates, where k is the wavenumber of the periodicity [5, 29]. This solution is mapped back to the cylindrical coordinates using the mapping

$$x \to r \quad , \quad y \to r\theta \quad , \quad z \to z \quad , \quad k \to \frac{mP}{r} \quad , \tag{8.1}$$

in which the wavenumber mapping guarantees that the solutions are periodic in θ for all r with fundamental periodicity P. The integer P is determined by the machine geometry, and will ultimately become the number of pole pairs in the machine. The integer m will be used to index higher space harmonics. Thus, the approximate solutions to Laplace's Equation in cylindrical coordinates take the form $e^{\pm jmP\theta}e^{\pm mPz/r}$. Such solutions essentially treat each cylindrical sliver of the machine as independent and two-dimensional.

To investigate the conditions under which the approximate solutions to Laplace's Equation are valid, those solutions can be substituted back into Laplace's Equation to yield

$$0 \approx \left(\frac{1}{r}\frac{\partial}{\partial r}\left(r\frac{\partial}{\partial r}\right) + \frac{1}{r^2}\frac{\partial^2}{\partial\theta^2} + \frac{\partial^2}{\partial z^2}\right)e^{\pm jmP\theta \pm mPz/r} \tag{8.2}$$

$$= \left(\pm\frac{mPz}{r^3} + \frac{m^2P^2z^2}{r^4} - \frac{m^2P^2}{r^2} + \frac{m^2P^2}{r^2}\right)e^{\pm jmP\theta \pm mPz/r} \tag{8.3}$$

in cylindrical coordinates. Note that the first two terms in (8.3) come from the partial derivatives with respect to r in (8.2), the third term comes from the partial derivatives with respect to θ, and the fourth term comes from the partial derivatives with respect to z. In order for (8.3) to evaluate approximately to zero, the dominant balance in the equation must be between the last two terms, with the first two terms being small. Since the product mP is a positive integer, the first two terms will be small in regions in which $|z| \ll r$. Most electromagnetic PowerMEMS machines exhibit fields that are essentially confined to narrow planar regions that are much shorter in the axial direction than the inner annular radius of their rotor and stator, and so this condition is easily met. When it is not, one must solve Laplace's Equation directly in cylindrical coordinates.

8.3 Electric Induction Machine

A cross-section side view of the electric induction machine studied here is shown in Fig. 8.8. Photographs of the machine fabricated as a PowerMEMS machine are shown in Fig. 8.9. The stator comprises radially directed electrodes, like spokes, supported by an insulator on a conducting substrate. The stator electrodes are wired
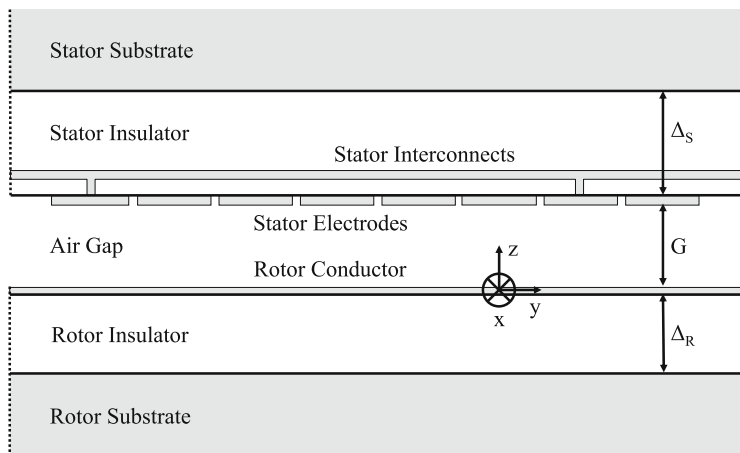
Fig. 8.8 Side view of the electric induction machine with the Cartesian coordinates used for analysis
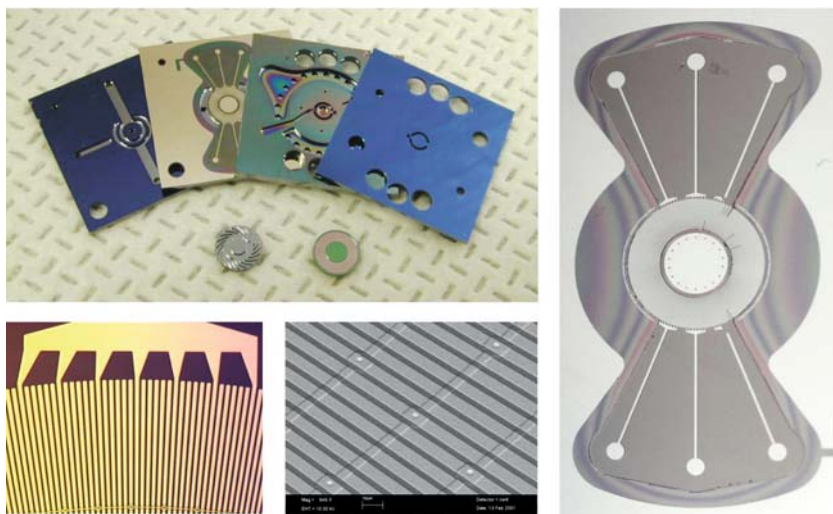

Fig. 8.9 Photographs of an MEMS electric induction machine from [35]. The *top-left* photograph shows a five-wafer set which, when fully bonded, forms a complete motor/compressor or turbine/generator depending on the design of the blades. The middle-right wafer is already a bonded wafer pair that contains the rotor. The middle-left wafer is the stator wafer. The two outer wafers are foundation wafers that contain many of the air passages connecting to the compressor or turbine, and the air bearings. Below the wafers are two separated rotors. The rotor on the left shows its turbine blades, while the rotor on the right shows its annular rotor conductor surrounding a thrust bearing pad. The *right*-most photograph shows a close-up view of the stator fabricated on top of buried silicon dioxide in the shape of a bow tie. The six phase leads that terminate on contact pads are also visible. The stator electrodes in the central annular region are not distinguishable, but the air nozzles around the periphery of the center thrust bearing are visible. The *lower-left* photograph shows a close-up view of the stator electrodes near their connection to one of the phase leads. One interconnect ring is visible at the very bottom of the photograph. The *lower-middle* photograph shows another close-up view of the stator electrodes which shows three interconnect rings (reprinted from Livermore et al. [35] © 2004 IEEE)

together through back-side interconnects to form N phases; every Nth electrode is connected to form a single phase. In both figures, N is 6. The interconnected electrode pattern is repeated P times around the stator. Thus, the total number of stator electrodes is NP. In Fig. 8.9, P is 131 for a total of 768 electrodes. The rotor consists of a thin uniform conductor also supported by an insulator on a conducting substrate. In the applications considered here, the bottom side of the rotor could be etched to form turbine or compressor blades. The blades are not shown in Fig. 8.8, but they are visible in Fig. 8.9. In the machines studied here, the substrates are silicon, the insulators are silicon dioxide, the stator electrodes and interconnects are either metal or heavily doped polysilicon, and the rotor conductor is moderately doped polysilicon.

The stator phases of an electric induction machine are generally excited with balanced sinusoidal voltages, having a temporal phase shift of $2\pi/N$ from one phase to the next, and hence one electrode to the next. In this way, the phases support a traveling wave of potential that circulates around the stator. The stator potential and the corresponding charges on the stator electrodes induce image charges on the rotor conductor, as shown in Fig. 8.10. In steady state, the image charges on the rotor must travel in synchronism with the stator excitation. Part of this travel is provided by convection arising from the motion of the rotor, and part is provided by conduction through the rotor. During motoring operation, as shown in Fig. 8.10, the stator potential travels at a speed that exceeds that of the rotor motion, and so the rotor charges lag behind. To stay in synchronism with the stator potential, the rotor charges conduct forward through the rotor conductor, and this conduction is driven by the horizontal component of the air-gap electric field. This same electric field component produces the motoring torque acting on the rotor. During generating operation, the speed of the rotor motion exceeds that of the stator potential wave, and the rotor charges lead their images on the stator electrodes. In this case, the charges conduct backward through the rotor to maintain synchronism, and the horizontal component of the electric field is reversed.

The development of the electric induction machine as a PowerMEMS motor is chronicalled in [30–36], with [30, 31] providing the greatest detail, and [35]
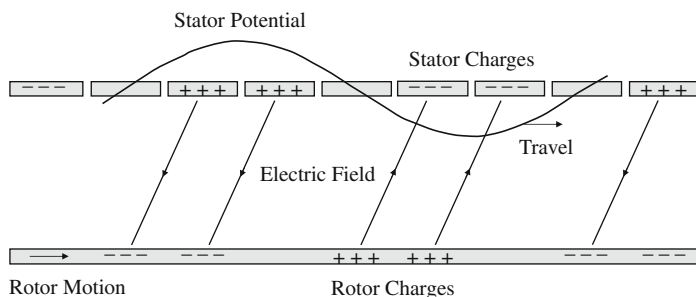

Fig. 8.10 A diagram of the traveling stator potential, the charges on the stator electrodes and the rotor conductor, and the electric field in the air gap, within an electric induction machine during motoring operation

providing additional experimental results. The development of the electric induction machine as a PowerMEMS generator is chronicalled in [37–39], with [37] providing the greatest detail. Additionally, the electric induction machine has a substantial development history as a macro-scale motor. Much of this early work is described in [29, 40–45]. Finally, the electric induction machine has been studied as a direct fluid pump both at the microscale [46, 47], and much earlier at the macroscale [29, 48]. The subsections that follow are based largely on this collective work.

8.3.1 Analysis

The analysis presented here is a steady-state analysis which closely follows that presented in [31–33, 36]. It is one in which the rotor moves with a constant angular velocity, and the stator electrodes are excited with balanced sinusoidal voltages. Its objective is to determine the steady-state forces and torques at work within the electic induction machine, and the steady-state power flow through it. Such an analysis is adequate to understand the fundamental behavior of the electric induction machine, and its power electronics, and to investigate design and performance tradeoffs. However, there are situations in which an unbalanced and/or transient model is required. One important situation is during the analysis of self-exciting resonant operation in which imbalances play a critical role at the microscale. In such cases, the reader is refered to [37, 38, 39] for an extended model.

The analysis of the electric induction machine begins with its stator excitation. This excitation is spatially piecewise constant, except for the small gaps between the stator electrodes which are ignored here. It is also periodic, and thus expressible in a Fourier Series over the angle θ defined in Fig. 8.7. Thus, if the N stator voltages v_n, $0 \le n < N$, are given by

$$v_n(t) = V \cos{(\omega t - 2\pi n/N)} \quad , \tag{8.4}$$

where V and ω are the electrical stator excitation amplitude and frequency, respectively, then the stator potential ϕ_S at $z = G$ may be written as

$$\phi_S(r,\theta,z = G,t) = \sum_{m=-\infty}^{\infty} V_m \cos{(\omega t - mP\theta)} \tag{8.5}$$

$$V_m \equiv \begin{cases} V\frac{N}{m\pi} \sin{\left(\frac{m\pi}{N}\right)} & m = \cdots 1 - N, 1, 1 + N, 1 + 2N \cdots \\ 0 & \text{otherwise} \end{cases} ; \tag{8.6}$$

For the case of $N = 6$, as shown in Figs. 8.8, 8.9, and 8.10, for example, $V_1 = 0.95\,V$, while $V_{-5} = 0.19\,V$ and $V_7 = -0.14\,V$. Thus, while the higher space harmonic amplitudes do fall off essentially as $1/m$, this decay may not be

rapid enough to justify ignoring the higher harmonics altogether. The stator potential expressed in (8.5) becomes

$$\phi_S(y, z = G, t) = \sum_{m=-\infty}^{\infty} V_m \cos(\omega t - k_m y) \tag{8.7}$$

$$k_m \equiv \frac{mP}{r} \tag{8.8}$$

in the approximate Cartesian coordinates defined in Figs. 8.7 and 8.8, after the mapping in (8.1) is applied. It is a superposition of potential waves traveling in the y direction.

The next step in the analysis is to determine the electric potential within the stator, the air gap and the rotor, all driven by the stator potential at $z = G$. This requires the solution to Laplace's Equation within these three regions, which is developed here in the Cartesian coordinates shown in Fig. 8.8. To solve Laplace's Equation, boundary conditions of zero potential are applied at the axial extremes, namely at $z = G + \Delta_S$ and $z = -\Delta_R$. Further, the thin rotor conductor at $z = 0$, which separates the air gap from the rotor insulator, is assumed to behave as a surface conductor with surface conductivity σ_R, and the stator and rotor insulators are assumed to have permittivity ϵ. Finally, the rotor is assumed to rotate with angular velocity Ω. Under these conditions, the three potentials are given by

$$\phi_S(y, z, t) = \sum_{m=-\infty}^{\infty} \Re\left\{ V_m \frac{\sinh(k_m(\Delta_S + G - z))}{\sinh(k_m \Delta_S)} e^{j(\omega t - k_m y)} \right\} \tag{8.9}$$

$$\phi_G(y, z, t) = \sum_{m=-\infty}^{\infty} \Re\left\{ \left(V_m \frac{\sinh(k_m z)}{\sinh(k_m G)} + \hat{\Phi}_{R_m} \frac{\sinh(k_m(G - z))}{\sinh(k_m G)} \right) e^{j(\omega t - k_m y)} \right\} \tag{8.10}$$

$$\phi_R(y, z, t) = \sum_{m=-\infty}^{\infty} \Re\left\{ \hat{\Phi}_{R_m} \frac{\sinh(k_m(\Delta_R + z))}{\sinh(k_m \Delta_R)} e^{j(\omega t - k_m y)} \right\} \tag{8.11}$$

where ϕ_S, ϕ_G, and ϕ_R are the potentials in the stator ($G \leq z \leq G + \Delta_S$), the air gap ($0 \leq z \leq G$), and the rotor ($-\Delta_R \leq z \leq 0$), respectively, and

$$\hat{\Phi}_{R_m} \equiv V_m \beta_m \frac{j S_m \omega \tau_m}{1 + j S_m \omega \tau_m} \tag{8.12}$$

$$\beta_m \equiv \frac{\epsilon_\circ / \sinh(k_m G)}{\epsilon_\circ \coth(k_m G) + \epsilon \coth(k_m \Delta_R)} \tag{8.13}$$

$$\tau_m \equiv \frac{\epsilon_\circ \coth(k_m G) + \epsilon \coth(k_m \Delta_R)}{\sigma_R k_m} = \frac{\epsilon_\circ}{\sigma_R \beta_m k_m \sinh(k_m G)} \tag{8.14}$$

$$S_m \equiv \frac{\omega - mP\Omega}{\omega} \quad . \tag{8.15}$$

As expressed in (8.12), $\hat{\Phi}_{R_m}$ is the complex amplitude of the electric potential in the rotor conductor for space harmonic m. Further, as defined in (8.13), (8.14) and (8.15), β_m is the capacitive potential division from the stator to the rotor, τ_m is the rotor charge-relaxation time, and S_m is the slip such that the electrical frequency of the traveling stator potential wave as viewed from the moving rotor is $S_m\omega$, again all for space harmonic m.

The electric field in the three regions, the free surface charge densities on the stator electrodes and the rotor conductor, the shear and normal stresses of electric origin acting on the rotor, and the power dissipation density in the rotor conductor, can all be determined from the potentials given in (8.9), (8.10) and (8.11). The electric field $\bar{E}$ is given in each region by

$$\bar{E} = -\nabla\phi \quad . \tag{8.16}$$

The free surface charge densities on the stator and rotor, ρ_S and ρ_R, respectively, are given by

$$
\begin{aligned}
\rho_S(y,t) &= \epsilon E_{S_z}|_{z=G} - \epsilon_0 E_{G_z}|_{z=G} \\
&= \sum_{m=-\infty}^{\infty} \Re\left\{ V_m k_m \left(\epsilon \coth\left(k_m \Delta_S\right) + \epsilon_0 \coth\right. \right. \\
&\quad \left.\left. - \frac{\epsilon_0 \beta_m}{\sinh\left(k_m G\right)} \left(\frac{jS_m\omega\tau_m}{1 + jS_m\omega\tau_m}\right)\right) e^{j(\omega t - k_m y)}\right\}
\end{aligned}
\tag{8.17}
$$

$$
\begin{aligned}
\rho_R(y,t) &= \epsilon_0 E_{G_z}|_{z=0} - \epsilon E_{R_z}|_{z=0} \\
&= \sum_{m=-\infty}^{\infty} \Re\left\{ \frac{-\epsilon_0 k_m V_m}{\sinh\left(k_m G\right)} (1 + jS_m\omega\tau_m) e^{j(\omega t - k_m y)}\right\} \quad .
\end{aligned}
\tag{8.18}
$$

The y-directed spatial average of the shear and normal stresses of electric origin acting on the rotor, $< f_y >$ and $< f_z >$, respectively, are given by

$$
\begin{aligned}
\langle f_y \rangle &= \langle \epsilon_0 \, E_{G_y}\big|_{z=0} \, E_{G_z}\big|_{z=0} \rangle = \langle \epsilon_0 \left.\frac{\partial\phi_G}{\partial y}\right|_{z=0} \left.\frac{\partial\phi_G}{\partial z}\right|_{z=0} \rangle \\
&= \sum_{m=-\infty}^{\infty} \frac{\epsilon_0 \beta_m k_m^2 V_m^2}{2\sinh\left(k_m G\right)} \left(\frac{S_m\omega\tau_m}{1 + S_m^2\omega^2\tau_m^2}\right)
\end{aligned}
\tag{8.19}
$$

$$
\begin{aligned}
\langle f_z \rangle &= \langle \frac{\epsilon_0}{2} \left(E_{G_z}^2\big|_{z=0} - E_{G_y}^2\big|_{z=0}\right)\rangle = \langle \frac{\epsilon_0}{2} \left(\left(\frac{\partial\phi_G}{\partial z}\right)^2\bigg|_{z=0} - \left(\frac{\partial\phi_G}{\partial y}\right)^2\bigg|_{z=0}\right)\rangle \\
&= \sum_{m=-\infty}^{\infty} \frac{\epsilon_0 k_m^2 V_m^2}{4\sinh^2\left(k_m G\right)} \left(\frac{1 + S_m^2\omega^2\tau_m^2 \left(1 - 2\cosh\left(k_m G\right)\beta_m + \beta_m^2\right)}{1 + S_m^2\omega^2\tau_m^2}\right)
\end{aligned}
\tag{8.20}
$$

where $\langle \cdot \rangle$ denotes the y-directed spatial average of its argument; the electric stress tensor has been used to determine $\langle f_y \rangle$ and $\langle f_z \rangle$ [2, 29]. The shear stress $\langle f_y \rangle$ is responsible for the motoring and generating operation of the electric induction machine. The normal stress, or pressure, $\langle f_z \rangle$ acts to collapse the air gap, and hence must be restrained by thrust bearings such as those developed in Chapter 6. Finally, the spatial average of the power dissipation density in the rotor conductor, $\langle p_R \rangle$, is given by

$$
\begin{aligned}
\langle p_R \rangle = \langle \sigma_R \, E_{G_y}^2 \Big|_{z=0} \rangle &= \langle \sigma_R \left(\frac{\partial \phi_G}{\partial y} \right)^2 \Big|_{z=0} \rangle \\
&= \sum_{m=-\infty}^{\infty} \frac{\sigma_R \beta_m^2 k_m^2 V_m^2}{2} \left(\frac{S_m^2 \omega^2 \tau_m^2}{1 + S_m^2 \omega^2 \tau_m^2} \right) \quad .
\end{aligned}
\tag{8.21}
$$

The final step in the analysis is to use the free stator surface charge density, the electric stresses acting on the rotor, and the power dissipation density in the rotor conductor, to determine the electrical and mechanical terminal variables of the electric induction machine, and the power dissipated in it. To do so, the surface charge density, the stresses, and the power dissipation density are first mapped into the cylindrical coordinates of Fig. 8.7 using (8.1). Although these quantities are not functions of x, they do become functions of r through the mapping. This dependence occurs because k_m is a function of r, and so β_m and τ_m become functions of r as well. For typical MEMS geometries, the dependence of β_m on r will likely be weak, but the dependence of τ_m on r may be strong.

Because β_m and τ_m become functions of r, $\hat{\Phi}_R$, and the electric potentials in general, become functions of r as well. The gradient of the rotor potential will therefore yield a radial electric field that drives radial currents in the rotor conductor. These currents in turn redistribute the rotor surface charges, and hence the operation of the electric induction machine, in ways that are not modeled in (8.9–8.21). However, if the conditions discussed in Section 8.2 are met, as is likely the case given typical MEMS geometries, then the unmodeled effects are inconsequential. Otherwise, Laplace's Equation must be solved in the cylindrical coordinates of Fig. 8.7.

After mapping back to cylindrical coordinates, the free stator surface charge density may be used to determine the total charge, q_n, on the electrodes of the nth phase. This charge is given by

$$
q_n(t) = P \int_{r_{IN}}^{r_{OUT}} \int_{(2n-1)\pi/NP}^{(2n+1)\pi/NP} \rho_S(r,\theta,t) r \, d\theta \, dr \quad , \tag{8.22}
$$

where r_{IN} and r_{OUT} are the inner and outer radii, respectively, of the rotor as depicted in Fig. 8.7. The time derivative of q_n is the current into the nth phase of the electric induction machine. Similarly, the two stresses can be used to determine the torque

of electric origin, T, and the normal force of electric origin, F_z, acting on the rotor. The torque and force are given by

$$T = 2\pi \int_{r_{\mathrm{IN}}}^{r_{\mathrm{OUT}}} \langle f_y \rangle(r) r^2 \mathrm{d}r \tag{8.23}$$

$$F_z = 2\pi \int_{r_{\mathrm{IN}}}^{r_{\mathrm{OUT}}} \langle f_z \rangle(r) r \mathrm{d}r \quad . \tag{8.24}$$

Finally, the power dissipation density can be used to determine to total power dissipated in the rotor conductor, P_{R}. This loss is given by

$$P_{\mathrm{R}} = 2\pi \int_{r_{\mathrm{IN}}}^{r_{\mathrm{OUT}}} \langle p_{\mathrm{R}} \rangle(r) r \mathrm{d}r \quad . \tag{8.25}$$

These quantities, in combination with the voltage applied to each phase, constitute the electrical and mechanical terminal variables of the electric induction machine, and the power dissipated in it. They directly control the power flow through the machine, as investigated in the next subsection.

8.3.2 Design and Performance

From (8.19) through (8.21), it is apparent that the electric stresses acting on the rotor, and the power dissipated in the rotor, all involve the superposition of terms proportional to V_m^2. Therefore, the behavior of the spatial fundamental, $m = 1$ in (8.6), is dominant even for machines constructed with only three phases. Correspondingly, this section investigates the design and performance of the electric induction machine as viewed primarily through its fundamental. In addition, a long-wave approximation is adopted to greatly simplify the investigation and improve its clarity. The long-wave approximation assumes that $k_1 G$, $k_1 \Delta_{\mathrm{R}}$, and $k_1 \Delta_{\mathrm{S}}$ are all much less than unity so that their hyperbolic sines and cosines are approximately themselves and unity, respectively. (As a practical matter, if each product is less than 0.4, then the error is less than 10%.) Physically, this approximation assumes that one wavelength of the stator excitation is much greater than the air gap separation and the insulator thicknesses. Also for simplicity, r_{IN} is taken to be zero, and $r_{\mathrm{OUT}} \equiv R$. As a result, the long-wave approximation will not be valid at the innermost radii, but this is not so important because phenomena at these radii make the least contribution to T, F_z, and P_{R}. When greater accuracy is required, (8.19), (8.20) and (8.21) should be used.

The objective now is to derive simple expressions for the phase charge, the torque and axial force, the input and output powers, and the efficiency of the electric induction machine. These expressions will then be used to assess performance and gain design insight. Again, these expressions will be approximations valid within the

limitations of the long-wave approximation. Beginning with (8.13) and (8.14), β_1 and τ_1 simplify to

$$\beta_1 \approx \left(1 + \frac{\epsilon G}{\epsilon_0 \Delta_R}\right)^{-1} \tag{8.26}$$

$$\tau_1(r) \approx \frac{\epsilon_0 r^2}{\beta_1 \sigma_R P^2 G} \tag{8.27}$$

after use of the long-wave approximation, and substitution for k_1 using (8.1). Next, (8.26) and (8.27) are substituted into (8.17), and (8.19) (8.20) and (8.21), which are in turn substituted into (8.22) (8.23), (8.24), and (8.25) to yield

$$q_n(t) \approx V_1 \sin\left(\frac{\pi}{N}\right) e^{j(\omega t - 2n\pi/N)}$$
$$\left(\frac{\epsilon R^2}{\Delta_S} + \frac{\epsilon_0 R^2}{G}\left(1 - \beta_1 + \beta_1 \frac{\tan^{-1}(\gamma_1)}{\gamma_1} - \frac{j\beta_1}{2}\left(\frac{\ln(1 + \gamma_1^2)}{\gamma_1}\right)\right)\right) \tag{8.28}$$

$$T \approx \frac{\pi P \beta_1 \epsilon_0 V_1^2 R^2}{4G}\left(\frac{\ln(1 + \gamma_1^2)}{\gamma_1}\right) \tag{8.29}$$

$$F_z \approx \frac{\pi \epsilon_0 V_1^2 R^2}{4G^2}\left(\frac{\tan^{-1}(\gamma_1)}{\gamma_1} + (1 - \beta_1)^2\left(1 - \frac{\tan^{-1}(\gamma_1)}{\gamma_1}\right)\right) \tag{8.30}$$

$$P_R \approx T \frac{S_1 \omega}{P} \tag{8.31}$$

$$\gamma_1 \equiv \frac{S_1 \omega \epsilon_0 R^2}{\beta_1 \sigma_R P^2 G} = S_1 \omega \tau_1 \mid_{r=R} \tag{8.32}$$

upon completing the indicated integrations. In deriving (8.28), (8.29), (8.30), and (8.31), all space harmonics except $m = 1$ have been dropped, the long-wave approximation has again been used, and the simplifications $r_{IN} \equiv 0$ and $r_{OUT} \equiv R$ have also been used. The mechanical power output from the machine, P_M, is the product of torque and rotor velocity, hence

$$P_M = T\Omega \approx \frac{\pi P \beta_1 \epsilon_0 V_1^2 R^2 \Omega}{4G}\left(\frac{\ln(1 + \gamma_1^2)}{\gamma_1}\right) \quad . \tag{8.33}$$

Combining (8.31), the equality in (8.33), and (8.15) yields an alternative expression for the power dissipated in the rotor, namely

$$P_R \approx P_M \frac{S_1 \omega}{P\Omega} = P_M \frac{S_1}{1 - S_1} \quad . \tag{8.34}$$

Then by energy conservation, the electrical power into the machine, P_E, is given by

$$P_E = P_M + P_R \approx P_M \frac{\omega}{P\Omega} = P_M \frac{1}{1 - S_1} \quad . \tag{8.35}$$

Finally, the electromechanical motoring efficiency η_M and the electromechanical generating efficiency η_G are given by

$$\eta_M = \frac{P_M}{P_E} \approx 1 - S_1 \tag{8.36}$$

$$\eta_G = \frac{-P_E}{-P_M} \approx \frac{1}{1 - S_1} \quad , \tag{8.37}$$

in which $0 < S_1 < 1$ for motoring operation, and $S_1 < 0$ for generating operation. Note that the efficiencies are based on the power balance that occurs between the electrodes of the machine and its shaft. There will always be additional electrical and mechanical losses that occur outside this domain, and hence are not represented in (8.36) and (8.37). In summary, the approximate expressions derived above can be used to assess the performance of the electric induction machine, and gain insight into its proper design. To aid in this process, a graph of $\ln{(1 + \gamma_1^2)}/\gamma_1$ is provided in Fig. 8.11.

In general, a harmonic can operate to perform one of three functions: motoring, generating, or braking. Which function it performs depends on its slip S_m, as defined by (8.15); ω is taken here to be positive without loss of generality. When space harmonic m travels at the same velocity as the rotor, then its excitation through (8.5) is stationary as viewed by the rotor, and $S_m = 0$. Correspondingly, its steady-state contribution to $\langle f_y \rangle$ and p_R, and hence T and P_R, is zero, as can be seen from (8.19) and (8.21). This can also be seen through (8.29) and (8.31) for $m = 1$, since γ_1 is
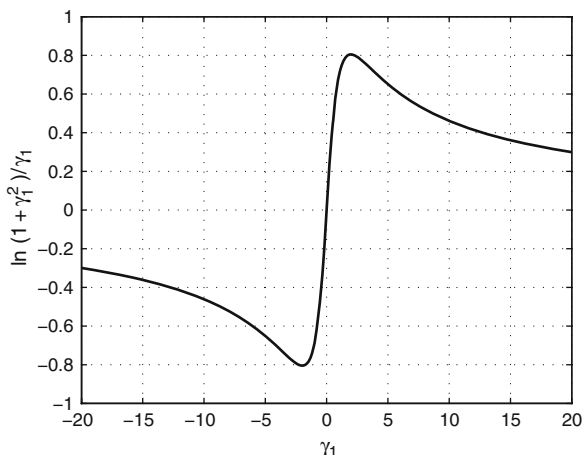

Fig. 8.11 A graph of $\ln{(1 + \gamma_1^2)}/\gamma_1$ as a function of γ_1

proportional to S_1. As the velocity of the rotor increases beyond synchronism, S_m becomes negative, as does its contribution to $\langle f_y \rangle$; its contribution to p_R, however, becomes positive. In this case, the harmonic generates, as power enters the machine through mechanical work, and exits through the electrical terminals, with some loss along the way. Conversely, as the velocity of the rotor decreases below synchronism, S_m becomes positive, as does its contribution to $\langle f_y \rangle$ and p_R. In this case, the harmonic motors, as power enters the machine through the electrical terminals, and exits through mechanical work, again with loss along the way. Finally, as the velocity of the rotor reduces to zero and below, the mechanical power reverses sign, and again enters the machine. In this case, the harmonic acts as a brake in which power enters both through the electrical terminals and through mechanical work. This power is dissipated entirely in the machine. This section will focus primarily on motoring and generating operation.

From (8.6) and (8.29), it is apparent that the torque produced by, and hence the power through, the electric induction machine increases as V^2. The principle limit to V is imposed by electrical breakdown inside the machine. As discussed in Section 8.1.1, and shown in Fig. 8.2, a realistic limit to V is approximately 300 V for an air gap. Such voltages have been successfully applied to a variety of electric MEMS devices from motors and generators, to valves to relays. In the electric induction machine, there are actually two gaps of importance to electrical breakdown, namely that between the rotor and the stator, and those between neighboring electrodes. Either gap can break down and hence limit machine performance. It is assumed here that the rotor and stator insulators have a greater breakdown strength.

From (8.6) and (8.29), it is apparent that $\beta_1 < 1$ and so $\left| V_1 - \hat{\Phi}_R \right|$ is maximized at V_1 for $S_1 = 0$. Thus, the worst case potential difference across the air gap of the electric induction machine is approximately V. At the same time, the maximum potential difference between two neighboring electrodes is given by $V\sqrt{2 - 2\cos(2\pi/N)}$, which equals V for $N = 6$, and exceeds V for smaller N. Thus, in order to maximize the permissible V, without requiring too many phases, and without losing too much to the space between them, N is chosen to be six for the electric induction machines shown in Fig. 8.9.

From (8.32), (8.33), (8.34), and (8.35) it is apparent that the power through the electric induction machine depends on the rotor surface conductivity σ_R only through the parameter γ_1. Thus, γ_1 can be considered an independent design parameter which in turn determines the required rotor surface conductivity. This is the viewpoint taken here. In the end, however, the rotor surface conductivity is restricted by fabrication and physical constraints, which may establish design trade offs. One means of constructing the rotor conductor is with a very thin layer of doped polysilicon which can exhibit a bulk resistivity ranging from 10^{-3} to 10^6 Ω·cm, depending upon the dopant and its concentration [49]. This variation, combined with permissible variations in the conductor thickness, allows for a wide range of effective rotor surface conductivities.

The dependence of torque, and hence power throughput, on γ_1 is shown in Fig. 8.11. For $\gamma_1 = 0$, the rotor and the stator excitation are in synchronism. That is, they travel at the same speed, and so the stator excitation appears to be stationary

as viewed from the rotor. In this case, charge relaxation causes the rotor charges to settle directly beneath their images on the stator, and the electric field lines between the two charges, shown in Fig. 8.10, are axially directed. No torque is produced in this case. As the stator excitation begins to slip past the rotor for $\gamma_1 > 0$, the rotor charges begin to lag the stator excitation, and the electric field lines tip as shown in Fig. 8.10. This produces a positive torque on the rotor. Eventually, the slip becomes so great that there is insufficient time to induce charge on the rotor, and so the torque drops off. The competing phenomena of charge induction and alignment for $\gamma_1 > 0$ give rise to the positive peak in Fig. 8.11. Alternatively, as the rotor begins to slip past the stator excitation for $\gamma_1 < 0$, the rotor charges begin to lead the stator excitation, and the electric field lines tip in the opposite direction shown in Fig. 8.10. This produces a negative torque on the rotor. Again, eventually, the slip becomes so great that there is insufficient time to induce charge on the rotor, and so the torque again drops off.

Motoring and generating torque can be maximized with $\gamma_1 \approx \pm 2$, respectively. In this case, $\ln(1 + \gamma_1^2)/\gamma_1 \approx \pm 0.8$, respectively. In practice, it is probably unwise to design an electric induction motor to operate in an open loop manner at the peak torque if the mechanical load can vary. For example, if the mechanical load increases beyond the peak torque, then the induction machine will slow down, which will increase S_1, thereby increasing γ_1 and further reducing torque. In this case, depending on the dependence of the load torque on speed, the motor could slow down significantly. Thus, some room for load variation is desirable from a practical viewpoint in an open-loop application.

From (8.33), it is also apparent that the power through the electric induction machine increases with decreasing G, and increasing P, R, and Ω. Beyond electrical breakdown concerns, the principle limits to decreasing G are viscous losses in the air gap, the planarity of the rotor, and the ability of the thrust bearings to hold the air gap open in the presence of F_z. Air gaps as small as 3 μm, for example, have been successfully implemented in the machines described in [30, 31, 37, 34–36, 38, 39], even with rotors having diameters approaching 1 cm. The principle limits to increasing P are the minimum feature size of the separation between electrodes, the electric field fringing that occurs as the long-wave approximation is violated, and practical limits to the resulting electrical frequency ω. Given a fixed minimum feature size, the fraction of the stator area that is allocated to the actual electrodes diminishes with increasing P. This will eventually result in a significant loss of torque as the width of the electrodes approaches the electrode separation. Generally, the electrode separation should be limited to at most 25% of the electrode width at $r = R$. The performance of machines having wider electrode separations between the electrodes must be examined with more detailed electric potential solutions than are given in (8.9), (8.10), and (8.11). Separately, as $k_1 G$ approaches 0.4, the electric fields lines emanating from the stator electrodes begin to fringe more towards the neighboring electrodes rather than being directed to the rotor. As this occurs, the torque of electric origin begins to decrease rapidly, and a further increase in P causes a reduction in torque and power throughput. Finally, the principle limits to raising R and Ω are the planarity and mechanical integrity of the rotor, and the resulting

electrical frequency. The mechanical integrity of a silicon rotor becomes limiting as the tip speed of the rotor, $R\Omega$, approaches 2000 m/s, as observed in Table 8.1. However, if the rotor carries turbomachinery blades etched into the silicon, then a limit near 500 m/s is more realistic.

Following (8.15), the electrical frequency ω is given by

$$\omega = \frac{P\Omega}{1 - S_1} \quad . \tag{8.38}$$

Given the dependence of η_M and η_G on S_1 observed in (8.36) and (8.37), $(1 - S_1)$ will likely be near unity so that $\omega \approx P\Omega$. Thus, raising both P and Ω results in an increase in ω for a given efficiency. In this case, practical electronics limits must be observed so that ω is limited to perhaps the MHz range and below as discussed in Section 8.1.1.

Finally, consider Δ_R and Δ_S. A small Δ_R allows the rotor substrate to short circuit the rotor surface conductor. This results in a reduction of torque through β_1. A small Δ_S increases the stator charge, as observed in (8.28). While this does not directly reduce power throughput, the increase in stator charge results in an increase in reactive current to the electric induction machine. This current will pass through electrode and wiring resistances, and the power electronics, and thereby create additional losses. Thus, it is desirable to make both Δ_R and Δ_S as large as possible, though there are eventually diminishing returns as $k_1 \Delta_R$ and $k_1 \Delta_S$ become large enough so that the majority of the electric fields lines do not reach the stator and rotor substrates. This may occur, however, for Δ_R and Δ_S as large as 10 times G given typical PowerMEMS geometries.

To summarize, assume that: (1) Δ_R can be made large enough so that $\beta_1 \approx 0.5$; (2) that P can be made large enough so that k_1 at $r = R$ satisfies $k_1 = PG/R \approx 0.4$; and (3) that the operation of the electric induction machine can be controlled so that the machine operates at the peak of the curve in Fig. 8.11. In this case,

$$P_M \approx 0.5 \left(\frac{\epsilon_0 V_1^2}{4G^2} \right) R^2 U \tag{8.39}$$

where $U = \Omega R$ is the peripheral tip speed of the rotor. Note that the term inside the parentheses is the spatial average of the electric energy stored in the air gap. If the slip can be set near zero, then the electromechanical efficiency of the machine will be high, and P_M in (8.39) is a good measure of the power through the machine during both motoring and generating operation. By way of example, let: $V_1 = 300$ V; $G = 3$ μm; $R = 2$ mm; and $U = 500$ m/s. In this case, $P_M = 22$ W from (8.39), which is quite high for a small device. However, it is also the case that $P = 267$, and so $\omega \approx 11$ MHz. Thus, fabrication and power electronics issues will play a significantly limiting role. Note that by way of comparison, the evaluation of (8.19) and (8.23) for the same machine and operating conditions yields $P_M = 12$ W. As expected, the simple models presented in this section are optimistic, and are best used to understand performance trends and develop design guidelines. The results

of Section 8.3.1 should be used for detailed analysis, or a Fourier–Bessel analysis of the electric potentials in cylindrical coordinates could be used for yet greater accuracy.

8.3.3 Power Electronics and Control

To achieve its best performance as a motor or a generator, the electric induction machine must be operated at both high voltage and high frequency. Voltage amplitudes near 300 V and frequencies near 1 MHz are typical for highest power throughput. In addition, the applied stator voltage waveforms should be sinusoidal. Non-sinusoidal waveforms contain time harmonics that can degrade both motoring and generating performance, and they will unnecessarily increase the peak voltage between neighboring electrodes making electrical breakdown a more limiting phenomenon. Thus, hard-switching power electronics such as those shown in Fig. 8.4 are inappropriate for the electric induction machine, and will most likely be too lossy as discussed in Section 8.1.1, particularly for generating applications. An alternative is required.

One alternative is to use resonant power electronics such as those shown in Fig. 8.12. The electric induction machine is essentially a capacitive machine. The effective capacitance at its electrical terminals, which includes any parasitic capacitance, can be used to form a resonator with an external inductor. The function of the resonator is to step the voltage from the transistors in the power electronics up to the phases of the machine. This is the approach taken in [30, 37, 34, 38, 39]. In [37–39], the low-voltage sources are themselves sinusoidal to minimize the presence of time harmonics and the associated loss. This is important during generation. However, it is possible, particularly in motoring applications, that the sources can be simple switching square-wave sources as shown in Fig. 8.4 because each resonator acts as a band-pass filter. This is the approach taken in [30, 34]. Whether or not this approach is acceptable will depend on the application. The advantage of resonant power electronics is that the transistors in the power electronics operate at a lower voltage, and so their switching losses can be greatly reduced. Voltage step-up ratios near 20 have been achieved, which lowers the transistor switching losses by a factor of 400 [30, 34].

Resonant power electronics also have important disadvantages. One disadvantage is the need to tune each phase so as to maintain a balanced excitation at the
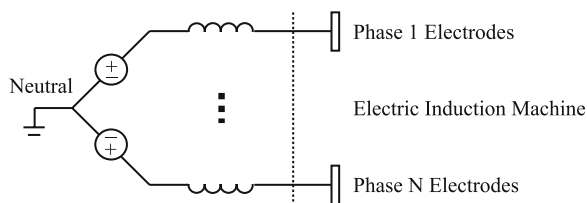

Fig. 8.12 Resonant power electronics for an electric induction machine; only two phase legs are shown

electrodes of the machine. Without a balanced excitation, the amplitudes of the space harmonics may be large enough to significantly reduce the performance of the machine, particularly when used as a generator. One source of imbalance is unbalanced parasitic capacitance in the machine itself. For example, the interconnect rings seen in Fig. 8.9 are concentric, with some rings inside others. The parasitic capacitance between these rings and the other phases will be different depending on the radius of the ring at least because the electrodes become wider as radius increases. Another source of imbalance is the inductors, no two of which will be the same. For this reason, it may be necessary to place tuning capacitors from each phase to neutral, and adjust them, and the voltage and temporal phase of the low-voltage sources, to achieve balanced excitation at the electrodes. This is done in [30, 37, 34, 38, 39]. Note that the presence of the tuning capacitors increases reactive currents and the associated losses, but the net result can be an improvement in performance. A second disadvantage is the presence of the resonating inductors, and the losses that they bring at high voltage and high frequency. Low-loss inductors having the appropriate inductance that operate at high voltage and high frequency can be physically large, and almost certainly larger than the electric machine itself. A final disadvantage is that the effective capacitance of the electric induction machine will change with operating conditions. For this reason, it may be necessary to change the excitation frequency and temporal phase shifts of the low-voltage sources so as to keep the resonator tuned at resonance.

A second alternative is to again use resonant electronics, but with a crystal as opposed to an inductor [37]. Crystals exhibit inductive behavior, although they do so only over a limited frequency range. The advantage to using a crystal over an inductor is the potential for much smaller size, and much lower loss. Preliminary experiments with crystals indicate that they can tolerate acceptably high-voltage operation.

A third alternative for providing a high-voltage and high-frequency excitation is to make use of multi-level power electronics as described in [50]. In [50], a multiphase inverter is implemented with a collection of identical single-phase inverters, one inverter per machine phase. Each single-phase inverter is in turn constructed from several identical full-bridge inverters whose outputs are transformer coupled and connected in series to produce a high net output voltage. By timing the switching of the individual inverters that constitute a single phase, the net output can be made nearly sinusoidal over a wide frequency range so that electrical breakdown between neighboring electrodes is not a limiting phenomenon. The advantages of such an inverter are again the low-voltage operation of the individual inverters that constitute a complete phase inverter. Additionally, the multi-level inverter is non-resonant, and so need not be tuned. Its primary disadvantages are the presence and size of the output transformers, and increased hardware complexity.

Finally, a fourth alternative for providing a high-voltage and high-frequency excitation is the use of piezoelectric transformers [51]. These transformers can also be used in resonant circuits to provided very-high-voltage sinusoidal outputs at very-high frequency. To date, however, they have not been pursued extensively in the context of inverters for MEMS electromagnetic machines.

The control of an electric induction machine is identical in spirit to that of a magnetic induction machine [3, 4] since the two are electromagnetic duals. As a motor, the electric induction machine may be successfully run open loop with a fixed electrical excitation, although care must be taken to anticipate the peak load so that the motor is capable of producing the necessary torque over the range of $0 \leq \gamma_1 \leq 2$. This is the manner in which most magnetic induction machines are operated today. Since it is an asynchronous machine, the electric induction machine will produce starting torque at zero speed, for which $S_m = 1$, even if it is excited at a high electrical frequency. Alternatively, a more complex control can be implemented with a controller that measures speed and adjusts the electrical excitation frequency ω so that the output torque follows the positive peak of Fig. 8.11. Yet more complex torque and speed controllers are discussed in [3, 4] in the context of magnetic machines. As a generator, the electric induction machine may also be run successfully open loop with an electrical frequency that yields negative slip, namely such that $P\Omega > \omega$. Again, more complex control is possible, such as following the negative peak in Fig. 8.11. Interestingly, the electric induction generator with resonant power electronics is capable of self excitation as discussed in Section 8.3.5, and in [37–39].

8.3.4 Special Fabrication Issues

To obtain high power throughput from an electric induction machine, the machine must run at very high speeds, perhaps hundreds of thousands to millions of revolutions per minute. In order to support such high-speed operation, air thrust and journal bearings of the type described in Chapter 6 are required. For this reason, a MEMS electric induction machine will look very much like one of the bearing test devices described in Chapter 6. The only difference will be the inclusion of stator electrodes and interconnects, and their supporting insulator, on one side of the stator, and the inclusion of a rotor conductor and its supporting insulator on the facing side of the rotor. Further, if the electric induction machine is to be integrated into a motor/compressor or a turbine/generator, then it will also look much like the turbomachinery described in Chapter 7. Thus, in order to understand the fabrication of the electric induction machine, it is first necessary to understand the fabrication of the bearing test devices and turbomachinery [52, 53]. The focus of this subsection is fabrication issues that are important to the electric induction machine, yet outside bearing test devices, turbomachinery and the main stream of Chapter 2. Additional fabrication details for specific electric induction machines may be found in [30, 31, 37, 34, 35, 38, 36, 39], which together describe the fabrication and operation of five separate machines.

8.3.4.1 Thick Rotor and Stator Insulators

As discussed in Section 8.3.2 it is desireable to fabricate the rotor conductor and stator electrodes on top of very thick insulators. That is, it is desirable to fabricate electric induction machines with large Δ_R and Δ_S. While there are diminishing

returns beyond some thickness, it is likely that insulators as thick as 20 μm or more are desirable. Silicon dioxide is the insulator considered here, and such thicknesses are well beyond those that can be obtained with thermally grown silicon dioxide. Therefore, deposited silicon dioxide, primarily densified PECVD and PECVD TEOS silicon dioxide, is used in all electric induction machines discussed in this subsection.

Because the air gaps of the electric induction machine and its thrust bearings are likely to be on the order of several microns, rotor and stator planarity is critical. Consequently, the stress internal to any thick layer of deposited silicon dioxide must be properly managed, since this stress can lead to significant wafer bow. In the electric induction machines discussed here, the stress is managed primarily by limiting the deposited insulators to those regions of the rotor and stator that are directly beneath the rotor and stator conductors. Further, to maintain planarity, the insulators are embedded in their silicon substrates so that their top surfaces are nearly flush with that of the silicon. These embedded silicon-dioxide islands are the annular region beneath the rotor conductor, and the bow-tie-shaped region beneath the stator electrodes and wiring, shown in Fig. 8.9. Alternatively [31, 36], investigate the use of a quartz stator substrate to eliminate the conducting silicon substrate, and hence the associated parasitic capacitance, altogether. This also eliminates the need for an additional thick insulator.

While their fabrication flows are similar, no two electric induction machines discussed in this subsection employ the same fabrication flows to create embedded silicon-dioxide islands on the rotor or the stator. Nonetheless, there are significant similarities worthy of note. First, all flows use the same two essential steps to create an embedded silicon-dioxide island. These steps are the dry etch of deep recesses in the silicon substrates, typically 10 μm for the rotor and 20 μm for the stator, and the subsequent deposition of silicon dioxide so that the top surface of the silicon dioxide in the recess is flush with the silicon substrate, or slightly recessed. Second, all flows either remove or substantially thin the silicon dioxide in the field regions outside the embedded islands so as to limit wafer bow. There are several ways to accomplish this. The fabrication of the early machines described in [30, 31, 34, 36] uses dry or wet etching, and/or chemical–mechanical polishing (CMP) following a fabrication flow first described in [54]. Subsequent machine fabrication described in [37, 35, 38, 39] uses lift-off to simplify the fabrication as first described in [35]. The lift-off of silicon dioxide is carried out using a 1-μm layer of sacrificial aluminum beneath the thick silicon dioxide. Following a lengthy wet sacrificial etch in HCl, the silicon dioxide breaks off cleanly at the edges of the islands leaving behind micron-scale stubs that can be removed with light CMP. The resulting wafer bow is insignificant with respect to an air gap of several microns. Third, all fabrication flows integrate the creation of the embedded silicon-dioxide islands with the preparation of the rotor and stator wafers for fusion bonding. This often involves repeated CMP and silicon dioxide deposition until a suitable bonding surface is obtained.

Upon completed fabrication, the axial gaps between the rotor and the stator will likely be very small across the radial span of the thrust bearings, stator electrodes, and rotor conductor. The bearings gaps and the electrode-to-conductor gap are typically on the order of several microns on both sides of the rotor; as discussed in

Chapter 7, the gaps across any turbomachinery can be larger. The fabrication of the narrowest gaps is best integrated with the fabrication of the thick stator and rotor insulators, since the insulators can either be recessed or used as shims to create the narrow gaps with good control. While the various electric induction machines described in this chapter manage this integration differently, they all nonetheless integrate the fabrication of the narrow gaps and the thick insulators.

8.3.4.2 Stator Electrodes and Interconnects

The fabrication of the stator electrodes is complicated by at least four factors: (1) the need for two levels of conductors to accommodate the electrodes and their interconnect rings, (2) the need for good electrical conductivity, (3) concerns for electrical breakdown, and (4) thermal exposure during subsequent fabrication, particularly during fusion wafer bonding. Good electrical conductivity is required to minimize losses. This is particularly important for generators since their stator losses come after the limiting air gap energy conversion; see Section 8.1.1. It is also important to limit electric breakdown, which ultimately limits the air-gap energy conversion in any electric induction machine. Electrical breakdown tends to initiate at sharp corners. The sharpest corners in the machine are probably at the edges of the stator electrodes. Electric breakdown will also initiate at particles, and so cleanliness is extremely important during the fabrication of an electric induction machine.

In the electric induction machines described in this chapter, the stator electrodes are connected through back-side interconnect rings, as can be seen in Fig. 8.9. This requires two levels of conductors that are separately patterned and connected through vertical vias. The overlap between electrodes and the interconnect rings from other phases leads to a parasitic capacitance between phases that is unbalanced. The imbalance arises from the electrode geometry that widens with increasing radius. The parasitic capacitance leads to reactive currents that cause loss. The imbalance also leads to undesired potential space harmonics that further decrease performance. Both effects are particularly important during generation. To minimize the parasitic capacitance, it is desireable to use a thick insulator between the two conducting layers. However, this makes via fabrication difficult given the typically narrow electrodes and interconnect rings. Separating the conductors with approximately 1 μm of TEOS silicon dioxide has been found to a good compromise.

The early stator electrodes and interconnect rings for motoring applications described in [30, 31, 34, 36] are fabricated from highly doped polysilicon because that material easily withstands the high temperatures associated with fusion wafer bonding. Even highly doped polysilicon, however, is too lossy for generating applications. It can also be difficult to pattern with smooth edges using dry etching, and so the electrodes may break down at low voltages. Subsequent machines described in [31, 36], and other machines described in [37, 35, 38, 39] use stator electrodes fabricated from 0.3-μm-thick platinum using a 10-nm titanium adhesion layer and lift-off patterning as detailed in [35]. Platinum is selected because it exhibits good electrical conductivity, it has good chemical and thermal stability, and it can lift

off smoothly leaving electrode edges that do not exhibit premature electrical break-down. In particular, the platinum electrodes can withstand all necessary chemical cleans and wafer bonding anneals up to 800°C that came after their deposition and patterning [35]. Fusion wafer bonding at temperatures as low as 700°C is described in Chapter 2, and in [37–39].

8.3.4.3 Rotor Surface Conductor

The primary fabrication challenge posed by the rotor surface conductor is its typi-cally high surface resistivity. In all electric induction machines described here, the target surface resistivity is $200 \sqrt{M\Omega}$. Correspondingly, the target surface conduc-tivity σ_R is 5 nS. To achieve this electrical behavior, the rotor conductor is fabricated as a thin layer of course-grain polysilicon, moderately doped with boron [31]. The rotor conductor thickness is designed to be 0.5 µm in order to be much thinner than the air gap, and boron is chosen as the dopant because it does not segregate at grain boundaries. The dopant dose is 5×10^{12} cm^{-2}, leading to a dopant den-sity of 10^{17} cm^{-3}. With appropriate anneals, this leads to the desired bulk resis-tivity of 10^4 Ω·cm. However, at this doping level, the resistivity of polysilicon is highly dependent on the anneal history, dopant concentration and temperature [49], and so it is difficult to control during fabrication and operation. Therefore, con-siderable variation in the rotor surface conductivity is observed in the experiments reported here.

In addition to presenting fabrication and operating challenges, lightly to mod-erately doped polysilicon presents the possibility that its conductors can be signif-icantly depleted at high air-gap field strengths. In this case, charge depletion will effectively increase the air gap, and so this phenomenon must be considered during design. To begin, the rotor surface charge density can be computed using (8.18). This charge density and the dopant concentration can then be used to compute the depth of the depletion layer. Rotor conductor depletion effects have been observed during generating experiments in [37–39].

There is perhaps a better approach to manufacturing a highly resistive rotor con-ductor that has not yet been explored. It may be possible to use highly conducting rotor electrodes that are connected to their neighbors by very thin bridges. In this case, the high apparent resistivity is achieved through the narrow geometry of the bridges, allowing the resistivity of the material to be much lower. If this option is pursued, then the number of rotor electrodes and the number of stator electrodes should probably be mutually prime to prevent cogging.

8.3.5 Experiments

Between them, [30, 31, 37, 34, 35, 38, 36, 39] describe the experimental operation of five separate electric induction machines. Motoring experiments are described in [30, 31, 34–36] and generating experiments are described in [37–39]. All machines have the same number of stator phases and electrodes, and approximately the same

geometry. They differ primarily in their fabrication details, and the manner in which the experiments were conducted. For example, the motors described in [31, 36] were tethered. That is, their rotors were suspended by springs so as to eliminate the need for, and the effects of, air bearings. This made torque easier to measure. The focus of the motor described in [30, 34] was integration into a motor/compressor application, while the focus of the motor described in [35] was higher power operation. The focus of [37–39] was generation. This subsection focuses on the experiments described in [37, 35, 38, 39].

8.3.5.1 Motoring Experiments

The parameters for the electric induction motor described in [35] are given in Table 8.4. The air gap G was smaller than the 3 μm for which it was designed due largely to the operation of the air bearings. The rotor surface conductivity σ_R was smaller than the 3 nS for which it was designed due largely to the omission of several high-temperature bonding anneals that would have promoted grain growth in the polysilicon rotor conductor.

Table 8.4 Parameters for the electric induction motor described in [35]

Parameter	Value	Parameter	Value	Parameter	Value
N	6	r_{IN}	1.0 mm	Δ_R	10 μm
P	131	r_{OUT}	1.9 mm	Δ_S	20 μm
G	1.8 μm	σ_R	1.25 nS	ϵ	3.9 $\epsilon_\circ$

Data from two motoring experiments are presented in [35]. In both experiments, the motoring torque was balanced only by the viscous losses in the air gaps. This permitted the torque to be measured via motor speed following a spin-down calibration experiment, also described in [35], and in [34]. In the first experiment, a balanced six-phase 45-V square-wave excitation was applied to the stator at electrical frequencies ranging from 50 to 600 kHz. The motor speed was recorded and converted to torque. The data from this experiment are reported in Fig. 7 of [35]. In the second experiment, a balanced six-phase 200-kHz square-wave excitation was applied to the stator with voltage amplitudes ranging from 25 to 95 V. Again the motor speed was recorded and converted to torque. The data from this experiment are reported in Fig. 8 of [35]. The data from both experiments are shown here in Fig. 8.13, although in a slightly different format. In Fig. 8.13, measured torque is normalized by the division of V_1^2, and it is plotted against the electrical slip frequency $S_1\omega$ of the fundamental. In this way, the data from both experiments can be shown in the same graph. Note that in the process, V_1 is multiplied by 0.92 to account for the spacing between the electrodes, which reduces the amplitude of the potential space harmonics.

Figure 8.13 also includes a graph of normalized theoretical torque, based on the fundamental alone as computed numerically from (8.23) using the parameters from Table 8.4. The fit between the data and the theory is good, but a better fit is
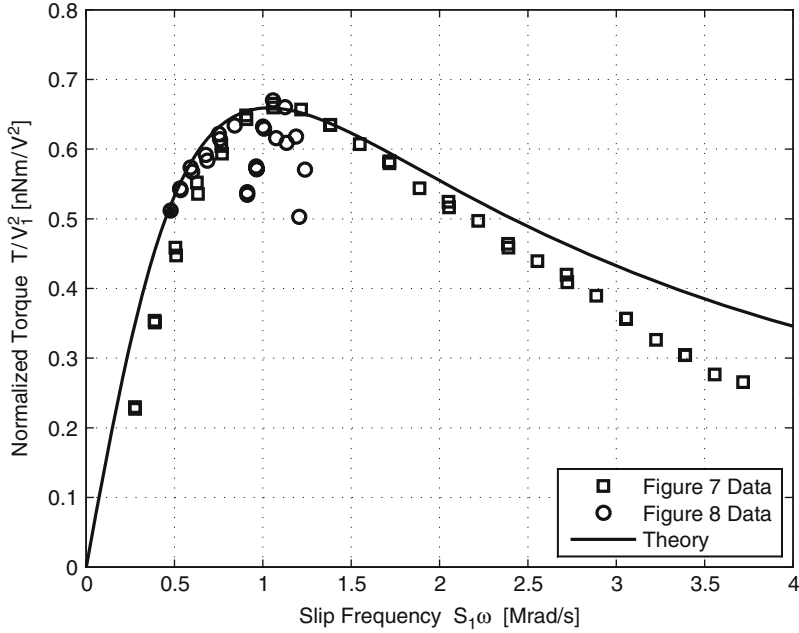
Fig. 8.13 A graph of the normalized torque T/V_1^2 versus the electrical slip frequency $S_1\omega$; the data is taken from [35]

obtained in [35] using additional space and time harmonics. The time harmonics, which are not represented in (8.4), arises from the square-wave excitation of the stator electrodes.

The greatest torque and power output from the electric induction motor was achieved during the second experiment at 95 V. The data corresponding to this experiment is identified by an solid circle in Fig. 8.13 near $S_1\omega = 0.5$ MRad/s. During this experiment, the measured torque was 3.51 μNm, the measured speed was 56.7 krpm, and the measured mechanical power was 20.8 mW. The efficiency, as determined by (8.36) was 62%. As measured, it was 61% with the additional loss coming as conduction loss in the stator wiring. In separate experiments, the stator electrodes were tested for electrical breakdown. As described in [35], the electrodes were capable of withstanding a 300-V excitation. Scaling the peak torque to full voltage would then increase it by a factor of $(300/95)^2$ to 35 μNm. At fixed speed, the power would scale up by the same factor to 0.207 W, with only 10% of that power being consumed by viscous losses in the air gap and bearings.

One interesting metric for comparison purposes is power density, computed on the basis of electromagnetically active materials. The electromagnetically active materials in the electric induction machine include the rotor and stator conductors and insulators, and the air gap. The axial length of these materials is approximately 34 μm after including the thickness of the conductors, and the insulator between the

stator electrodes and the interconnect rings. The active volume of the electric induction motor is therefore 3.9×10^{-10} m^3, which yields a power density of 54 MW/m^3 at the peak power point. If this power density is scaled up to full voltage, then it becomes 540 MW/m^3. Both are greater than the power density of a 1-GW utility generator, which approaches 20 MW/m^3. Such generators are designed to run with a peripheral tip speed near 200 m/s, a mechanically stress-limited rotor, and maximum magnetic shear stress through forced cooling.

Another interesting metric for comparison purposes is electromagnetic shear stress. If f_z in (8.23) is replaced with the average shear stress $\bar{f}_z$, then the torque is given by

$$T = \frac{2\pi}{3} \bar{f}_z (r_{OUT}^3 - r_{IN}^3) \quad , \tag{8.40}$$

from which it may be concluded that $\bar{f}_z = 286$ N/m^2 at the maximum power point. If the demonstrated average stress is scaled up to full voltage by the factor of $(300/95)^2$, then the average shear stress would be 2850 N/m^2. This is not far from the shear stress in an ordinary integral-horsepower magnetic induction motor, approximately 7 kN/m^2 [17], but it is quite far from the shear stress in a 1-GW utility generator, which approaches 180 kN/m^2.

8.3.5.2 Generating Experiments

Producing net electrical power with a microscale electric induction generator is much more difficult than producing net mechanical power with a microscale electric induction motor. The primary reason for this is the electrical losses in the machine system, which are downstream of the air gap during generation; see Fig. 8.6. These losses occur in the stator wiring and in the power electronics; the inductors in Fig. 8.12 are particularly lossy. Nonetheless, successful generation with net power output has been achieved as described in [37–39].

Eliminating electrical losses from the machine system is critical to the production of net electrical power with a microscale electric induction generator. This requires attention to many details, including: (1) reducing the resistance of the electrodes and the stator wiring; (2) eliminating parasitic capacitance inside and outside the generator; (3) maintaining a balanced sinusoidal excitation; and (4) using low-loss inductors and transistors. Each of these issues is discussed further below. In this discussion, it is assumed that resonant power electronics like those shown in Fig. 8.12 are employed. Hard-switching power electronics like those shown in Fig. 8.4 will be too lossy.

To reduce losses, all stator electrodes and wiring must be fabricated with metal. Even heavily doped polysilicon is too lossy to permit net generation. Metal electrodes, however, lead to subsequent fabrication challenges, the most noteworthy of which is wafer bonding at temperatures low enough to preserve the mechanical and electrical integrity of the metal conductors. See [37, 35] and Chapter 2 for fabrication details.

To the extent possible, all parasitic capacitance must be eliminated. This includes parasitic capacitance inside and outside the generator. Such capacitance leads to reactive currents that produce loss in the stator electrodes and wiring, and more importantly in the power electronics. Thick insulators help eliminate parasitic capacitance inside the generator, and attention to the layout of the power electronics helps eliminate parasitic capacitance outside the generator. Inside the electric induction generator, it is the capacitance between the stator electrodes and the stator substrate, and the capacitance between the stator electrodes and the interconnect rings of other phases, that make up the dominant parasitic capacitance. Outside the generator, even oscilloscope probes at the generator terminals can present excessive capacitance.

Also to the extent possible, the stator excitation should be sinusoidal and balanced as it appears at the electrodes. A non-sinusoidal excitation excites potential time harmonics inside the electric induction generator, while an unbalanced excitation excites potential space harmonics. The reactive currents associated with these harmonics will almost surely create more loss than the harmonics can generate. Further, some of the harmonics will likely motor, in which case they could consume all generated power. The dominant source of electrical imbalance is physical imbalance in the parasitic capacitance inside and outside the machine, and differences between inductors. Since these physical imbalances cannot be avoided, it is necessary to tune the power electronics so that the excitation presented to the stator electrodes is balanced, despite the imbalance outside. Time harmonics can be eliminated by using sinusoidal sources in Fig. 8.12.

At least two convenient adjustments can be made to tune the power electronics so as to produce a balanced stator electrode excitation. Both are employed in [37–39]. First, the voltage amplitudes and phase shifts of the sources driving the generator phases can be adjusted relative to that of one source chosen as the reference. Second, tuning capacitors can be placed from the external terminal of each generator phase to neutral, and these capacitors can be adjusted to help balance the parasitic capacitance. The presence of the tuning capacitors will increase the reactive currents, but their ability to eliminate imbalance is more important [37]. Executing this tuning procedure for a six-phase electric induction machine results in the tuning of 18 variables: five voltage amplitudes, five voltage phase shifts, six tuning capacitors, the fundamental electrical frequency, and the speed of the generator. Such tuning is too complex to be performed in an ad hoc manner. Consequently, a model-based approach to tuning is employed in [37–39]. This approach follows three basic steps. The first step is to develop a model of the parasitic capacitances and the inductors. The second step is to perform a set of experiments to determine the parameters in the model. The third step is to use the model to determine how to tune the power electronics, and the operation of the generator, so as to maximize the electrical output power. This approach proved to be essential to successful generation.

Finally, it is important to make use of very-low-loss inductors and transistors in the power electronics since it is in these components that most of the loss actually takes place. If voltage step-up ratios of 20 or more can be obtained, then the losses in the transistors can be made small. However, low-loss inductors that can operate at

high voltage and high frequency are considerably more challenging, and will almost certainly be bigger than the generator.

Following the approach outlined above, the electric induction generator has been successfully run to generate net electrical power. This is reported in [37–39], with [37] providing the most detail. The generator was identical to that described by Table 8.4, except for its air gap of 4.2 µm and rotor surface conductivity of 0.75 nS. With a speed of 250 krpm, an electrical frequency of 403 kHz, and sinusoidal source voltage amplitudes of 0.8 V, the electric induction generator produced 108 µW while very good correlation with the tuning model was observed. The tuning model further estimated that the efficiency of the electric machine system, from the input mechanical power to the electrical power delivered to the phase sources, was 14%; the associated power flow is tabulated in Table 8.5. However, the overall efficiency from input air power to output electrical power was estimated to be 0.036%, with turbine losses of 219 mW, air-gap viscous losses of 54 mW, and viscous bearing losses of 26.7 mW being dominantly responsible for the low overall efficiency.

Table 8.5 Electromechanical power flow in the electric induction generator described in [37–39]. The electrical output power is the total power delivered to the sources in Fig. 8.12

Phenomenon	Power [µW]
Rotor conductor loss	255
Stator wiring loss	75
Inductor loss	280
Dielectric loss	50
Proximity loss	22
Electrical output power	108
Mechanical input power	790

Experiments were also run at higher voltages in an attempt to generate greater electrical output power. However, these experiments actually yielded a lower output power due a nonlinearity in the rotor surface conductor. As explained in [37], the nonlinearity was caused by charge depletion in the rotor surface conductor.

Finally, it is also interesting to observe that the electric induction generator is capable of self excitation. To arrange for this, the sources in Fig. 8.12 are simply removed and replaced with a load. If the generator speed and the inductor inductance are properly chosen, the generator will self excite and deliver power to the load. Self excitation can be understood qualitatively from a circuit's viewpoint. From this viewpoint, each phase of the electric induction machine behaves as a (frequency dependent) capacitor in parallel with a (frequency dependent) resistor between the phase terminal and neutral, assuming that only the potential fundamental is active. When the electric induction machine operates as a generator, each phase resistor exhibits a negative resistance. If this circuit model is placed in parallel with an inductor, as is done for each phase in Fig. 8.12, and the inductor resonates with the phase capacitance at a frequency that excites the machine into generation, then the system becomes unstable due to the negative effective resistance, and the electric

generator will self excite. This mode of operation is also demonstrated in [37–39]. In the experiments reported therein, the load connected to each phase was a pair of anti-parallel light-emitting diodes (LEDs).

The same model used to guide driven generation was used to guide self-excited generation in [37–39]. Using the model, the external capacitors were tuned, the inductor inductances were chosen, and the generator speed was set to maximize the self-excited electrical output power. This yielded a maximum output power of approximately 140 µW delivered to the LED load when the turbine/generator was run at 255 krpm. In that experiment, the phase terminal voltages grew to an amplitude of 14.5 V before being limited by the nonlinearity of the rotor surface conductor. Figure 8.14 shows a photograph of the self-excited electric induction generator driving the LED load. The turbine/generator is at the center of the top of the figure. Were it not for the nonlinear rotor surface conductor, this experiment should have produced a net electrical output power of almost 3 mW if the phase voltage amplitudes were to grow to 300 V.

Fig. 8.14 A photograph of a PowerMEMS electric induction turbine/generator operating under self-excitation. The photograph is taken from [37]

8.3.6 Summary

The focus of this section has been the electric induction machine, specifically its analysis, design, microfabrication, operation, and experimental performance. To begin, an analytical model of the machine is presented in Section 8.3.1. While this model is quite detailed, it is based on several limiting assumptions. First, the stator excitation is limited to a single time harmonic. Such excitation is desireable, but not required. In more complex cases, the model can be extended in a straight forward manner to involve a Fourier expansion having multiple time harmonics [31]. Second, for simplicity and transparency, the model is built on an analysis in Cartesian geometry. In cases where this is inappropriate, as described in Section 8.2, a Fourier–Bessel analysis can be employed. Third, the model ignores the spacing

between the electrodes. If the spacing is wide, presumably to accomodate fabrication limitations, then a more complex electric potential solution is required. Finally, the model is concerned only with the core of the electric induction machine. Detailed models of the wiring between the core and the bonding pads, including parasitic resistance and capacitance, are developed in [31].

Section 8.3.2 develops a simplified model, and uses this model to design the electric induction machine within the limitation of MEMS fabrication. This design effort exposes several design trends. In an effort to maximize power throughput, a Power-MEMS electric induction machine will likely be designed with six phases, a narrow air gap, many hundreds of electrodes, and thick rotor and stator insulators. It will likely operate with phase voltages having amplitudes near 300 V and frequencies on the order of 10^5–10^6 Hz.

Section 8.3.3 discusses some of the power electronics that have been, or could be, developed for the electric induction machine. In order to avoid dominant switching losses and large power electronics, resonant power electronics are probably prefered. Resonant power electronics have so far been implemented with inductors. However, similar power electronics implemented with either crystals or piezoelectric transformers should also be explored.

Section 8.3.4 examines three aspects of the electric induction machine that require special attention during microfabrication. These are the stator electrodes, the rotor surface conductor, and the rotor and stator insulators. The stator electrodes require special attention because they should be metal for good conductivity, and smooth to avoid electrical breakdown. The presence of metal electrodes, however, complicates downstream fabrication since wafer–wafer bonding at elevated temperatures is desired. The rotor surface conductor requires special attention because it will likely be designed to be highly resistive. Further, attention should be paid to rotor conductor depletion to permit high-power operation. The stator insulators require special attention because they must be thick on an MEMS scale, and so their internal stress must be managed to preserve the planarity of the rotor and stator at the air gap.

Finally, Section 8.3.5 presents experiments involving both electric induction motors and generators. References to many more experiments are also given. The motoring experiments in particular show a very good match to the analysis provided in Section 8.3.1. Further, the experiments indicate that the electric induction motor, if run at full voltage, can produce a motive shear stress nearing that of ordinary macroscale magnetic machines. Further, Watt-level power output from a machine having a radius of 2–3 mm certainly appears possible. Even without a full-voltage stator excitation, the motor described in Section 8.3.5 achieves a power density exceeding that of most magnetic machines when computed from the volume of its electromagnetically active materials.

Generating is much more difficult than motoring due to the many electrical losses that occur downstream of the air gap. Indeed, the management of these losses is critical to successful generation, as explained in Section 8.3.5. With the losses under control, net generation is possible through both driven and self-excited operation. Such experiments are reported in Section 8.3.5.

8.4 Permanent-Magnet Synchronous Machine

Unlike the electric induction machines described in Section 8.3, the specific permanent-magnet synchronous machines described in this section have not been fully integrated into a silicon housing with self-contained air bearings. In order to achieve this integration, several challenges must be met. These challenges include: (1) the integrated fabrication of deep laminations in a silicon substrate, (2) the fabrication of multi-level three-phase windings on the stator surface, (3) the design and operation of bearings that can support a heavy magnetic rotor, and (4) the design and fabrication of a rotor that can hold together at speeds approaching 300 krpm to 400 krpm. While not described in this section, many to most of these challenges have now been met, as described in [55, 56].

The permanent-magnet synchronous machine (PMSM) consists of two-key components, a rotor with a multi-poled permanent magnet, and a stator with appropriately designed windings. During operation the rotating multi-poled permanent-magnet rotor creates a time-varying magnetic flux in the rotor–stator air gap. This flux induces AC voltages at the terminals of the stator windings, which forms the basis for power generation. The PMSMs considered in this section use an annular permanent magnet mounted on a ferromagnetic core. Interior PMSMs are not considered here due to the difficulty of embedding magnets into an electroplated ferromagnetic core. With the use of suitably thick magnets (500 μm) and high-performance magnetic materials in the rotor and stator core, the air gap can be made very large (300–500 μm) without appreciable loss of performance. This allows the stator windings to occupy space in the air gap, fabricated on the surface of a flat stator core as shown in Fig. 8.15. PMSM fabrication is thus greatly simplified. A fabricated stator is shown in Fig. 8.16.

Microscale magnetic machines can match the linear tip speeds of their macroscale counterparts by spinning much faster, reaching speeds of 100–1000 krpm. This, combined with the higher current densities allowed in the windings, enables microscale machines with very high-power densities. Microscale magnetic machines operate at electrical frequencies one to two orders of magnitude higher than typical macroscale machines, typically in the kHz to tens of kHz range, due to their higher rotational speeds. These high-operating electrical frequencies lead to smaller passive filtering components in their attendant switch-mode power electronics. The small size of microscale machines also leads to low stator inductances. This permits both generator and motor drives with fast transient responses, but also requires very high switching frequencies (hundreds of kHz to low MHz) in their power electronics.

Prior work has focused on planar MEMS PMSMs. Several axial-air-gap motors have been demonstrated [57–61], and speeds of up to 200 krpm with torques of up to 7.5 μNm have been achieved [59, 60]. Planar three-phase motors using magnetic thrust bearings have also been demonstrated [60]. Generators too have been demonstrated. One was a turbine/generator using NdFeB permanent magnets that produced 1.1 mW at 30 krpm with an air flow of 35 L/min [62]. The composite turbine/generator rotor was supported by conventional ball-race bearings, and
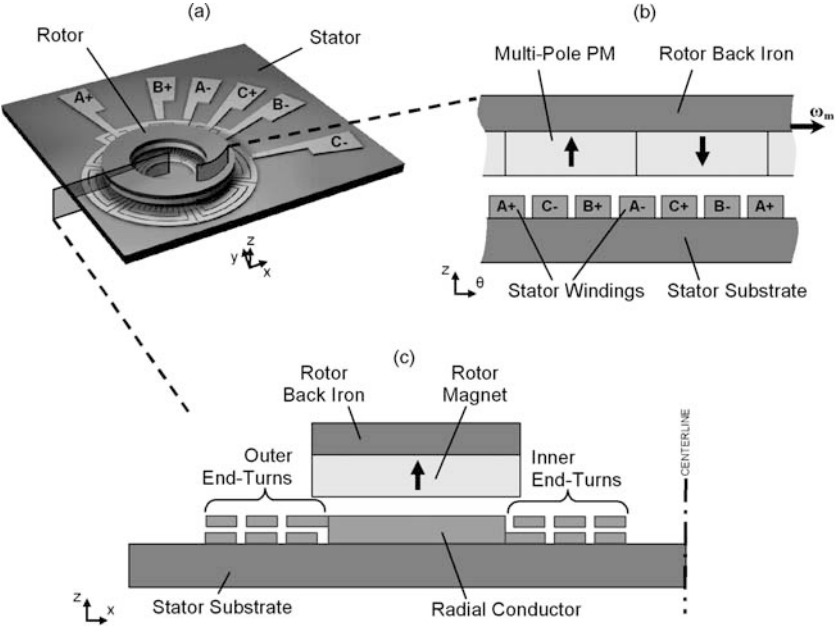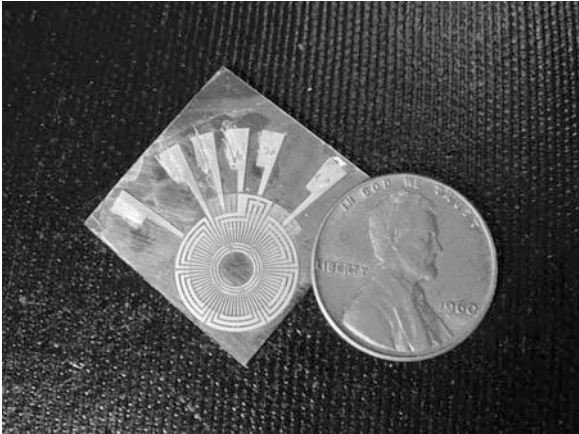
Fig. 8.15 Conceptual drawing of the **PMSM**: (**a**) perspective view, (**b**) angular cross section, and (**c**) radial cross section (Adapted from [64])

Fig. 8.16 Fabricated 3-turn/pole concentric wound stator is shown along side a penny for size comparison (Adapted from [64])

measured 1 mm in thickness and 6 mm in diameter. Another demonstrated high-speed rotation (260 krpm) by using a combination of air and magnetic bearings [63]. Using an 8-mm diameter SmCo$_5$ rotor, 14.6 mW of power was delivered to a wye-connected resistive load at 58 krpm. Using an air-powered drill and 8-mm-diameter

NdFeB permanent magnets, the same generator delivered 5 W into a wye-connected resistive load at 380 krpm.

The previous work on microscale PMSMs for power generation focused solely on the generator. This section focuses on the complete generating system, starting from the electric generator that performs the electromechanical energy conversion to the power electronics that provide usable power for portable applications. This section presents the modeling, design, and evaluation of high-speed (300+ krpm) microscale PM machines and power electronics capable of generating and delivering multi-Watt electric power to a load at a regulated DC output voltage. Unlike the electric induction machines described in Section 8.3, the PMSMs described in this section have only recently been fully integrated into a silicon housing with self-contained air bearings [55, 56]. In order to achieve this integration, several challenges were met beyond those described here. The additional challenges include: (1) the integrated fabrication of deep laminations in a silicon substrate, (2) the fabrication of multi-level three-phase windings on the stator surface, (3) the design and operation of bearings that can support a heavy magnetic rotor, and (4) the design and fabrication of a rotor that can hold together at speeds approaching 300–400 krpm.

8.4.1 Modeling

This section develops models for the planar surface-wound PMSM with laminated and unlaminated stators. The development closely follows that presented in [64, 65]. The analytic models developed here permit the quick determination of machine performance as a function of speed, physical dimensions, material properties, and input currents. The planar surface-wound PMSM is modeled by solving Maxwell's Equations in their magneto-quasistatic (MQS) form [29]. Correspondingly, the magnetic field intensity H, and magnetic flux density B, in the machine driven by the rotor magnet and stator currents are determined as functions of radius, and then integrated over the radial span of the machine to determine machine parameters such as open-circuit voltage, inductance, and torque. The field solutions are solved in the spatio-temporal frequency domain, which permits modeling of complex winding patterns and rotor magnetization profiles by decomposing them into their respective Fourier components. Performance parameters can then be determined on a harmonic-by-harmonic basis.

The continuum model presented here can be used to determine how thin the rotor and stator back iron, or cores, can be without becoming heavily saturated. It can also be used to determine hysteresis and eddy-current losses in both cores in order to predict machine efficiency as a function of speed, geometry, and material properties. The model supports these tasks by utilizing the nonlinear B–H relationship of the core materials. An iterative algorithm is first used to solve for the fields and effective permeabilities within the rotor and stator cores. Second, the field theory solutions are used to determine hysteresis losses from the nonlinear core B–H curve. Finally, the Maxwell Stress Tensor is used to find the eddy-current losses without the need to calculate current densities or evaluate volume integrals.

The field solutions are used to compute the inductance and open-circuit voltage for a single phase of the machine. Together with a simple model for the single-phase winding resistance, these parameters are summarized through an equivalent-circuit model of the PMSM. The proximity eddy-current losses in the stator windings can also be computed using the field solutions from the continuum model.

Because it contains no complicated axial structures such as poles or slots, the surface-wound PMSM can be modeled through a set of planar continuum layers as shown in Fig. 8.17. The use of two-dimensional Cartesian coordinates follows the discussion of Section 8.2. Note that Fig. 8.17 contains two parallel coordinate axes. The x-y-z axis is fixed to the stationary stator, while the x'-y'-z' axis is fixed to the moving rotor which travels with velocity U_y with respect to the stator.

Fig. 8.17 The surface-wound PMSM is modeled as a series of planar continuum layers. The interfaces between the layers are designated 1–6. The rotor layers move in the $y=y'$ direction with velocity U_y (Adapted from [64])
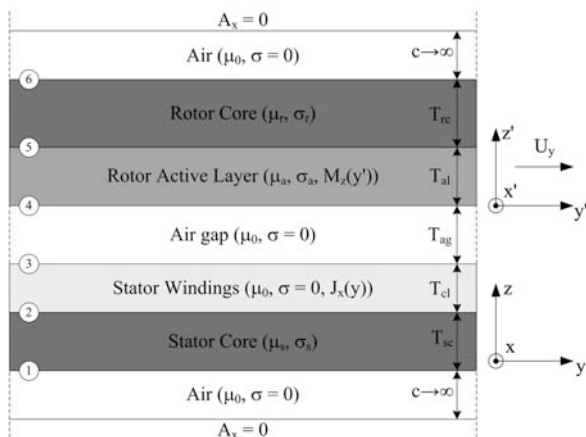
The rotor–stator air gap, as well as the space above the rotor and below the stator, are modeled as layers with permeability μ_0 and conductivity $\sigma = 0$. The rotor and stator cores are modeled as layers with permeabilities μ_r and μ_s, and conductivities σ_r and σ_s, respectively. For the purposes of modeling magnetic fields, the stator windings are modeled as a layer with zero conductivity and permeability μ_0, with an imposed current density distribution $J_x(y,t)$. The effects of proximity eddy currents within the coil layer are modeled separately. The active rotor layer has a spatially varying magnetization in the axial direction, $M_z(y')$, as well as a permeability μ_a and conductivity σ_a. It can be used to model a permanent magnet such as SmCo or NdFeB. The active layer can also model the rotor conductor in an induction machine by setting $M_z(y')$ to zero.

A two-dimensional Cartesian-coordinate convection-diffusion equation for the magnetic vector potential A, derived from the MQS Maxwell's Equations, can be solved to find the H and B fields at the radius r produced by the rotor active layer and the stator windings [29]. Each planar layer moving uniformly with velocity v_y, will have a vector potential with only one component, A_x. If no magnetization

or independent current sources exist within the layer then the convection-diffusion equation for A_x is

$$\nabla^2 A_x = \mu\sigma \left(\frac{\partial A_x}{\partial t} + v_y \frac{\partial A_x}{\partial y} \right). \tag{8.41}$$

The normal B field and tangential H field can be computed from the vector potential according to

$$H_y = \frac{1}{\mu} \frac{\partial A_x}{\partial z}, \tag{8.42}$$

$$B_z = -\frac{\partial A_x}{\partial y}. \tag{8.43}$$

Equation (8.41) governs the behavior of the vector potential in the rotor core, the stator core, the air gap, and the regions above the rotor and below the stator. In each region, μ, σ and v_y may be different; in particular, v_y is U_y for the rotor core, and zero otherwise. Equation (8.41) also governs the vector potential in an open-circuited stator-winding layer in the PMSM. For the active rotor layer with magnetization $M_z(y')$, moving uniformly with velocity $v_y = U_y$ the convection-diffusion equation for A_x, derived in [64], is

$$\nabla^2 A_x + \mu_a \frac{\partial M_z}{\partial y} = \mu_a \sigma_a \left(\frac{\partial A_x}{\partial t} + U_y \frac{\partial A_x}{\partial y} \right). \tag{8.44}$$

The current density in the stator winding layer, J_x, will be a function of y and t. For such a planar layer with current density distribution J_x, the governing equation for the vector potential is [66]

$$\nabla^2 A_x = -\mu_0 J_x. \tag{8.45}$$

The vector potential in each layer of the machine will have the form

$$A_x(y,z,t) = \text{Re} \left\{ \sum_{n=-\infty}^{\infty} \hat{A}_{xn}(z) \, e^{j(m\omega t - nky)} \right\}, \tag{8.46}$$

where m indexes the time harmonics, n indexes the space harmonics, the lowest-order time frequency is ω, the lowest-order spatial wave number k is P/r, and P is the number of pole pairs. Note that the lowest-order wavelength λ of the magnetic periodicity is $2\pi/k$. For each spatial harmonic, the complex amplitudes of the normal B field and tangential H field will be

$$\hat{B}_{zn} = jnk\hat{A}_n, \tag{8.47}$$

$$\hat{H}_{yn} = \frac{1}{\mu} \frac{d\hat{A}_n}{dz}, \tag{8.48}$$

where

$$B_z\,(y,z,t) = \text{Re}\left\{\sum_{n=-\infty}^{\infty} \hat{B}_{zn}\,(z)\,e^{j(m\omega t - nky)}\right\}, \qquad (8.49)$$

$$H_y\,(y,z,t) = \text{Re}\left\{\sum_{n=-\infty}^{\infty} \hat{H}_{yn}\,(z)\,e^{j(m\omega t - nky)}\right\}. \qquad (8.50)$$

Each layer in Fig. 8.17 is the same except for the details of its material properties (μ and σ) and velocity. The field solution for the entire machine can be found by splicing together the solutions within each layer using the appropriate boundary conditions. This approach takes advantage of the fact that the vector potential A, the normal B field and tangential H field are all continuous across the interface of two layers. Using the linear superposition of the two separate solutions, the vector potential and magnetic fields due to the stator currents and rotor magnetization can be found everywhere in the machine. These field solutions are iterated using different values for the permeability of the rotor and stator cores until the correct effective permeabilities are found so that the fields in the machine lie on the *B–H* curves of the core materials.

8.4.1.1 Rotor Magnetization Profile

For rotors with an annular permanent magnet, the magnetization impressed using a magnetic poling process does not abruptly transition between north and south poles. Instead, the magnetic remanence transitions smoothly between $+B_r$ and $-B_r$. Normally, in a macroscale machine, discrete permanent magnets are used so this transition region is not present. However, for microscale machines this effect is important because of the small dimensions involved. Therefore, the annular-rotor permanent magnets are modeled here with a trapezoidal magnetization profile having a linear "transition region" of length c_m, as shown in Fig. 8.18. This linear transition is used as a first-order approximation for computational simplicity.

Fig. 8.18 Trapezoidal magnetization profile of the annular permanent magnets. B_r is the remanent flux density of the magnets, and c_m is the transition region length (Adapted from [64])
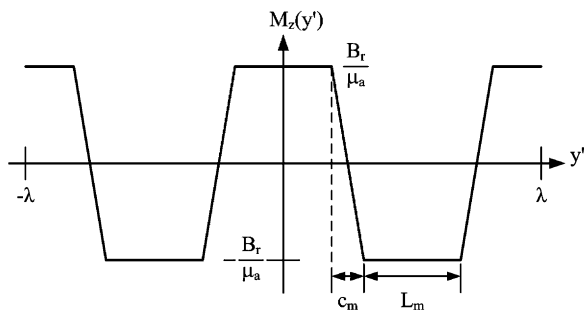
In the stationary coordinate frame, the time-varying magnetization profile can be decomposed into its Fourier harmonics according to

$$M_z (y,t) = \mathrm{Re} \left\{ \sum_{n=1,odd}^{\infty} \hat{M}_{zn} e^{jn(\omega_m t - ky)} \right\}, \tag{8.51}$$

where

$$\hat{M}_{zn} = \frac{1}{\lambda} \int_{\lambda} M_z (y') \, e^{jnky'} dy. \tag{8.52}$$

The linear velocity U_y is given by $\Omega_m r$, the rotor angular velocity multiplied by the radius. The electrical angular frequency ω_m is given by $P\Omega_m = kU_y$.

Defining the length L_m of the region in which the magnetization is uniform according to

$$L_m = \frac{\lambda}{2} - c_m = \frac{\pi r}{P} - c_m, \tag{8.53}$$

the magnitude of each magnetization harmonic becomes

$$\hat{M}_{zn} = \frac{4}{n^2 \pi^2} \frac{\lambda}{c_m} \frac{B_r}{\mu_a} cos \left(nk \frac{L_m}{2} \right). \tag{8.54}$$

Given the magnetization in (8.54), the particular solution to (8.44) is

$$\hat{A}_{xn(m)} = \frac{8}{n\pi} \frac{B_r}{n^2 k^2 c_m} cos \left(nk \frac{L_m}{2} \right). \tag{8.55}$$

8.4.1.2 Stator Current Density Profile

The windings on the surface of the stator are arranged so that a traveling magnetic field is created by the winding currents. Like the rotor magnetization, the spatially varying current density in the stator windings can be represented in terms of its Fourier harmonic components according to

$$J_x (y,t) = \mathrm{Re} \left\{ \sum_{n=-\infty}^{\infty} \hat{J}_{xn} e^{j(\omega_e t - nky)} \right\}, \tag{8.56}$$

where the current in windings is assumed to operate at the single electrical frequency ω_e. For a three-phase surface-wound machine with balanced excitation, P pole pairs, N turns per pole, and κ winding layers, the harmonic amplitudes of the current density are

$$\hat{J}_{xn} = \frac{6}{n\pi} \sin\left(n\pi \frac{W_{cl}}{\lambda}\right) J_o \sum_{\substack{v=2N'+1 \\ \text{step2}}}^{4N'-1} e^{-j\frac{n\pi}{6N'}v}, \text{for } n = 1, -5, 7, -11, 13\ldots \quad (8.57)$$

where

$$J_o = \frac{\kappa I_o}{W_{cl}T_{cl}}, \quad (8.58)$$

and $\lambda = 2\pi r/P$, $N \doteq N/\kappa$, W_{cl} is the width of the stator winding, and T_{cl} is the total height of all κ winding layers, and I_o is amplitude of the phase current. For the current density amplitudes given by (8.57) the resulting particular solution to (8.45) is

$$\hat{A}_{xn(J)} = \frac{6}{n\pi} \frac{\mu_0 J_o}{n^2 k^2} \sin\left(n\pi \frac{W_{cl}}{\lambda}\right) \sum_{\substack{v=2N'+1 \\ \text{step2}}}^{4N'-1} e^{-j\frac{n\pi}{6N'}v}. \quad (8.59)$$

8.4.1.3 Stator Laminations

The laminations are a series of thin concentric shells, as shown in Fig. 8.19. Adding laminations to the stator core creates a planar layer with non-uniform properties in the radial (x) direction which complicates the field analysis. Rather than solving Maxwell's Equations in three dimensions for a laminated stator core, a one-dimensional analysis is used to determine an effective conductivity $\sigma_{s,eff}$. The effective conductivity is then used in the two-dimensional continuum analysis derived above. The effective conductivity $\sigma_{s,eff}$ for the laminated stator core is given by [64]

$$\sigma_{s,eff} = \sigma_s \left(1 - \left|\frac{\tanh(Q)}{Q}\right|\right), \quad (8.60)$$

where

$$Q = \frac{1+j}{2} \frac{W}{\delta} \quad (8.61)$$

and

$$\delta = \sqrt{\frac{2}{\mu_s \sigma_s \omega_e}}. \quad (8.62)$$

The parameter Q describes how induced eddy currents reduce the net flux through a lamination. As the lamination width W becomes much larger than the skin depth, δ, the right-hand term inside the parenthesis in (8.60) approaches zero so that $\sigma_{s,eff} \approx \sigma_s$ and the solution in the stator core becomes that of an unlaminated stator. As W becomes much smaller than δ, this term approaches unity and the effective conductivity goes to zero.

Fig. 8.19 Laminated stator
for a planar surface-wound
magnetic machine (Adapted
from [64])
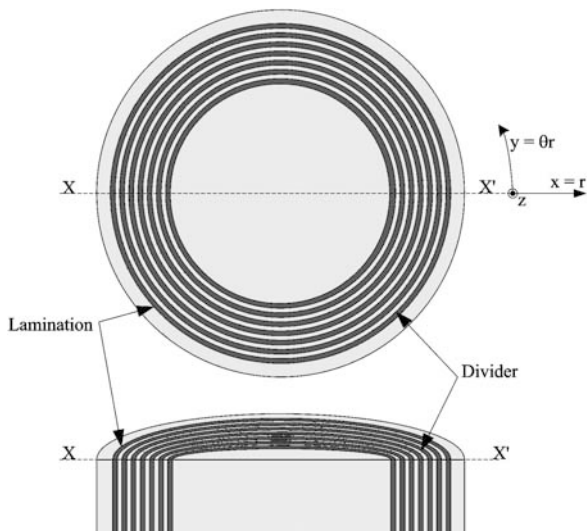
8.4.1.4 Saturation and Hysteresis Loss

Saturation effects in the machine are incorporated into the model by assigning effective permeabilities to the rotor and stator cores. The effective permeabilities are found by iteratively solving for the B and H fields until $B = \mu_{\text{eff}}H$ lies on the B–H curve of the magnetic material [64]. Since the B fields in the rotor and stator cores vary spatially over one wavelength, the root-mean-square (RMS) B field for each region is used to determine the effective permeability. For a stator consisting of laminations, the B field in the stator core will be higher than in the unlaminated case. To account for this effect, a packing factor, p_{f}, is introduced. The packing factor represents the fraction of the core that is taken up by ferromagnetic material. The RMS B field used to determine the effective permeability is increased by the factor $1/p_{\text{f}}$.

For an unlaminated stator, the fields are evaluated at the average radius $\frac{1}{2}(R_{\text{o}} - R_{\text{i}})$. The analysis of the laminated stator on the other hand is no longer continuous over the radial span of the machine. The iteration procedure is evaluated at the radius of each lamination to determine the permeability $\mu_{\text{s}}(r_{\text{lam,i}})$, where $r_{\text{lam,i}}$ is the radius of the ith lamination. Since the field solutions are computed over a continuous radial span, a permeability that varies smoothly with radius, $\mu_{\text{s}}(r)$, can be computed by interpolating between permeabilities at successive laminations, that is, between $\mu_{\text{s}}(r_{\text{lam,i}})$ and $\mu_{\text{s}}(r_{\text{lam,i+1}})$.

The hysteresis losses in the stator core are calculated using the B–H curve for the core material. The hysteresis-loss density is defined to be the energy density lost while traversing the static B–H loop. For a material with a peak flux density B_1, the hysteresis-loss density is [67]

$$\rho_{\text{core}}(B_1) = \int_{-B_1}^{B_1} H(B)\, dB. \tag{8.63}$$

For an unlaminated stator, B_1 is evaluated at the average radius of the machine. For a laminated stator, B_1 is computed for each lamination at $r_{\text{lam},i}$. The hysteresis loss is the sum of the total energy dissipated in the stator core over one hysteresis cycle times the frequency at which the *B–H* loop is traversed. For an unlaminated stator this yields

$$P_{\text{core}} = \frac{\omega_m}{2\pi} \int\int\int \rho_{\text{core}}(B_1)\,dV = \frac{\omega_m}{2}\left(R_o^2 - R_i^2\right)\int_0^{T_{sc}} \rho_{\text{core}}(B_1(z))\,dz. \tag{8.64}$$

For a laminated stator core with N_{lam} laminations the hysteresis loss is

$$P_{\text{core}} = \omega_m W \sum_{i=1}^{N_{\text{lam}}} r_{\text{lam},i} \int_0^{T_{sc}} \rho_{\text{core}}\left(\frac{1}{p_f} B_1(z)|_{r=r_{\text{lam},i}}\right) dz. \tag{8.65}$$

8.4.1.5 Eddy-Current Losses in the Stator Core

The eddy-current losses in the stator core can be found by computing the drag torque on the rotor generated by these currents. The Maxwell Stress Tensor [29] is used to find the torque on the rotor using the field solutions found for the air gap in the continuum model. The time-average shear stress at the bottom surface of the rotor permanent-magnet surface (interface 4) is

$$\langle \tau_{yz} \rangle = \frac{\mu_0}{2} \sum_n \text{Re}\left\{\hat{H}_{zn}^{(4)} \hat{H}_{yn}^{(4)*}\right\} = \frac{1}{2} \sum_n \text{Re}\left\{\hat{B}_{zn}^{(4)} \hat{H}_{yn}^{(4)*}\right\}. \tag{8.66}$$

The total time-averaged torque is $2\pi\, r^2$ times this shear stress integrated over the radial span of the machine such that

$$T_{\text{drag}} = -2\pi \int_{r=R_i}^{r=R_o} \langle \tau_{yz} \rangle r^2 dr. \tag{8.67}$$

Note that the minus sign in front of the integral in (8.67) is due to the fact that integration is performed over bottom surface of the rotor permanent magnets, which has a normal in the $-\hat{z}$ direction. The eddy-current losses in the machine are then

$$P_{\text{eddy}} = \Omega_m T_{\text{drag}}. \tag{8.68}$$

Physically, the drag torque T_{drag} manifests as eddy-current loss and stator-core heating. It can be reduced by using a ferrite or a laminated core.

8.4.1.6 Proximity Eddy Current Losses in the Coil Layer

The continuum model of the surface-wound PMSM does not model the stator windings as a layer with conductivity σ_c because the windings are made of discrete conductors. The width of each conductor is much smaller than a magnetic wavelength. The coil layer is instead treated as a layer with zero conductivity and an imposed current density $J_x(y,t)$ in the continuum model. However, eddy currents within each radial conductor will be present. These eddy currents are driven by the magnetic fields from the rotor permanent magnets, and the resulting losses are modeled separately using the field solutions from the continuum model. If the losses due to these eddy currents are too large, they can be reduced by laminating the radial conductors. There are 6PN radial conductors in a surface-wound stator. If each of these conductors has C_{lam} laminations, then the total loss due to proximity eddy currents is [64, 65]

$$
P_{prox} = \frac{3\sigma_c \omega_m^2}{64\pi} (PNC_{lam})^2 T_{cl} \left[W_{cl} (R_o)^4 - W_{cl} (R_i)^4 \right] \sum_{n=1,\text{odd}}^{\infty} n^2 \left| \hat{B}_{zn,\text{coil}(m)} \right|^2,
$$

where $\hat{B}_{zn,\text{coil}(m)}$ is flux density at half the thickness of the coil layer due the rotor PM.

8.4.1.7 Equivalent Circuit Model

The equivalent circuit for a single phase of a balanced PMSM is shown in Fig. 8.20. It consists of a back EMF source, or open-circuit voltage V_{oc}, due to the spinning permanent magnets, as well as an inductance L_s, and resistance R_s, due to the stator windings. The open-circuit voltage and stator inductance can be found using the vector potential solutions within the machine due the rotor magnetization and stator currents, respectively. The resistance is calculated from the dimensions of the radial conductors, and the inner and outer end turns of the stator windings.

Fig. 8.20 Equivalent circuit for a single phase of a PMSM consisting of an open-circuit voltage V_{oc}, stator winding inductance L_s, and resistance R_s (Adapted from [64])
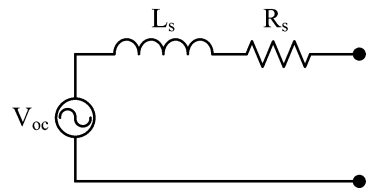
Open-Circuit Voltage

The spinning multi-pole permanent-magnet rotor creates a time-varying flux that induces the voltage V_{oc} on each phase of the stator windings governed by Faraday's Law according to

$$V_{oc} = \frac{d\lambda_m}{dt}, \tag{8.70}$$

where λ_m is the total flux from the rotor permanent magnets linked by a single phase. In order to determine the open-circuit voltage, the axial flux through a single phase of the stator windings must be found. This is achieved by integrating the incremental flux at a given radius over the radial span of the machine. The incremental flux from a single turn can be found by taking the difference between the vector potential of the two radial conductors in that turn [29].

For a three-phase surface-wound machine with P pole pairs, N turns per pole, and κ winding layers, the incremental flux per phase is [64, 65]

$$\hat{\Phi}_{zn,\mathrm{coil}(m)} = 2\kappa P \hat{A}_{xn,\mathrm{coil}(m)} \sum_{\substack{\nu=2N'+1 \\ \mathrm{step2}}}^{4N'-1} e^{j\frac{n\pi}{6N'}\nu}, \tag{8.71}$$

where $\hat{A}_{xn,\mathrm{coil}(m)}$ is the vector potential evaluated at half the axial thickness of the stator winding layer, and $N' \triangleq N/\kappa$. Equation (8.71) works for both full-pitched and concentric-wound stators. Integrating over the radial span of the machine, the total flux linked by a single phase for each harmonic is

$$\hat{\lambda}_{n,\mathrm{coil}(m)} = \int_{r=R_i}^{r=R_o} \hat{\Phi}_{zn,\mathrm{coil}(m)} dr. \tag{8.72}$$

The harmonic amplitude of the open-circuit voltage induced by this flux is then

$$\hat{V}_{ocn} = \frac{d}{dt}\hat{\lambda}_{n,\mathrm{coil}(m)} = jn\omega_m\hat{\lambda}_{n,\mathrm{coil}(m)}. \tag{8.73}$$

Stator Inductance

The stator inductance can be determined in the same manner as the open-circuit voltage. The total flux generated by the stator currents and linked by a single phase of the machine is found by integrating the incremental flux at a given radius over the radial span of the machine. The incremental flux linked by a single phase is P times the incremental flux per pole. For a three-phase surface-wound machine with P pole pairs, N turns per pole, and κ winding layers, the incremental flux per phase is [64, 65]

$$\hat{\Phi}_{zn,\mathrm{coil}(J)} = 2\kappa P \hat{A}_{xn,\mathrm{coil}(J)} \sum_{\substack{\nu=2N'+1 \\ \mathrm{step2}}}^{4N'-1} e^{j\frac{n\pi}{6N'}\nu}, \tag{8.74}$$

where $\hat{A}_{xn,\mathrm{coil}(J)}$ is the vector potential due to the stator currents evaluated at half the thickness of the stator winding layer, and $N' \triangleq N/\kappa$.

The stator currents, which have the single temporal frequency ω_e, generate magnetic fields with multiple spatial harmonics. However, due to the large air gap, the higher-order harmonics are much smaller than the fundamental. Therefore, the flux linked by a winding due to the stator currents is dominated by the fundamental component of the magnetic field in the air gap. Integrating over the radial span of the machine, the flux linked by a single phase is then

$$\hat{\lambda}_{\text{coil}(J)} = \int_{r=R_{\text{i}}}^{r=R_{\text{o}}} \hat{\Phi}_{z1,\text{coil}(J)} dr. \tag{8.75}$$

Note that this is the flux linkage generated by the sum of the three phase currents. The resulting inductance, L_{d}, is referred to as the synchronous inductance [1] and is given by

$$L_{\text{d}} = \frac{\text{Re}\left\{\hat{\lambda}_{\text{coil}(J)}\right\}}{I_{\text{o}}}. \tag{8.76}$$

In a balanced machine, the Phase-B and Phase-C currents produce a flux linked by Phase A that is scaled by $\cos(\pm 2/3\pi) = -\frac{1}{2}$. Since $i_{\text{b}} + i_{\text{c}} = -i_{\text{a}}$, the sum of the fluxes produced by Phases B and C equals half the flux produced by Phase A. Therefore, Phase A will link 1.5 times the flux produced by currents in only Phase A during balanced operation. Therefore, the stator phase inductance, L_{s}, in the single phase model will be

$$L_{\text{s}} = \frac{2}{3I_{\text{o}}} \text{Re}\left\{\hat{\lambda}_{\text{coil}(J)}\right\}. \tag{8.77}$$

Stator Resistance

For a surface-wound PMSM, the radial conductors of all three phases will occupy the same winding layer. Radial conductors in the same phase are connected by concentric end turns. Figure 8.21 shows a two-turn-per-pole stator with concentric windings. The width of the radial conductors, W_{cl}, is a function of radius r. Each outer end turn has a width W_{co} and each inner end turn has a width W_{ci}. The conductors are separated from each other by a width g_{cl}.

There are $2PN$ radial conductors per phase. Given C_{lam} laminations per radial conductor, the resistance of all the radial conductors in a single phase is [64]

$$R_{\text{radial}} = \frac{6\,(PNC_{\text{lam}})^2}{\pi \sigma_{\text{c}} T_{\text{cl}}} \ln\left(\frac{W_{\text{cl}}\,(R_{\text{o}})}{W_{\text{cl}}\,(R_{\text{i}})}\right), \tag{8.78}$$

where T_{cl} is the height of the radial conductor and σ_{c} is the conductivity of copper. If N is even, there will be $N/2$ short-pitched windings and $N/2$ long-pitched windings. If N is odd, their will be one full-pitched winding, $(N-1)/2$ short-pitched windings and $(N-1)/2$ long-pitched windings. The arcs spanned by the nth inner and outer end turns are, respectively,

Fig. 8.21 End turn
connections for a
2-turn-per-pole concentric
winding (Adapted from [64])
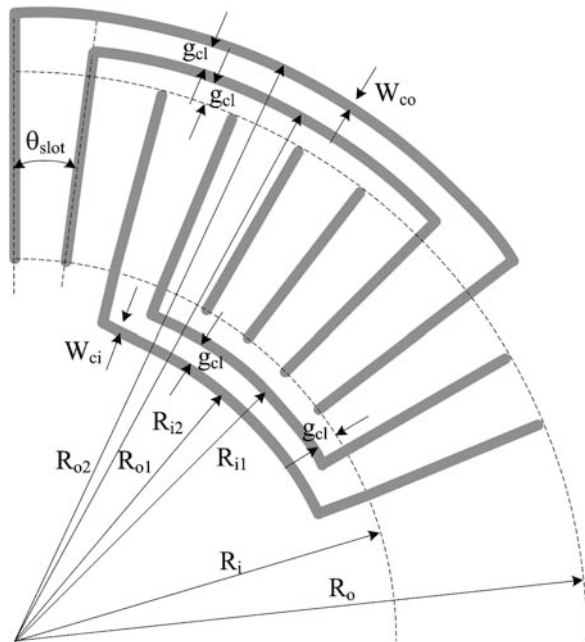
$$L_{\text{inner}(n)} = \frac{[2(N+n)-1]\pi R_{\text{i}(n)}}{3PN}, \tag{8.79}$$

$$L_{\text{outer}(n)} = \frac{[2(N+n)-1]\pi R_{\text{o}(n)}}{3PN}, \tag{8.80}$$

where the radii of the arcs are

$$R_{(n)} = R_{\text{i}} - \frac{2n-1}{2}W_{\text{ci}} - ng_{\text{cl}}, \tag{8.81}$$

$$R_{(n)} = R_{\text{o}} + \frac{2n-1}{2}W_{\text{co}} + ng_{\text{cl}}. \tag{8.82}$$

The total resistance of the inner and outer end turns is then

$$R_{\text{inner}} = P\sum_{n=1}^{N}\frac{L_{\text{inner}(n)}}{\sigma_{\text{c}}T_{\text{ci}}W_{\text{ci}}} = \frac{\pi}{\sigma_{\text{c}}T_{\text{ci}}W_{\text{ci}}}\sum_{n=1}^{N}\frac{[2(N+n)-1]R_{(n)}}{3N}, \tag{8.83}$$

$$R_{\text{outer}} = P\sum_{n=1}^{N}\frac{L_{\text{outer}(n)}}{\sigma_{\text{c}}T_{\text{co}}W_{\text{co}}} = \frac{\pi}{\sigma_{\text{c}}T_{\text{co}}W_{\text{co}}}\sum_{n=1}^{N}\frac{[2(N+n)-1]R_{(n)}}{3N}. \tag{8.84}$$

The total stator resistance per phase is $R_s = R_{radial} + R_{inner} + R_{outer}$.

8.4.1.8 Simplified Open-Circuit Voltage Equation

The continuum model is fast and accurate, but also complex. To derive analytical insight into how various parameters affect the open-circuit voltage, the continuum model can be simplified. To do so, let the magnetization profile approach an ideal square wave ($c_m \to 0$). Also, assume that the rotor and stator cores and active rotor layer are ideal such that $\mu_r = \mu_s \to \infty$, and $\sigma_r = \sigma_s = \sigma_a = 0$. In addition, assume that the magnetic wavelength λ is much larger than the thicknesses of the air gap, stator windings, rotor permanent magnets, and rotor and stator cores. With the last approximation, the exponential decay of the fields in the machine can be ignored. In addition, the B and H fields are assumed to be independent of radius. The magnetic wavelength of the rotor is also independent of the radius, and the wave number k is evaluated at the mean radius. Given these approximations, the vector potential evaluated at half the thickness of the stator winding layer is

$$\hat{A}_{xn,\text{coil}(m)} = -j\frac{(R_o + R_i)}{P} \left(\frac{T_{al}}{T_{al} + T_{cl} + T_{ag}} B_r \right) \frac{2}{n^2\pi} \sin\left(\frac{n\pi}{2} \right). \qquad (8.85)$$

The corresponding incremental flux per phase reduces to

$$\hat{\Phi}_{zn,\text{coil}(m)} = 2PN\hat{A}_{xn,\text{coil}(m)}e^{j\frac{n\pi}{2}} = (R_o + R_i) \left(\frac{T_{al}}{T_{al} + T_{cl} + T_{ag}} B_r \right) N\frac{4}{n^2\pi}. \qquad (8.86)$$

Since (8.86) is independent of the radius, the flux linked by a phase becomes

$$\hat{\lambda}_{n,\text{coil}(m)} = (R_o - R_i)\hat{\Phi}_{zn,\text{coil}(m)} = \left(R_o^2 - R_i^2 \right) \left(\frac{T_{al}}{T_{al} + T_{cl} + T_{ag}} B_r \right) N\frac{4}{n^2\pi}. \qquad (8.87)$$

while the harmonic amplitudes of the open-circuit voltage become

$$\hat{V}_{ocn} = jn\omega_m\hat{\lambda}_{n,\text{coil}(m)} = j\left(R_o^2 - R_i^2 \right) \left(\frac{T_{al}}{T_{al} + T_{cl} + T_{ag}} B_r \right) NP\Omega_m \frac{4}{n\pi}. \qquad (8.88)$$

The voltage harmonics can be added to generate the total open-circuit voltage

$$V_{oc}(t) = \mathrm{Re}\left\{ \sum_{n=1,\text{odd}}^{\infty} \hat{V}_{n,\text{coil}(m)}e^{jn\omega_m t} \right\} = V_o \sum_{n=1,\text{odd}}^{\infty} -\frac{4}{n\pi} \sin(\omega_m t), \qquad (8.89)$$

where

$$V_o = \left(R_o^2 - R_i^2 \right) \left(\frac{T_{al}}{T_{al} + T_{cl} + T_{ag}} B_r \right) NP\Omega_m. \qquad (8.90)$$

The term inside the summation of (8.89) is the nth Fourier component of a square wave. Therefore the open-circuit voltage due to a square wave magnetization is also a square wave with magnitude V_o. The first term in the parentheses in (8.90) shows how the open-circuit voltage scales with the active area of the machine. The second term in parentheses is the B field in the air gap, and indicates that the thickness of the rotor permanent magnets should be larger than the thickness of the coil layer and physical air gap combined in order to maximize the flux generated from the permanent magnets. Lastly, the open-circuit voltage scales linearly with B_r, N, P, and Ω_m.

8.4.2 Design

The surface-wound PMSM was chosen as the best candidate for efficient high power generation in the microengine. This section focuses on the design of a microscale PMSMs capable of generating and delivering Watt-level power at speeds of approximately 300 krpm. The emphasis will be on DC power generation via power electronics that rectify the AC voltages delivered by the generator phases. Since integration issues are not dealt with at this stage, silicon wafers and electroplated core materials will not be used. Instead, a ferromagnetic wafer will be used as the stator core. Since this wafer will not be laminated, eddy current losses will degrade efficiency but will not affect output power provided that the turbine that spins the rotor provides sufficient mechanical power to overcome the added losses. Integration issues are addressed in [55].

The PMSMs considered here are three-phase axial-air-gap machines. Each machine consists of a rotor with an annular multi-pole permanent magnet and ferromagnetic core, and a stator with multi-turn windings on the surface of a ferromagnetic substrate which serves as the stator back iron as shown in Fig. 8.22. During operation, the rotating multi-poled permanent-magnet rotor creates a time-varying magnetic flux in the rotor–stator air gap, which induces AC voltages at
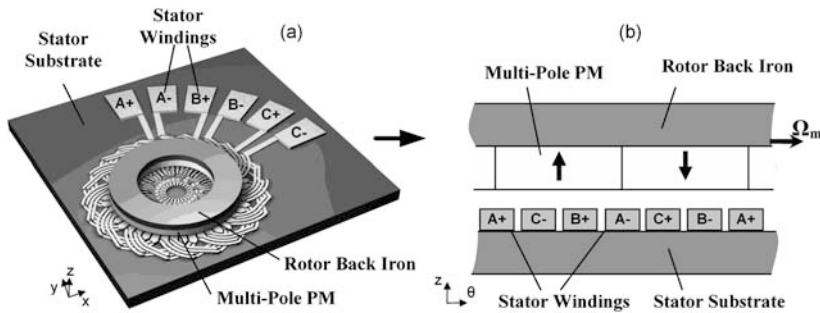

Fig. 8.22 Conceptual drawing of the PMSM: (**a**) perspective view and (**b**) cross-section (Adapted from [64])

the terminals of the stator windings. The magnetic flux generated by the permanent magnets can be concentrated in the rotor–stator air gap by using cores with very large permeabilities. By using rare earth permanent magnets, which have large remanences ($\sim$1 T), strong magnetic fluxes can be generated in the air gap. In fact, by using high-performance magnetic materials (permanent magnet, and rotor and stator cores) and suitably thick magnets ($\sim$500 µm), the actual rotor–stator air gap can be made relatively large (300–500 µm) to reduce windage loss while maintaining high magnetic flux in the air gap. Thus, the stator windings can be hundreds of microns thick and occupy space in the air gap on the surface of the stator substrate.

The simplified model of the PMSM will be used to derive the scaling laws that allow optimization of the physical and electrical parameters of the machine. The open circuit voltage scales as

$$V_{\text{oc}} \propto \left(\frac{T_{\text{al}}}{T_{\text{al}} + T_{\text{cl}} + T_{\text{ag}}} \right) NP\Omega_{\text{m}}. \tag{8.91}$$

The total resistance per phase [65, 68] scales as

$$R_{\text{s}} \propto \frac{1}{T_{\text{cl}}} \left[k_1 (PN)^2 + k_2 PN \right]. \tag{8.92}$$

The k_1 term represents the resistance of the radial conductors which grows as PN squared, while the k_2 term represents the resistance of the inner/outer end turns which grow linearly with PN. Even though the end turn resistance grows more slowly, it can make up a large fraction of the over all resistance. In addition, the resistance is inversely proportional to the thickness of the radial conductors that make up the coil layer. Equation (8.92) assumes the thickness of the inner and outer end turns are a constant fraction of the coil layer.

Combining (8.91) and (8.92), the output power capability of a PMSM scales approximately as

$$P_{\text{out}} \propto \frac{V_{\text{oc}}^2}{R_{\text{s}}} \propto \left(\frac{T_{\text{al}}}{T_{\text{al}} + T_{\text{ag}} + T_{\text{cl}}} \right)^2 T_{\text{cl}}. \tag{8.93}$$

Equation (8.93) contains important information about the relative thicknesses of the active layer, air gap, and coil layer in order to maximize output power. First, the air gap should be made as small as possible. Second, for a given coil layer and air gap thickness, power is maximized as the term inside the parentheses approaches unity. Finally, taking the derivative of (8.93) with respect to T_{cl}, the maximum output power for a fixed air gap and active layer thickness is

$$T_{\text{cl}} = T_{\text{al}} + T_{\text{ag}}. \tag{8.94}$$

Thus, for a fixed air gap and active layer thickness, the coil layer should equal the sum of the two. The maximum thickness for the rotor permanent magnets is 500

μm, set by microengine wafer-thickness constraints. The maximum height of the coil layer is 200 μm due to fabrication constraints. So, for a given coil thickness, the maximum power is achieved by setting T_{al} to its maximum value, while for a given rotor permanent magnet thickness, the maximum power is achieved by setting T_{cl} to its maximum. Thus, the maximum power is achieved when T_{al} is set to 500 μm and T_{cl} is set to 200 μm.

To optimize N and P, scaling laws for the power electronic losses are required. Some losses in the power electronics are independent of frequency, such as conduction loss in the on-state resistance of a power MOSFET. Others are proportional to the square root of the electrical frequency, such as skin depth losses in the windings of high-frequency transformers. Still others grow linearly with frequency, such as the switching loss of a power MOSFET. The frequency-dependent components are the most important because they scale with both the speed and number of pole pairs of the machine. To model these losses, the effective power-electronics resistance R_{pe}, will be assumed to be proportional to $P\Omega_m$ because the fastest growing frequency-dependent component scales linearly. Thus

$$R_{pe} \approx k_3 P \Omega_m. \tag{8.95}$$

Since the load resistance can be expressed as some fraction of $R_s + R_{pe}$, the overall output power of the generator and power electronics scales as

$$P_{out} \propto \frac{V_{oc}^2}{R_s + R_{pe}} \propto \frac{(PN\Omega_m)^2}{k_1(PN)^2 + k_2 PN + k_3 P\Omega_m}. \tag{8.96}$$

By making N large, both the open-circuit voltage and stator resistance increase, while dissipation in the power electronics remains the same leading to higher output power. In addition, for large N, P_{out} will be independent of both P and N, and scale with the square of the rotational speed. In reality, the minimum feature size constraint will limit the gap between adjacent radial conductors, and so a large number of turns per pole will lead to thin inner and outer end turns. Both effects make R_s increase slightly faster than N^2. Therefore, to maximize output power, the number of turns per pole should be maximized subject to stator fabrication and surface area limitations.

The total generator system efficiency can be expressed as

$$\eta_g = \frac{P_{out}}{P_{out} + P_{prox} + P_{core} + P_{cond} + P_{pe}}, \tag{8.97}$$

where P_{cond} is the loss in the stator windings and P_{pe} is the loss in the power electronics. P_{core} is the sum of the stator core eddy current and hysteresis losses. The eddy current loss is either proportional to frequency squared (skin depth > core/lamination thickness) or linear with frequency (skin depth < core/lamination thickness). The hysteresis loss is linear with frequency. In the worst case,

$$P_{core} \propto k_4(P\Omega_m)^2 + k_5 P\Omega_m. \tag{8.98}$$

Thus, the generator system efficiency can be increased by making P small. However, doing so will make the rotor permanent-magnet poles wide. Consequently, the rotor and stator cores must be made thicker to prevent them from saturating. The proximity skin effect losses, P_{prox}, are approximately independent of P [64, 65] and scale as speed squared. However, proximity losses decrease as N squared. Therefore, to maximize efficiency, the number of poles should be minimized subject to rotor and stator core thickness limitations while the number of turns/pole should be maximized subject to stator fabrication and surface area limitations. Optimization of the output power and efficiency [64, 69] resulted in a stator with 8 poles and 3 turns per pole.

8.4.2.1 Stator Design

The stator uses interleaved, multi-layer electroplated copper windings that are dielectrically isolated from a 1-mm thick $Ni_{80}Fe_{15}Mo_5$ (Moly Permalloy) substrate by a 3-μm spin-on-glass layer and/or a 5-μm polyimide layer. The active area of the stator has an outer diameter of 9.5 mm, and an inner diameter of 5.5 mm. NiFeMo is selected as the stator core (substrate) for its combination of high permeability ($\mu_r > 10^4$), low coercivity ($H_c \sim 0.16$ A/m) to minimize hysteresis losses, and commercial availability in sheets of suitable thickness [70].

An optimized 2nd-generation 8-pole 3-turn-per-pole stator is shown in Fig. 8.23. The winding pattern is designed for minimal resistance to ensure optimal generator performance. These stators use a single layer for the radial conductors that are 200 μm thick. The end turns occupy two layers and are each 80 μm thick. There is a 40 μm thick SU8 insulation layer between the top and bottom end turns. The stators use concentric windings, shown in Fig. 8.24, in which a complete end turn occupies
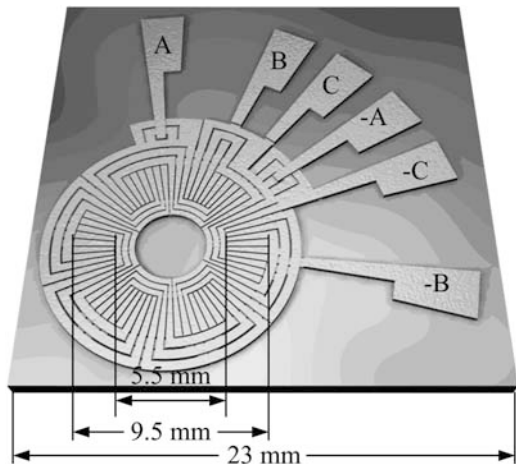

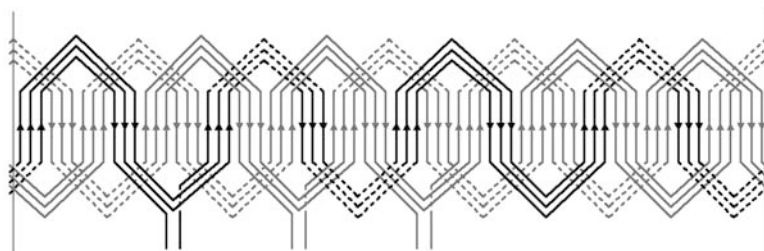**Fig. 8.23** 8-pole, 3-turn/pole concentric wound stator (Adapted from [64])

Fig. 8.24 Winding diagram for the 3-turn-per-pole concentric-wound stator. *Solid lines* represent end turns on the top layer while *dashed lines* represent end turns on the bottom layer. The radial conductors, marked with *arrows*, occupy both coil layers. Phase A is *darkened* for reference (Adapted from [64])

a single layer. This eliminates the need for cross-over conductors like the ones used in the 1st-generation stators [65, 68]. In fact, the only cross-over conductors needed are for connections to the pads. With fewer crossovers the number of vias is greatly reduced, from 96 down to 3. In addition, by using concentric windings, the end turns can be made to be circular arcs. This makes much more efficient use of the surface area of the inner and outer regions of the stator than the triangular end turns used in the 1st-generation devices [68]. Furthermore, variable-width coils are used with the gaps between adjacent radial conductors and end turns equal to 50 μm rather than 130 μm. The combination of the reduced number of vias, better end turn design, and more aggressive fabrication leads to a predicted stator resistance of 100 mΩ. This resistance is about the same as that of a 1st-generation 2-turn-per-pole machine. In fact, the predicted output power capability is increased by a factor of 2.25 over the 2-turn-per-pole machines presented in [68] due to the improved stator resistance.

8.4.2.2 Rotor Design

The rotor contains an 8-pole, annular, pressure-formed (sintered) Sm_2Co_{17} permanent magnet and a ferromagnetic $Fe_{49}Co_{49}V_2$ (Hiperco 50) core, as shown in Fig. 8.25. The rotor components are mounted in a titanium adaptor for assembly onto a 1.6-mm diameter shaft for testing. The permanent magnet and rotor core are 500 μm thick to be compatible with standard wafer thicknesses, and have an outer diameter of 10 mm and inner diameter of 5 mm. This outer diameter was chosen because it was the closest match to the 10-mm outer diameter of the microengine generator.

SmCo magnets were selected for their combination of high-energy product (BH_{max} ~240 kJ/m^3) for high-energy conversion, and high-operating temperatures (T_{max} ~300°C) [71]. Although NdFeB has a higher energy product (BH_{max} ~400 kJ/m^3), it does not provide the necessary operating temperatures (T_{max} ~150°C) for integration with the combustion-driven microengine [71]. However, it would be suitable for a low-temperature turbine generator. Hiperco 50 was selected for the rotor core for its combination of a reasonably high permeability ($\mu_r > 3000$),
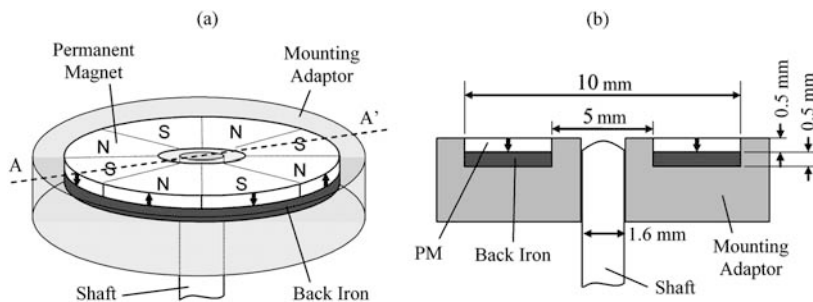
Fig. 8.25 Schematic (**a**) perspective view and (**b**) cross-section of the PM machine rotors. Note that the rotor is shown upside down (Adapted from [64])

and its high saturation flux density ($B_s \sim 2.4$ T) to minimize the thickness of the cores while avoiding magnetic saturation [70]. Note that the fields in the rotor core are nearly time-invariant, so the coercivity of the rotor back iron is not a major concern.

8.4.3 Power Electronics

For the microengine system to replace batteries, it must provide a constant DC output voltage. The PMSM presented in the previous section produces a three-phase AC voltage. A PMSM can work with both passive and active power electronics to create a DC output voltage. If the microengine is to provide a 12-V battery replacement, for example, then the power electronics must rectify and boost the AC voltages from the generator, while operating under closed-loop control to provide a regulated output voltage.

One way to passively step up and rectify the AC voltages is to use a Δ/wye-connected transformer and diode bridge rectifier as shown in Fig. 8.26. The generator windings are connected in a wye configuration and tied to the Δ-connected primary side of the transformer. This gives an additional factor-of-three increase from the line-to-neutral voltage of the PMSM to the line-to-line voltage on the transformer secondary side. A linear regulator at the output of the rectifier can then be used to achieve output voltage regulation.

Passive electronics, however, tend to be large and bulky. Transformers designed for use in the stator electrical frequency range of 10–20 kHz can be very large compared to the PMSM. The three-phase transformer used in [68] is eight times the volume of the PMSM stator. In addition, the transformer/diode bridge combination cannot provide power factor correction. Power factor correction is important at high speeds where the machine and transformer inductances will start to create a phase lag in the generator current relative to the generator voltage, reducing output power capability. At only 100 krpm the power factor for the transformer and diode bridge is 93.4%. At 300 krpm, the power factor drops to 90% while at 500 krpm the power
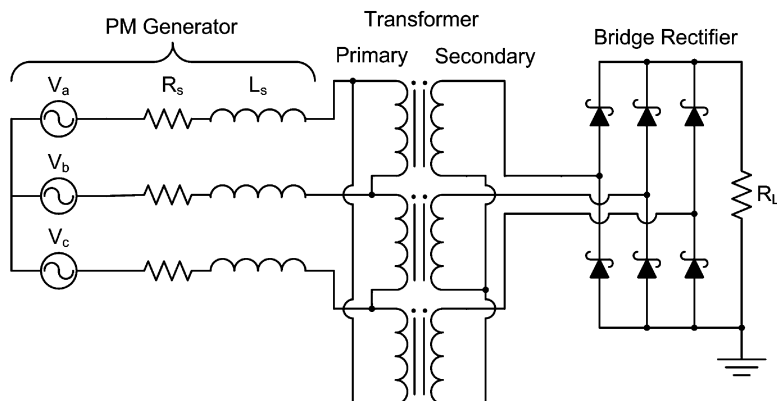
Fig. 8.26 Three-phase rectification circuit for DC power generation (Adapted from [64])

factor is only 82.6%. Clearly, as the speed rises, passive power electronics become a poor choice for power conversion.

Active power electronics can eliminate the transformer, diode bridge, and linear regulator, and provide all four functions (power factor correction, rectification, voltage step-up, and regulation) in a much more compact and efficient way. Active power electronics for a macroscale PMSM often requires speed and/or position sensing to determine the position of the magnetic poles on the rotor. This information is used to keep the stator currents in phase with the voltage to achieve maximum energy/power conversion. Hall effect sensors are sometimes used to directly measure the rotor position but are difficult to integrate into a microscale PMSM. "Sensorless" techniques to estimate the rotor position from current and terminal voltage measurements are also used in macroscale PMSMs but are computationally intensive, often requiring the use of high-performance microprocessors or digital signal processors. Real time processing of current and voltage information to determine the proper turn-on and turn-off times of the power transistors would be difficult achieve for the high speeds in the microscale PMSMs.

The active power electronics designed for microscale a PMSM uses a three-phase boost semi-bridge topology [72], shown in Fig. 8.27, operating in discontinuous conduction mode (DCM). Independent control of all three phases, as well as direct position, speed, current or voltage sensing is not needed to align the stator currents with the line-to-neutral voltages due to DCM nature of the circuit [72]. The three power MOSFETs are driven from the same control signal and are turned on/off at a constant switching frequency much higher than the stator electrical frequency. The converter turns the PMSM into a current source that can be controlled with a voltage control loop implemented using an off-the-shelf pulse-width-modulated (PWM) control IC. This topology provides near unity power factor and low-harmonic distortion without the need for large low-frequency passive magnetic components [73].
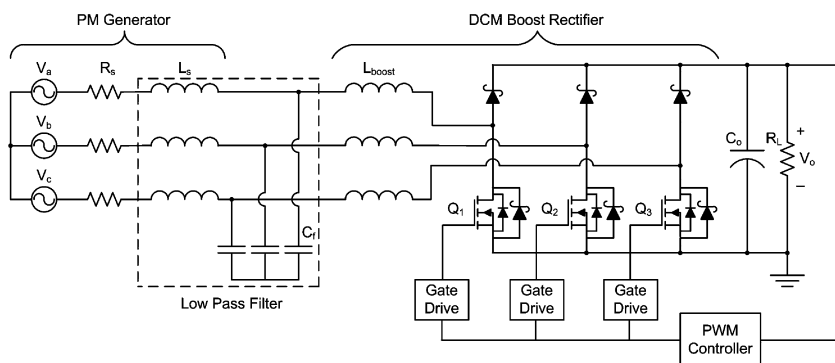
Fig. 8.27 DCM rectifier based on the boost semi-bridge topology (Adapted from [64])

The boost inductors are separate external inductors. The machine inductance and resistance, along with an external capacitor, act as a damped low-pass LC filter to attenuate the ripple current from the boost inductors so that the line voltage sees mainly a sinusoidal current at the line frequency. By using separate inductors, the high-frequency high-ripple currents are localized on the printed circuit board to minimize electromagnetic interference (EMI). In addition, the RMS stator currents are primarily due to the fundamental harmonic. This leads to low-harmonic distortion and reduced conduction loss in the stator windings. Even though the RMS currents are larger in the boost inductor, the resistance of the boost inductor is much smaller than the stator resistance (by design) so the conduction loss in the inductor is a small fraction of the overall conduction loss.

At the beginning of each switching period the three MOSFETs are turned on and the currents through the boost inductors rise to a value proportional to their respective open-circuit line-to-neutral voltages. The duty ratio determines the fraction of the switching period that the switches remain on. When the MOSFETs are turned off, the currents will flow through the diode bridge. If the currents through the boost inductor are positive, then current will flow through the high side (or boost) diode. If the currents are negative, they will flow through the free wheeling diode in parallel with the MOSFET.

The peak boost inductor current is proportional to the average value of the line-to-neutral voltage during the on-time of the MOSFET. This average value varies sinusoidally. Since the current in the boost inductor returns to zero each period, the variation in the average value of the current over a switching period will also be approximately sinusoidal, and will be in phase with the open-circuit voltage. For a DC output voltage much larger than the open-circuit voltage, such as is the case for microscale PMSMs, the time it takes for the boost inductor current to return to zero is much shorter than the on-time of the switch. Therefore, the average current over a switching period is almost independent of the output voltage leading to low-harmonic distortion of the current waveform [72].

Fig. 8.28 Simplified model of the boost rectifier and generator. The input circuit is shown on a per-phase line-to-neutral basis (Adapted from [64])
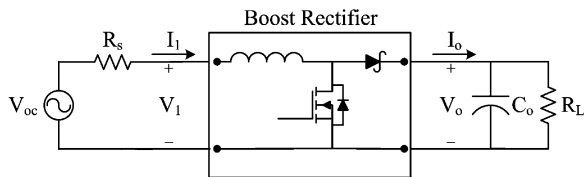

Figure 8.28 shows a simplified model of the power generation system. The input side is shown on a per-phase line-to-neutral basis. Assuming an ideal lossless converter, the input power will equal the output power such that

$$\frac{3}{2} V_1 I_1 = V_o I_o = P_o, \tag{8.99}$$

where V_1 is the peak line-to-neutral voltage after the stator resistance and I_1 is the peak fundamental component of the current through a single boost inductor. The input power from the generator will be

$$\frac{3}{2} V_{oc} I_1 = \frac{3}{2} I_1^2 R_s + P_o. \tag{8.100}$$

Solving (8.100) for I_1, the required current in each phase to deliver P_o to the output is

$$I_1 \frac{V_{oc}}{2R_s} \left(1 - \sqrt{1 - \frac{P_o}{P_{max}}} \right). \tag{8.101}$$

where

$$P_{max} \equiv \frac{3V_{oc}^2}{8R_s}, \tag{8.102}$$

And P_{max} is the power that the three-phase generator can deliver to a matched resistive three-phase load. The input voltage to the power converter on a line-to-neutral basis will be

$$V_1 = V_{oc} - I_1 R_s = \frac{V_{oc}}{2} \left(1 + \sqrt{1 - \frac{P_o}{P_{max}}} \right). \tag{8.103}$$

In [74], the input and output currents are derived for the three-phase DCM boost rectifier as functions of input voltage, output voltage, duty ratio, boost inductance, and switching frequency. The terms in [74] are modified using the voltage after the machine resistance, V_1, rather than the input voltage, V_{oc}. The average output current for the boost rectifier is

$$I_\mathrm{o} = \frac{1.46}{2L_\mathrm{boost}f_\mathrm{sw}} \frac{V_1^2 D^2}{(V_\mathrm{o} - 1.67V_1)} \tag{8.104}$$

where D and f_sw are the PWM duty ratio and switching frequency, respectively. The per-phase input current to the converter can be found using (8.99) and (8.104), and is given by

$$I_1 = \frac{0.973}{2L_\mathrm{boost}f_\mathrm{sw}} \frac{V_\mathrm{o} V_1 D^2}{(V_\mathrm{o} - 1.67V_1)}. \tag{8.105}$$

To deliver 10 W at an output voltage of 12 V, I_o must be 833 mA. Under the assumptions in that $V_\mathrm{oc} = 2.5$ V, and $R_\mathrm{s} = 100$ mΩ, P_max equals 23.44 W. Using (8.103), V_1 is 2.196 V. Equation (8.104) can be used as guide to determine the desired boost inductor value and duty ratio. Rewriting (8.104),

$$\frac{L_\mathrm{boost}}{D^2} = \frac{1.46}{2I_\mathrm{o}f_\mathrm{sw}} \frac{V_1^2}{(V_\mathrm{o} - 1.67V_1)}. \tag{8.106}$$

A PWM switching frequency of 500 kHz is chosen to minimize frequency dependent losses. Since the output voltage is much larger than the input voltage, a large duty cycle can be chosen and still keep the boost inductor current discontinuous. A larger duty ratio typically leads to a smaller RMS value for the boost current, minimizing conduction loss. However, since the converter is not lossless, any duty ratio set by (8.106) will under predict the actual duty ratio. This is because the converter must draw extra power to overcome its own losses which it does by increasing the inductor current. The duty ratio is set to 0.5 which corresponds to a boost inductor value of 0.36 μH. The closest standard value available is 0.33 μH and the resulting nominal duty ratio is 0.57. PSpice simulations of the boost rectifier confirm that the inductor current remains discontinuous at maximum output power.

The peak current in the boost inductor will be

$$I_\mathrm{pk} = \frac{V_1 D}{L_\mathrm{boost}f_\mathrm{sw}} = 7.6A. \tag{8.107}$$

The corresponding RMS current through the boost inductor is 3.8 A which is found from the simulation model. The D01813H-331 inductor from Coilcraft is a 0.33 μH surface-mount power inductor designed for high current applications. It is chosen as the boost inductor due to its high saturation (10 A) and RMS (7 A) current ratings, and its small size. The DC resistance of the inductor, R_DC, is only 4 mΩ. At a switching frequency of 500 kHz, the resistance of the inductor increases to 34 mΩ. The high-frequency resistance of the inductor windings is substantially larger than the DC resistance due to skin effect, and contributes a significant amount of loss in the inductor. This is expected due to the thickness of the wire used. In the future, the single thick wires can be replaced by multiple interposed thinner wires, or even Litz wire.

The PWM controller used for the boost rectifier is the UCC28C40 from Texas Instruments. It is intended for high-frequency power supplies for 12-V systems, and has a maximum switching frequency of 1 MHz. The operating supply current at 500 kHz is 4 mA. At a supply voltage of 12 V, the controller consumes 48 MW of power. The LM5112 gate driver IC from National Semiconductor is used to drive the power MOSFETS. The gate drive is capable of sourcing 3 A and sinking 7 A with a propagation delay of 25 ns. The selected power MOSFET (Q_1, Q_2, and Q_3 in Fig. 8.27) is the IRF7413Z from International Rectifier. It is a 30-V 13-A power MOSFET intended for notebook processor power applications. The diodes used in the bridge are 30-V 1-A DFLS130L surface-mount Schottky diodes from Diodes Inc. These diodes have very low forward voltages and junction capacitances.

The controller and gate drivers can be powered either from an external power supply or from the output voltage. To start up the converter, an external supply raises the input to 7 V, at which point the converter turns on and starts to bring up the output voltage. When the output voltage becomes larger than the external supply voltage, the converter powers itself up to 12 V. Two diodes provide an OR-ing of the two power sources.

The rectifier is shown in Fig. 8.29 along with a 3-turn-per-pole stator for size comparison. The rectifier power stage is 24 mm by 22.5 mm and has about the same surface area as the stator die. The PCB is 1.6 mm thick and most of the components are 1.75 mm in height or less with the boost inductors being 5 mm tall. The output filter capacitors and free wheeling diodes are placed on the bottom side of the power stage. The control section is 11 mm by 10 mm. The size of the control section could be made smaller by using EIA 0603 or 0402 sized packages for all the passives. This is not done here due to the challenge of soldering such small components.
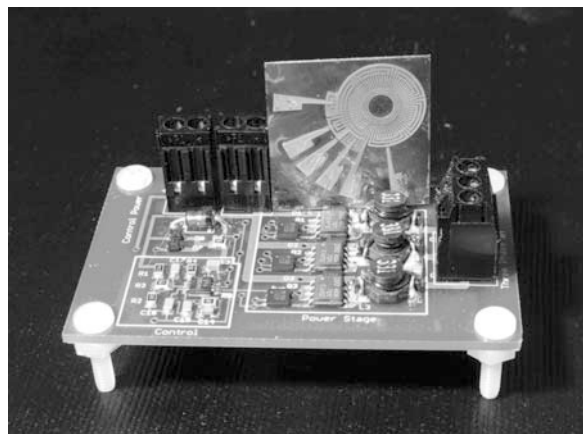

Fig. 8.29 Boost rectifier board shown with the 3-turn stator for size comparison (Adapted from [64])

Figure 8.30 shows the boost inductor current, stator current, and open-circuit voltage at a speed of 150 krpm. Both the boost inductor and stator currents are in phase with the open-circuit voltage. Figure 8.31 shows the boost inductor current,
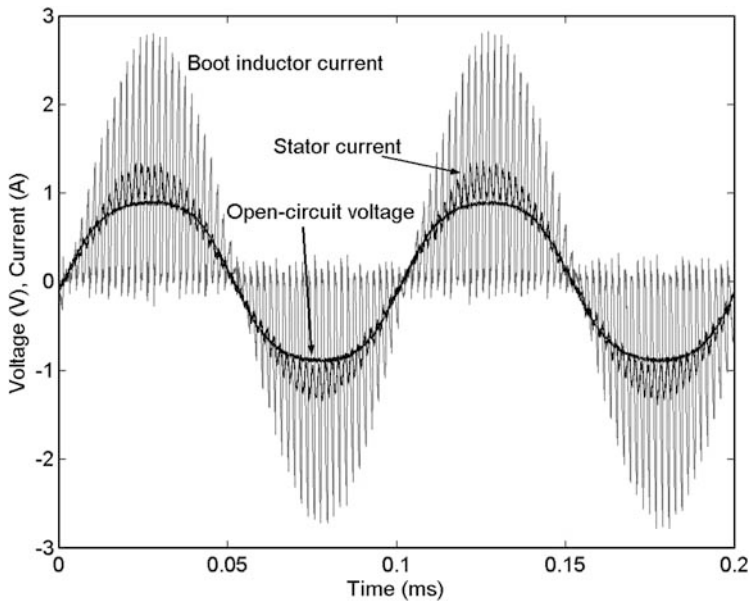
Fig. 8.30 Boost rectifier waveforms over two stator electrical periods at a generator speed of 150 krpm (Adapted from [64])
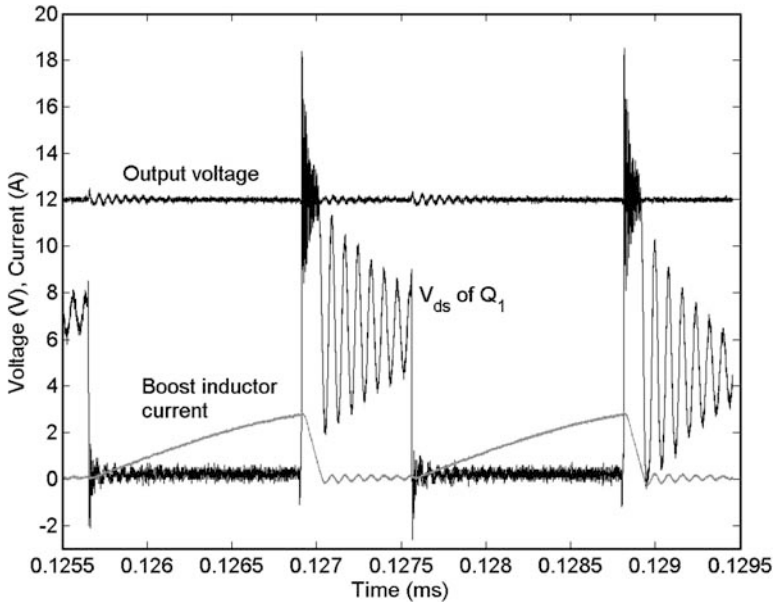

Fig. 8.31 Boost rectifier waveforms over two switching periods (Adapted from [64])

V_{ds} of Q_1 and the output voltage over a couple of switching periods. The ringing in the drain-to-source voltage and the inductor current is due to the LC tank created by the boost inductor and the output capacitance of Q_1. The output voltage also exhibits ringing when the MOSFET turns on and off. However, the magnitude is much smaller than the ringing on V_{ds} due to the output filter capacitor, C_o.

8.4.4 Experiments

ptA test stand has been developed to support spinning rotors in order to demonstrate electrical power generation while avoiding the design and fabrication complexities of integrated high-speed bearings [68]. The test stand consists of a high-speed, air-driven spindle to spin rotors with a controllable air gap over the surface of the stators, as depicted in Fig. 8.32. Powered by compressed nitrogen, the spindle provides rotational speeds in excess of 350 krpm. The rotor/shaft assembly is mounted in the spindle, and the rotation speed is measured with an optical shaft encoder or, in the case of electrical machine tests, using the frequency of the generated voltages. The stator is clamped to an xyz-micropositioner stage, having $\pm 5\,\mu$m resolution in all three directions. Rotors are mounted to a shaft and inserted into the spindle, which is attached to an articulating arm providing translation and rotation in all directions.
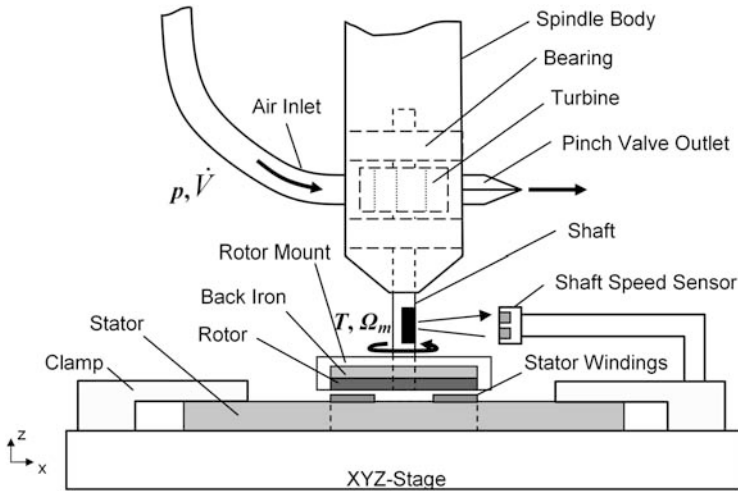

Fig. 8.32 Spinning rotor test stand, depicting the air-powered spindle spinning a magnetic rotor over the surface of the stator (Adapted from [64])

8.4.4.1 Electrical Characterization

The stators are first characterized in terms of their equivalent circuit parameters: phase resistance R_s, phase inductance L_s, and open-circuit voltage V_{oc} (Fig. 8.20).

The machines are then connected to power electronics for power generation tests, which are conducted at varying load resistances and speeds with the rotor–stator air gap set to 100 μm.

The stator has radial conductors with an average thickness of 188 μm. There is a layer of SU8 over the coils to protect them that is approximately 50 μm thick. The measured phase resistance is 145 mΩ which is 45% higher than predicted and is most likely due to variations in the thickness of the SU-8 layer between the top and bottom windings which can make the inner and outer end turns thinner than expected. The measured phase inductance is 0.34 μH, which is more than double the 0.138 μH predicted by the continuum model. This is because the continuum model does not take into account the leakage inductance from the inner or outer end turns. The leakage inductance of a macroscale machine is typically a small fraction of the magnetizing inductance [1]. In macroscale surface wound PM machines, the leakage can be on the same order of magnitude as the magnetizing inductance. In the microscale surface-wound PMSMs presented here, however, the leakage inductance dominates the overall stator inductance.

The permanent magnets used have an inner diameter of 5 mm and an outer diameter of 10 mm. The ideal square-wave magnetization with a B_r of 1 T for SmCo was seen to over-predict the experimental results in [65, 68, 69]. It is believed that the selective pulse magnetization process used to pattern the rotor magnetization does not fully saturate the material, resulting in a reduced remanence. Also, transition regions between poles are possible due to saturation of the magnetized heads at the edges of the magnetizer poles and the resulting leakage flux. A closer fit is obtained if the remanence used in the analytical model is reduced to 0.52 T. Further improvement, is made by introducing a 1.2 mm linear magnetization transition region, c_m, between north and south poles. This trapezoidal profile yields a more sinusoidal shape, and more likely represents the physical magnetization pattern.

The open-circuit voltage is shown as function of speed and air gap in Figs. 8.33 and 8.34 , respectively. The open-circuit voltage as function of speed is taken at an air gap of 100 and 250 μm while the voltage as a function of air gap is taken at 50, 100, and 150 krpm. The thickness of the SU8 layer is added to the air gap thickness. The RMS V_{oc} varies linearly with speed as expected and the open-circuit voltage is a decreasing function of air gap due to the exponential decay of rotor flux in the air gap. Notice that once B_r and c_m are set, the experimental measurements of V_{oc} agree very well with the values predicted by the analytical continuum model over a wide range of speeds and air gaps.

Power Generation Tests

Machine efficiency is an important consideration in the generator design. The power flow diagram for the generator is shown in Fig. 8.35. The total generator system efficiency, η_g, and electrical system efficiency, η_e, are defined as

$$\eta_g = \frac{P_{out}}{P_{mech}}, \tag{8.108}$$

Fig. 8.33 Open-circuit voltages versus rotational speed at different air gaps. *Points* represent measurements; *curves* represent the analytical model (Adapted from [64])
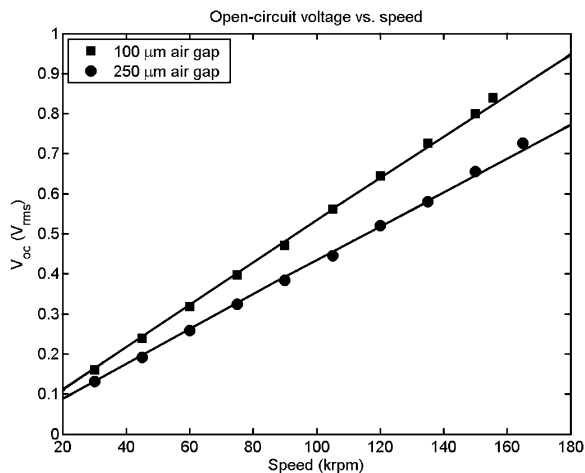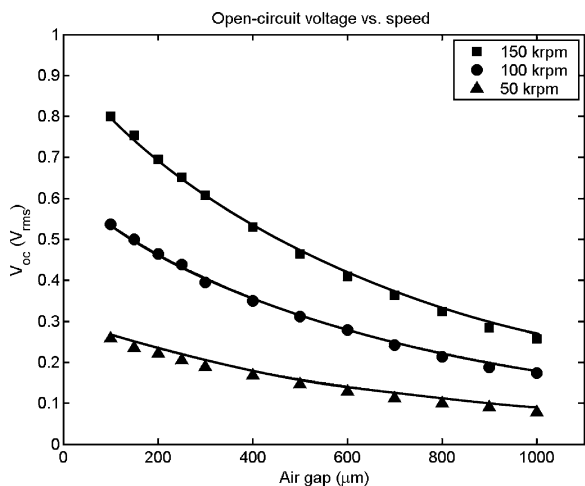

Fig. 8.34 Open-circuit voltages versus air gap at different speeds. *Points* represent measurements; *curves* represent the analytical model (Adapted from [64])

$$\eta_e = \frac{P_{out}}{P_{elect}}. \tag{8.109}$$

Direct experimental measurement of the total generator system efficiency is not possible because of the difficulty in measuring the mechanical input power, P_{mech}. Instead, the total input mechanical power is estimated by summing the proximity losses, core losses, and converted power; $P_{mech} = P_{prox} + P_{core} + P_{elect}$. The core losses P_{core}, and proximity losses P_{prox}, are computed from the analytical model. The core losses consists of both eddy-current and hysteresis losses. The converted
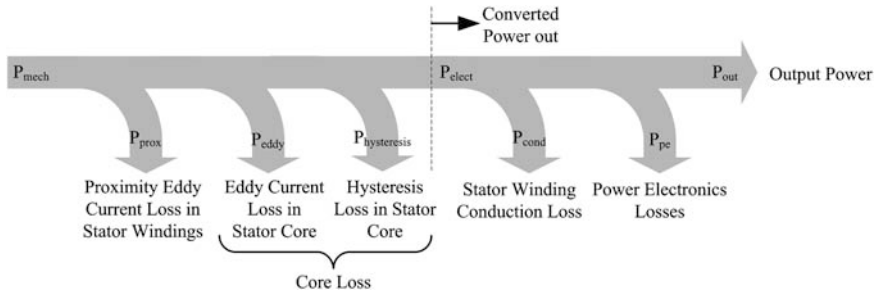
Fig. 8.35   Power flow diagram for generator system (Adapted from [64])

power P_{elect} is the power available from the open-circuit voltage in the equivalent circuit model, and is extracted from a PSpice model. P_{elect} consists of stator winding conduction loss P_{cond}, power electronics losses P_{pe}, and the power delivered to the load, P_{out}. The efficiency of the power electronics, η_{pe}, is

$$\eta_{\mathrm{pe}} = \frac{P_{\mathrm{out}}}{P_{\mathrm{out}} + P_{\mathrm{pe}}}. \tag{8.110}$$

The PMSM is tested using the transformer and diode bridge rectifier from [69]. Testing focuses on delivering maximum power to the load resistor as a function of speed. The output power versus speed is shown in Fig. 8.36. The load resistance is 37 Ω. At a rotor speed of 305 krpm, the PM generator delivers 8 W of DC power to the load resistor at an estimated electrical system efficiency of 49.2%. This corresponds to 16.27 W of mechanical-to-electrical power conversion. There is 7.46 W dissipated in the stator windings and 0.81 W dissipated in the transformer and diode bridge rectifier. The hysteresis losses in the stator core and the proximity eddy-current losses in the stator windings are 0.37 and 0.92 W, respectively. The stator core eddy-current losses are predicted to be 12.56 W. The resulting generator system efficiency, defined in Eq. (8.108) is only 26.6%. The measured values correspond well with a PSpice model of the generator and power electronics.

The dominant losses are the eddy current losses in the stator core which can be reduced significantly by using a laminated stator. The proximity eddy-current losses in the stator windings can be reduced by laminating the radial conductors. However, since the conduction losses are eight times as large as the proximity losses, it is better to leave the windings unlaminated to keep the winding resistance to a minimum.

Next, the PMSM is connected to the boost rectifier. To estimate the actual efficiency of the converter, the input current is measured using a Tektronix TCP202 current probe in conjunction with a Tektronix TDS3034B oscilloscope. The experimental input power is found by multiply the RMS values of the measured open-circuit voltage and stator currents by the power factor predicted by the PSpice model. This is done because the open-circuit voltage and stator currents could not be measured at the same time to compute the measured input power. The output

Fig. 8.36 DC output power across the load resistor for stator #3 vs. speed for a 37 Ω load at a 100 μm air gap. *Points* represent measurements; *curves* represent PSpice modeling (Adapted from [64])
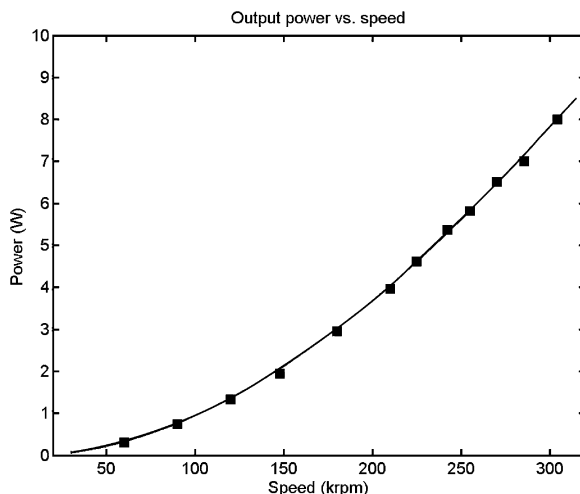
power is measured in real time with a voltage probe across a load potentiometer, a current probe around a wire connecting the potentiometer to the rectifier and using the channel math function on the oscilloscope.

Figure 8.37 shows the output power at different speeds for both a self-sustaining converter and a converter with a 12-V external control power supply. Note that this is not the maximum output power at these speeds, but rather what can be achieved using the coarse pressure control knob on the nitrogen tank [64]. Also plotted in Fig. 8.37 is the input stator current required to achieve the output powers at various speeds. The externally powered boost rectifier demonstrates 5.47 W of power delivery at of 298 krpm, while the self-sustaining boost rectifier delivers 5.52 W at 303 krpm. These two data points were achieved by fixing the load resistance and then increasing the nitrogen pressure to achieve a 12-V output voltage. The measurements were then recorded and the pressure was decreased to slow down the rotor. Attempts were not made to adjust the load potentiometer to find the maximum power due to concerns for rotor structural integrity at these speeds.

The power electronics, electrical system, and generator system efficiencies for the self-sustaining boost rectifier are shown in Fig. 8.38. The power electronics efficiency varies between 40% at low speed and power, to 70% at high speed and power. This is because, as the speed increases, the output power delivered increases making the fixed losses in the control IC and gate drives a smaller fraction of the input power. At 303 krpm the self sustaining rectifier delivered 5.52 W at 69% power-electronics efficiency with an electrical system efficiency of 57%. Including the predicted core and proximity losses in the stator core of 13.72 W, the overall generator system efficiency is 23.6%. The self-sustaining rectifier has a generator system efficiency of only 11% at 150 krpm. The power factor for the output powers in Fig. 8.36 is between 98 and 99.5%.

Fig. 8.37 Power and stator current versus speed for the boost rectifier with and without external control power. *Points* represent measurements; *curves* represent PSpice modeling (Adapted from [64])
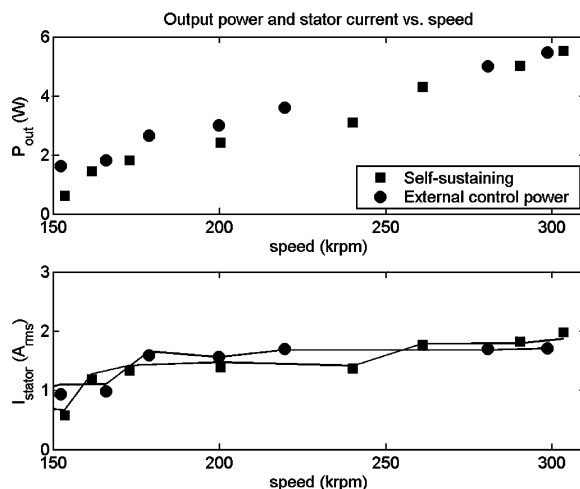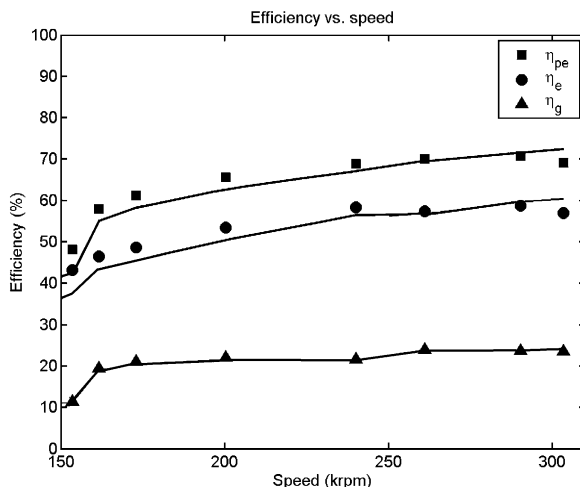

Fig. 8.38 Power electronics, η_{pe}, electrical system, η_e, and generator system, η_g, efficiencies versus speed for the self-sustaining boost rectifier. For η_{pe} and η_e, *points* represent measurements, and *curves* represent PSpice modeling. For η_g, *points* represent measurements/analytical model, and *curves* represent PSpice/analytical modeling (Adapted from [64])

To demonstrate the ability to power practical applications, the PMSM and rectifier is loaded with a series combination of six LEDs (two blue, two white, and two red). The generator is spun up to 150 krpm. A 9 V battery is connected temporarily to the control power terminal block and the converter boosts the output to 12 V. The test setup for this demonstration is shown in Fig. 8.39. Since the LEDS have a small viewing angle, the picture on the right shows the test setup from the top to better show the brightness of the LEDs. The control section of the rectifier consumes 0.48 W of power.

Figure 8.40 shows a self-contained microgenerator powering a PDA using only compressed gas [75]. The system integrates the PMSM, an air-turbine assembly
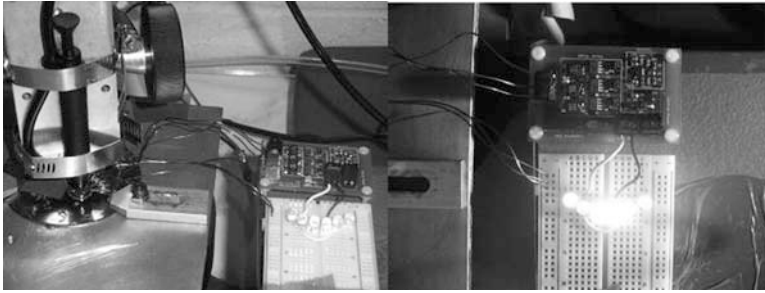
Fig. 8.39 Test setup for self-sustained operation. Boost rectifier is powering six LEDs (Adapted from [64])

Fig. 8.40 Standalone
generator powering a PDA

and power electronics into a compact, self-contained unit. The air-turbine assembly houses an off-the-shelf air-turbine in a conventionally milled stainless steel block. Two tubing connectors provide inlet and outlet connections to the air-turbine assembly. The rotor components are mounted on a steel shaft that fits into the air-turbine. Output wiring is soldered to the stator bond pads and routed to the power electronics board. The power electronics consist of three transformers for stepping up the generator voltages, a three-phase Schottky diode bridge for rectification and a linear regulator to provide a constant 5 V output under varying load conditions. The complete system measures 3.8 cm on a side, with a volume of 55 cm^3.

8.4.4.2 Comparison Between the Passive and Active Power Electronics

The passive and active power electronics are designed with different constraints and with different objectives. The goal of the passive power electronics is to maximize output power by efficiently stepping up and rectifying the generator's AC voltages with no constraints on the size of the circuit. In addition, output voltage regulation and power factor correction are not needed for initial low-speed power generation

tests. With no size constraint, a very large transformer is used to make the passive electronics highly efficient. The boost rectifier, on the other hand, is designed with size being an important consideration. Unlike the passive circuit, the boost rectifier provides power factor correction and voltage regulation in addition to stepping up and rectifying the AC voltages from the PMSM. Its goal is to efficiently deliver power at a regulated DC voltage with high power factor in a compact size. The size of the boost-rectifier power stage is limited to the size of a stator die. The passive and active power electronics are shown in Fig. 8.41. The transformer in the passive circuit is much larger than the power stage of the boost rectifier, and the bridge rectifier in the passive circuit is larger than the control section of the boost rectifier. The black terminal blocks in Fig. 8.41 are used so that the generator can be easily connected and disconnected to the power electronics.

Fig. 8.41 Size comparison of the passive (*left*) and active (*right*) power electronics
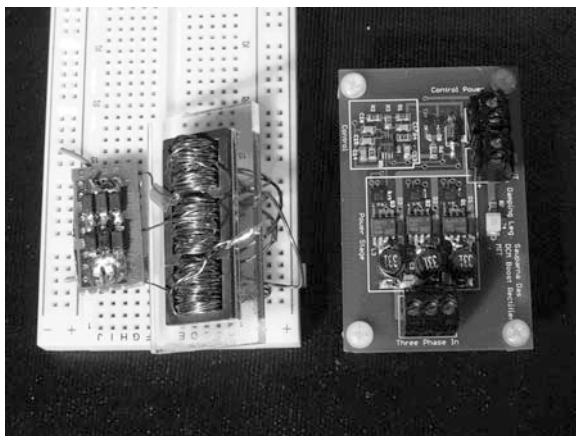
Table 8.6 gives a breakdown of the performance of the PMSM with the passive and active power electronics. At 305 krpm, the PMSM with the transformer and diode bridge rectifier can deliver 8 W at an electrical system efficiency of 49.2% and overall generator system efficiency of 26.6%. The passive power electronics is 90.8% efficient, but the generator has significant conduction loss (7.46 W) which is an order of magnitude larger than the losses in the power electronics. The power factor for the passive circuit is 89.2%. At 303 krpm, the PMSM with the boost rectifier can deliver 5.52 W at 57% electrical system efficiency and 23.6% generator system efficiency. The power factor of 98.3% is very close to unity. The boost rectifier is 69% efficient and the power lost in the circuit (2.46 W) is actually larger than the stator conduction loss (1.71 W). In both cases, the 12+ W of eddy-current loss in the stator core leads to generator system efficiencies that are significantly lower than the electrical system efficiencies.

A better performance comparison may be between the transformer/diode bridge rectifier and the power stage of the boost rectifier. At 303 krpm, the power stage

Table 8.6 Performance breakdown of the first and second generation power electronics

Property	Transformer/diode bridge rectifier	Self-sustaining boost rectifier power stage	Self-sustaining boost rectifier
Speed (krpm)	305	303	303
P_{mech}(W)	30.12	23.4	23.4
P_{prox}(W)	0.92	0.91	0.91
P_{eddy}(W)	12.56	12.45	12.45
$P_{hysteresis}$(W)	0.37	0.36	0.36
P_{elect}(W)	16.27	9.68	9.68
P_{cond}(W)	7.46	1.71	1.71
P_{pe}(W)	0.81	1.98	2.46
P_{out}(W)	8	6	5.52
η_{pe}(%)	90.8	78	69
η_e (%)	49.2	62	57
η_g(%)	26.6	25.6	23.6
Power factor (%)	89.2	98.3	98.3
Volume (mm^3)	5017	1080	1190
Power density (MW/m^3)	1.59	5.56	4.64

delivers 6 W out, of which 0.48 W is fed back to power the control circuitry. Since both circuits provide voltage step-up and rectification, one can think of the 0.48 W of fixed loss as the cost of providing output voltage regulation and power factor correction. The electrical system efficiency in this case is 62%, and the power stage is 78% efficient. The generator system efficiency in this case is only 1% less than the PMSM with the passive circuit. Another important metric for power electronic circuits is power density. The frame of the transformer is 43 mm long, 25 mm wide, and 3 mm thick. The windings are cylinders that extend 4 mm beyond the thickness of the frame in each direction and are 10 mm long each. The volume of the transformer is 4833 mm^3. The six diodes are 2.9 mm by 4.6 mm by 2.3 mm each, for a bridge rectifier volume of 184 mm^3. The total volume of the passive power electronics is 5017 mm^3 and the power density is 1.59 MW/m^3 when delivering 8 W to the load. The power stage of the boost rectifier is 24 mm by 22.5 mm. The tallest components are the boost inductors which are 5 mm high. The other components are 1–1.75 mm in height. The bypass and filter capacitors on the bottom side of the PCB can easily fit in the empty spaces on the top side of power stage area. For a mean height of about 2 mm, the volume of the power stage is 1080 mm^3. The control section is 11 mm by 10 mm, and the average component height is 1 mm for a volume of 110 mm^3. The total power electronics volume is 1190 mm^3. At an output power of 5.52 W the boost rectifier has a power density of 4.64 MW/m^3, which is nearly three times the power density of the passive power electronics. Considering only the power stage of the boost rectifier, the power density is 5.56 M W/m^3 for 5.52 W of output power (6 W from the power stage). This is more than three and a half times larger than the passive power electronics.

8.4.5 Conclusions

This section presented the modeling, design, and testing of microscale generators and power electronics capable of generating and delivering Watt-level DC power to a load. The generators are three-phase 8-pole axial-air-gap PMSMs. The rotor consists of a 500-μm SmCo permanent magnet, and a Hiperco 50 core. The stator consists of 3-turn-per-pole windings electroplated on the surface of a 1-mm thick Moly Permalloy stator core. The generators were designed and fabricated using a combination of microfabrication, and precision machining and assembly.

PMSMs allow the use of both passive and active power electronics to deliver DC power. The passive power electronics consist of a three-phase Δ/wye-connected transformer and a three-phase diode bridge rectifier. The active power electronics consist of a three-phase semi-bridge boost rectifier operating in DCM. DCM operation provides power factor correction without the need for direct rotor position/speed or stator current/voltage sensing. In addition, DCM operation of the rectifier turns the generator/boost semi-bridge into a controlled current source so that only a single feedback loop is necessary to regulate the output voltage. The power stage of the rectifier uses the same area as a stator die.

One generator is able to deliver 8 W of DC power to a load resistor at 305 krpm using the transformer and diode bridge rectifier. The stator current is 5.36 A peak corresponding to a current density of $\sim6\times10^8$ A/m^2, which is two orders of magnitude larger than what is possible in a macroscale machine. This is possible in an MEMS device because of the intimate thermal contact between the windings and their surrounding materials. For an active machine volume of 138.4 mm^3, (10-mm outer diameter, 5-mm inner diameter, and 2.35-mm thickness), the 8-W output power corresponds to a power density of 57.8 MW/m^3. A typical 1000-MW turbine/generator with an active volume of 60 m^3 (8.4-m length, 3-m stator-core outer diameter) has a power density of 17 MW/m^3. With 16.27 W electrical power converted through the air gap at 305 krpm, the shear stress is 2.8 kN/m^2 using (8.40). This is much lower than the 180 kN/m^2 for the 1000-MW liquid-cooled turbine/generator. Despite the lower shear stress the microscale generator has more than three times the power density of a 1000-MW turbine generator due its much higher current densities and rotor tip speeds.

The estimated electrical and generator system efficiencies are 49.2 and 26.6%, respectively, when the generator is delivering 8 W to a load. The main difference between the two efficiency metrics is due to the eddy-current losses in the stator core. In fact, the 12.56-W loss due to eddy currents in the stator core is larger than either the output power or the sum of all the other losses in the system (9.56 W). This means that laminating the stator will be necessary to increase the overall generator system efficiency. The proximity eddy-current losses in the stator windings are on the order of 1 W at 305,000 rpm. At higher speeds, this will increase significantly and it may be necessary to laminate the radial conductors of the stator windings as well. However, because the PMSM is expected to operate at 300°C in a microengine, the conductivity of the stator windings will drop by more than a factor of two.

The resulting decrease in conductivity will partially offset the increased proximity eddy-current losses due to higher rotational speeds. The increase in conduction loss due to higher temperatures may require that the radial conductors be unlaminated to minimize the sum of the conduction and proximity losses.

The microscale generator, when connected to the self-sustaining boost rectifier, is able to deliver 5.52 W to a load resistor at a regulated output voltage of 12 V and at a speed of 303 krpm. The power electronics is 69% efficient and has a power factor of 98.3%. The electrical and generator system efficiencies are 57 and 23.6%, respectively, with the difference due to the large eddy-current losses in the stator core. The power density of the boost rectifier is 4.64 MW/m^3, which is three times the power density of the transformer/diode bridge, even though it is less efficient than the passive circuit. The generators are also able to power a string of LEDs and a PDA. These results prove that Watt-level power generation and delivery is achievable using microscale axial-flux PM machines and switch-mode power electronics, and that they are a viable compact power generation system for portable power applications.

8.5 Summary

For reasons discussed in Section 8.1.1, this chapter has focused on the electric induction machine and the permanent-magnet synchronous machine. It is difficult to make a conclusive comparison between the two because their characteristics are very different at the microscale. The advantages of the electric induction machine are at that it is CMOS compatible, and probably the simpler of the two to fabricate. Further, it can operate at very high temperatures if its rotor conductor is designed with temperature stability in mind. Its greatest disadvantages are the viscous losses incurred in its air gap, and the inconvenience and complexity of developing high-voltage and high-frequency power electronics. Its operation as a generator is also greatly influenced by parasitics. The advantages of the permanent-magnet synchronous machine are its power and torque density, which have so far exceeded that of the electric induction machine, and its insensitivity to parasitics. Additionally, because of its comparatively lower pole count, the permanent-magnet synchronous machine can operate with a much larger air gap, and correspondingly smaller viscous losses. Its greatest disadvantage is probably the increased complexity of its fabrication, and its inability to run at high temperatures.

References

1. A. E. Fitzgerald, C. Kingsley, and S. D. Umans, *Electric Machinery*, Sixth Edition, McGraw Hill, New York 2003.
2. H. H. Woodson and J. R. Melcher, *Electromechanical Dynamics: Parts I & II*, Wiley, New York 1968.
3. W. Leonhard, *Control of Electrical Drives*, Springer-Verlag, Berlin 1985.
4. B. K. Bose, *Power Electronics and AC Drives*, Prentice-Hall, Englewood Cliffs 1987.

5. H. A. Haus and J. R. Melcher, *Electromagnetic Fields and Energy*, Prentice Hall, Englewood Cliffs 1989.

6. F. Paschen, "Ueber die zum funkenübergang in luft, wasserstof und kohlensäure bei verschiedenen drucken erforderliche potentialdifferenz"; *Annal der Physik*, *37*, 69–96, 1889.

7. J. M. Meek and J. D. Craggs, *Electrical Breakdown of Gases*, John Wiley & Sons, New York 1978.

8. M. Zahn, "Solid, liquid, and gaseous electrical insulation", *Encyclopedia of Applied Physics*, *18*, 431–466, VCH Publishers, Weinheim 1997.

9. S. F. Bart, T. A. Lober, R. T. Howe, J. H. Lang, and M. F. Schlecht, "Design considerations for micromachined electric actuators"; *Sensors and Actuators*, *14*, 269–292, July 1988.

10. M. Mehregany, P. Nagarkar, S. D. Senturia, and J. H. Lang, "Operation of microfabricated harmonic and ordinary side-drive motors"; *Proceedings: IEEE Workshop on Micro Electro Mechanical Systems*, 1–8, Napa Valley, CA, February 12–14, 1990.

11. M. Mehregany, S. F. Bart, L. S. Tavrow, J. H. Lang, S. D. Senturia, and M. F. Schlecht, "A study of three microfabricated variable-capacitance motors"; *Sensors and Actuators*, *A-21,22,23*, 173–179, February–April 1990.

12. S. F. Bart, M. Mehregany, L. S. Tavrow, J. H. Lang, and S. D. Senturia, "Electric micromotor dynamics"; *IEEE Transactions on Electron Devices*, *39*, 566–575, March 1992.

13. C. H. Ahn, Y. J. Kim, and M. G. Allen, "A planar variable-reluctance magnetic micromotor with fully integrated stator and wrapped coils", *Proceedings: IEEE Workshop on Micro Electro Mechanical Systems*, 1–6, Fort Lauderdale, FL, February 7–10, 1993.

14. H. Guckel, T. R. Christenson, K. J. Skorbis, T. S. Jung, J. Klein, K. V. Hartojo, and I. Widjaja, "A first functional current excited planar rotational magnetic micromotor", *Proceedings: IEEE Workshop on Micro Electro Mechanical Systems*, 7–11, Fort Lauderdale, FL, February 7–10, 1993.

15. W. C. Young and R. G. Budynas, *Roark's Formulas for Stress and Strain*, 7TH Edition, p. 745, McGraw-Hill, New York 2002.

16. M. W. Layland, "Generalized electrostatic machine theory", *IEE Proceedings*, *116*, 403–405, 1969.

17. T. J. E. Miller, *Switched Reluctance Motors and their Control*, Magna Physics Publishing and Oxford University Press, London 1993.

18. D. A. Torrey and J. H. Lang, "Optimal-efficiency excitation of variable-reluctance motor drives", *IEE Proceedings Part B*, *138*, 1–14, January 1991.

19. D. E. Cameron and J. H. Lang, "The control of high-speed variable-reluctance generators in electric power systems", *IEEE Transactions on Industry Applications*, *29*, 1106–1109, November/December 1993.

20. Y. Tada, "Theoretical characteristics of generalized electret generator using polymer film electrets", *IEEE Transactions on Electrical Insulation*, *21*, 457–464, June 1986.

21. Y. Arakawa, Y. Suzuki, and N. Kasagi, "Micro seismic power generator using electret polymer film", *Proceedings: PowerMEMS Conference*, 187–190, Kyoto, Japan, November 28–30, 2004.

22. Y. Sakane, Y. Suzuki, and N. Kasagi, "Development of high-performance purfluorinated polymer electret", *Proceedings: IEEE Symposium on Electrets*, *13*, Tokyo, Japan, September 15–17, 2008.

23. W. Olthuis and P. Bergveld, "On the charge storage and decay mechanism in silicon dioxide", *IEEE Transactions on Electrical Insulation*, *27*, 691–697 April 1992.

24. H. Köşer, *Development of Magnetic Induction Machines for Micro Turbo Machinery*, Ph. D. Thesis, EECS Department, MIT, June 2002.

25. F. Cros, *Developpement D'une Micromachine Induction Magnetique - Developpement do Techniques de Microfabrication pour Micro-electroaimants*, Ph. D. Thesis, Ecole Doctorale de Toulouse, France, September 2002.

26. H. Köşer and J. H. Lang, "Magnetic induction micro machine – Part I: design and analysis"; *IEEE/ASME Journal of Microelectromechanical Systems*, *15*, 415–426, April 2006.

27. F. Cros, H. Köşer, M. G. Allen, and J. H. Lang, "Magnetic induction micro machine – Part II: fabrication and testing"; *IEEE/ASME Journal of Microelectromechanical Systems*, *15*, 427–439, April 2006.

28. H. Köşer and J. H. Lang; "Magnetic induction micro machines – Part III: eddy currents and nonlinear effects"; *IEEE/ASME Journal of Microelectromechanical Systems*, *15*, 440–456, April 2006.

29. J. R. Melcher, *Continuum Electromechanical Dynamics*, MIT Press, Cambridge.

30. L. G. Frechette, *Development of a Microfabricated Silicon Motor-Driven Compression System*, Ph. D. Thesis, AA Department, MIT, September 2000.

31. S. F. Nagle, *Analysis, Design and Fabrication of an Electric Induction Micromotor for a Micro Gas-Turbine Generator*, Ph. D. Thesis, EECS Department, MIT, October 2000.

32. S. F. Bart and J. H. Lang; "Electroquasistatic induction micromotors"; *Proceedings: IEEE Workshop on Micro Electromechanical Systems Workshop*, 7–12, Salt Lake City, UT, February 20–22, January 1989.

33. S. F. Bart and J. H. Lang; "An analysis of electroquasistatic induction micromotors"; *Sensors and Actuators*, *20*, 97–106, November 1989.

34. L. G. Frechette, S. F. Nagle, R. Ghodssi, S. D. Umans, M. A. Schmidt, and J. H. Lang; "An electrostatic induction micromotor supported on gas-lubricated bearings"; *Proceedings: IEEE Workshop on Micro Electro Mechanical Systems*, 290–293, Interlaken, Switzerland, January 21–25, 2001.

35. C. Livermore, A. Forte, T. Lyszczarz, S. D. Umans, A. A. Ayon, and J. H. Lang; "A high-powerMEMS electric induction motor"; *IEEE/ASME Journal of Microelectromechanical Systems*, *13*, 465–471, June 2004.

36. S. F. Nagle, C. Livermore, L. G. Frechette, R. Ghodssi, and J. H. Lang, "An Electric Induction Micromotor", *IEEE/ASME Journal of Microelectromechanical Systems*, *14*, 1127–1143, October 2005.

37. J. L. Steyn, *A Microfabricated Electroquasistatic Induction Turbine Generator*, Ph. D. Thesis, AA Department, MIT, June 2005.

38. J. L. Steyn, S. H. Kendig, R. Khanna, T. M. Lyszczarz, S. D. Umans, J. U. Yoon, C. Livermore, and J. H. Lang; "Generating electric power with a MEMS electroquasistatic induction turbine generator"; *Proceedings: IEEE Workshop on Micro Electromechanical Systems*, 614–617, Miami, FL, January 30–February 3, 2005.

39. J. L. Steyn, S. H. Kendig, R. Khanna, T. M. Lyszczarz, S. D. Umans, J. U. Yoon, C. Livermore, and J. H. Lang, "A self-excited MEMS electroquasistatic induction turbine-generator"; *IEEE/ASME Journal of Microelectromechanical Systems, 18,* 424–432, April 09.

40. C. Kooy, "Torque on a resistive rotor in a quasi electrostatic rotating field"; *Applications of Scientific Research*, *20*, 161–172, February 1969.

41. B. Bollee, "Electrostatic motors"; *Phillips Technical Review*, *30*, 178–194, June–July 1969.

42. J. Ubbink, "Optimization of the rotor surface resistance of the asynchronous electrostatic motor"; *Applications of Scientific Research*, *22*, 442–448, October 1970.

43. S. D. Choi and D. A. Dunn, "A surface-charge induction motor"; *IEEE Proceedings*, *59*, 737–748, May 1971.

44. P. T. Krein and J. M. Crowley, "Harmonics affects in electrostatic induction motors"; *Electric Machines and Power Systems*, *10*, 479–497, May–June, 1985.

45. E. R. Mognashi and J. H. Calderwood, "Asynchronous dielectric induction motor"; *IEE Proceedings A*, *137*, 331–338, November 1990.

46. S. F. Bart, L. S. Tavrow, M. Mehregany, and J. H. Lang, "Microfabricated electrohydrodynamic pumps"; *Sensors and Actuators*, *A-21,22,23*, 193–197, February–April 1990.

47. S. Hardt and F. Schoenfeld, *Microfluidic Technologies for Miniaturized Analysis Systems*; Springer, New York 2007.

48. J. R. Melcher and M. S. Firebaugh, "Traveling wave bulk electroconvection induced across a temperature gradient"; *Physics of Fluids*, *10*, 1178–1185, 1967.

49. T. Kamins, *Polycrystalline Silicon For Integrated Circuits And Displays*, 2nd Edition; Kluwer Academic Publishers, Dordrecht, 1998.

50. T. C. Nuegebauer, D. J. Perreault, J. H. Lang, and C. Livermore, "A six-phase multilevel inverter for MEMS electrostatic induction micromotors"; *IEEE Transactions on Circuits and Systems II: Express Briefs*, *51*, 49–56, February 2004.

51. A. M. Flynn and S. R. Sanders, "Fundamental limits on energy transfer and circuit considerations for piezoelectric transformers"; *IEEE Transactions on Power Electronics*, *17*, 8–14, January 2002.

52. C. C. Lin, R. Ghodssi, A. A. Ayon, D. Z. Chen, S. A. Jacobson, K. S. Breuer, A. H. Epstein and M. A. Schmidt, "Fabrication and characterization of a micro turbine/bearing rig"; *Proceedings: IEEE Micro Electro Mechanical Systems Workshop*, 529–533 Orlando, FL, 1999.

53. L. G. Frechette, S. A. Jacobson, F. F. Ehrich, R. Ghodssi, R. Khanna, C. W. Wong, X. Zhang, K. S. Breuer, M. A. Schmidt, and A. H. Epstein, "Demonstration of a microfabricated high-speed turbine supported on gas bearings"; *Proceedings: Solid-State Sensor and Actuator Workshop*, 43–47, Hilton Head, SC, June 2000.

54. R. Ghodssi, L. G. Frechette, S. F. Nagle, X. Zhang, A. A. Ayon, S. D. Senturia, and M. A. Schmidt, "Thick buried oxide in silicon (TBOS): an integrated fabrication technology for multi-stack wafer bonded MEMS processes"; *Proceedings: Tenth International Conference on Solid State Sensors*, 1456–1459, Sendai, Japan, June 1999.

55. B. Yen, *A Fully-Integrated Mult-Watt Permanent-Magnet Turbine/Generator*, Ph. D. Thesis, EECS Department, MIT, June 2008.

56. F. Herrault, *Microfabricated Air-Turbine and Heat-Engine-Driven Permanent Magnet Generators*, Ph.D. Thesis, Institut National des Sciences Appliquées, Toulouse, France, February 2009.

57. B. Wagner, M. Kreutzer, and W. Benecke, "Permanent magnet micromotors on silicon substrates"; *Journal of Microelectromechanical System*, *2*, 1, pp. 23–29, March 1993.

58. K.-P. Kamper, et al., "Electromagnetic permanent magnet micromotor with integrated micro gear box"; *Proceedings of the 5th International Conference on New Actuators* (Actuator '96), June 1996, pp. 429–432.

59. U. Berg, et al., "Series production and testing of a micro motor"; *Proceedings of the 6th International Conference on New Actuators* (Actuator '98), June 1998, pp. 552–555.

60. P.-A. Gilles, J. Delamare, O. Cugat, and J.-L. Schanen, "Design of a permanent magnet planar synchronous micromotor"; *Proceedings of the 35th Mtg. IEEE Industry Appl. Soc.*, *1*, October 2000, 223–227.

61. C. Yang, et al., "An axial flux electromagnetic micromotor"; *Journal of. Micromechanics and Microengineering, 11*, 113–117, 2001.

62. A. S. Holmes, G. Hong, and K. R. Buffard, "Axial-flux permanent magnet machines for micropower generation"; *Journal of Microelectromechanical System*, *14*, 1, 54–62, February 2005.

63. H. Raisigel, et al., "Magnetic planar micro generator," in *Digest Tech. Papers Transducers '05 Conference*, Seoul, South Korea, June 10–14, 2005, 757–761.

64. S. Das, "Magnetic machines and power electronics for power MEMS applications," Ph.D. Thesis, Massachusetts Institute of Technology, Cambridge, MA, September 2005.

65. S. Das, D. P. Arnold, I. Zana, J. -W. Park, M. G. Allen, and J. H. Lang, "Microfabricated high-speed axial-air-gap multi-watt permanent-magnet generators – Part I: modeling"; *Journal of Microelectromechanical System*, *15*, 5, 1330–1350, October 2006.

66. M. Zahn, *Electromagnetic Field Theory: A Problem Solving Approach*, Kreiger, Malabar, 1979.

67. J. G. Kassakian, M. F. Schlecht, and G. C. Verghese, *Principles of Power Electronics*, Addison Wesley, Reading, 1991.

68. D. P. Arnold, S. Das, I. Zana, J. -W. Park, J. H. Lang, and M. G. Allen, "Microfabricated high-speed axial-air-gap multi-watt permanent-magnet generators – Part II: Design, Fabrication and Testing," *Journal of Microelectromechanical System*, *15*, 5, 1330–1350, October 2006.

69. D. P. Arnold et al., "Design optimization of an 8 W microscale, axial-flux, permanent-magnet generator"; *Journal of Micromechanics Microengineering, 16*, 290–296, 2006.
70. R. M. Bozorth, *Ferromagnetism*, IEEE Press, New York, Reissue, 1993.
71. "MMPA Standard No. 0100-00, Standard Specifications for Permanent Magnet Materials," published by International Magnetics Association (formerly Magnetic Materials Producers Association), Available: http://www.intl-magnetics.org/pdfs/0100-00.pdf.
72. E. H. Ismail and R. Erickson, "Single-Switch 3-Phase PWM Low Harmonic Rectifiers"; *IEEE Transaction on Power Electron*, *11*, 2, 338–346, March 1996.
73. A. R. Prasad, P. D. Ziogas, and S. Manias, "An active power factor correction technique for three-phase diode rectifiers"; *IEEE Transaction on Power Electron*, *6*, 83–92, January 1991.
74. D. Simonetti, J. L. Vieira, and G. Sousa, "Modeling of the high-power-factor discontinuous boost rectifiers"; *IEEE Transaction on Industrial Electronics*, *46*, 4, 788–795, August 1999.
75. D. P. Arnold, P. Galle, F. Herrault, S. Das, J. H. Lang, and M. G. Allen, "A self-contained, flow-powered microgenerator system"; Technical Digest 5th International Workshop Micro Nanotechnology For Power Generation and Energy Conversion Apps. (PowerMEMS 2005), Tokyo, Japan, 113–115, November 2005.